

POLITECNICO DI TORINO

Master's Degree in Mechanical Engineering

Master's Degree Thesis

Numerical Analysis of Zero Strain Point Behaviour in Adhesively Bonded Joints

Using Surface-Based and Element-Based Cohesive Zone Models



**Politecnico
di Torino**

Supervisor

Prof. Raffaele Ciardiello

Co-Supervisor

Dr. Mohammad Abbasi

Prof. Luca Goglio

Candidate

Dogus Doguturk

A.A. 2024/2025

ACKNOWLEDGMENTS

First and foremost, I would like to thank my advisor Prof. Raffaele Ciardiello, for his invaluable guidance, constant assistance in writing my thesis, and most importantly his direct and indirect support throughout the process. His expertise and encouragement have greatly contributed to the development of this research.

I would also like to thank my co-supervisors, Doctor Mohammad Abbasi and Prof. Luca Goglio, for their valuable contributions, constructive discussions, and technical advices, which greatly contributed to enhance this study.

Furthermore, I would like to express my special thanks to my mom and my family, for their continued support, patience and encouragement throughout my master's course. Their faith in me has always kept me going.

Finally, my deep gratitude to my friends, who have not only accompanied me in this academic journey but also shared the hardship and encouraged me to work through this challenging journey. Their presence has made this experience unbelievable.

ABSTRACT

Adhesively bonded joints, especially single-lap joints (SLJs), have gained many applications in aerospace and automotive industries due to their lightweight and efficient structures. The present study aims to highlight the proper detection of the Zero Strain Point (ZSP) through numerical modelling. Various models were developed and analysed in 2D and 3D FEM with cohesive elements and surface-based cohesive interactions. The epoxy adhesive proved better strain distribution in locating ZSP and replicating force-displacement behaviour; polyurethane was less versatile in some geometries. This paper points out ZSP prediction in FEM simulations through material property tuning and refinement of the mesh.

TABLE OF CONTENTS

ACKNOWLEDGMENTS	1
ABSTRACT	2
LIST OF FIGURES	6
1. INTRODUCTION	10
1.1. Motivation	10
1.2. Objective	11
2. LITERATURE REVIEW	13
3. METHODOLOGY	20
3.1. Finite Element Models	20
3.2. Surface-Based Cohesive Models.....	23
3.3. Cohesive Element-Based Models.....	25
3.4. Mesh Configuration.....	30
3.4.1. 2D Surface-Based Cohesive Model	30
3.4.2. 2D Element-Based Cohesive Model	31
3.4.3. 3D Surface-Based Cohesive Model	31
3.4.4. 3D Element-Based Cohesive Model	32
4. MATERIAL PROPERTIES	33
4.1. Adhesive Material Properties	33
4.2. Adherend Material Properties	38
5. BOUNDARY CONDITIONS	40
5.1. Boundary Conditions for 2D Models	40
5.1.1. Fixed End (Left Side).....	40
5.1.2. Loaded End (Right Side).....	40
5.1.3. Symmetries for 2D Models	41
5.2. Boundary Conditions for 3D Models	41
5.2.1. Fixed End (Left Side).....	41
5.2.2. Loaded End (Right Side).....	41
5.2.3. Off-Plane Boundary Conditions.....	42
6. THEORETICAL BACKGROUND	44
6.1. Bilinear Traction-Separation Laws and Their Role in Simulations	44
6.2. Damage Initiation: Quadratic Criteria.....	49
6.3. Damage Propagation: Power Law Criterion	53

7.	RESULTS.....	58
7.1.	Design of Experiments for Single-Lap Joint Specimens.....	58
7.2.	The Force-Displacement Analysis of Pu-L2W2T2.....	62
7.3.	The Zero Strain Point Analysis of Pu-L2W2T2.....	64
7.4.	Zero Strain Point Analysis for All Specimens.....	69
7.4.1.	The Results of 2D Surface-Based Approach.....	71
7.4.2.	The Results for 3D Surface-Based Cohesive Approach.....	102
7.4.3.	The Results for 2D Cohesive Element Approach.....	106
7.5.	Force-Displacement Analysis for All Specimens.....	112
7.5.1.	The Results of 2D Surface-Based Approach for Polyurethane Adhesive	112
7.5.2.	The Results of 3D Surface-Based Approach for Polyurethane Adhesive	114
7.5.3.	The Results of 2D Cohesive Element Approach for Polyurethane Adhesive	114
7.5.4.	The Results of 2D Surface-Based Cohesive Approach for Epoxy Adhesive.....	115
7.5.5.	The Results of 3D Surface-Based Cohesive Approach for Epoxy Adhesive.....	117
7.5.6.	The Results of 2D Cohesive Element Approach for Epoxy Adhesive.....	117
8.	DISCUSSION.....	121
9.	CONCLUSIONS.....	125
10.	REFERENCES.....	127

LIST OF TABLES

Table 4.1: Tuned Traction-Separation Properties of Polyurethane for the surface-based approach	36
Table 4.2: Tuned Traction-Separation Properties of Polyurethane for the element-based approach	37
Table 4.3: Tuned Traction-Separation Properties of Epoxy for the surface-based approach ...	37
Table 4.4: Tuned Traction-Separation Properties of Epoxy for the element-based approach ..	38
Table 4.5: Material Properties of Adherends ^[11]	39
Table 7.1: Single-Lap Joint Design of Experiments (Based on Abbasi et al., Backface strain as an index to detect damage initiation in composite single-lap bonded joints: Effects of adhesive type and joint dimensions, International Journal of Adhesion and Adhesives)	60
Table 7.2: Single-Lap Joint Design of Experiments (Based on Abbasi et al., A novel approach for damage assessment in adhesively bonded composite joints using backface strain technique, Composites Part B: Engineering)	60
Table 7.3: Energy Absorption and Error Comparison for L2W2T2 Specimen	64
Table 7.5: Relative Error for ZSP Position and Max. Strain for All Specimens	102

LIST OF FIGURES

Figure 1.1: Single Lap Joint (2D).....	12
Figure 1.2: Single Lap Joint (3D).....	12
Figure 3.1: Element types of the SLJ mesh setup showing both the adherend and adhesive regions in 2D surface-based approach.	23
Figure 3.2: Element types of the SLJ mesh setup showing both the adherend and adhesive regions in 3D surface-based approach.	24
Figure 3.3: Element types of the SLJ mesh setup showing both the adherend and adhesive regions in 2D.	25
Figure 3.4: Element types of the SLJ mesh setup showing both the adherend and adhesive regions in 3D.	26
Figure 3.5: Mesh and Stack Orientation for Cohesive Elements in a Single Lap Joint.....	29
Figure 3.6: Meshing in the 2D surface-based model	30
Figure 3.7: Meshing in the 2D element-based cohesive model	31
Figure 3.8: Meshing in the 3D surface-based cohesive model	32
Figure 3.9: Meshing in the 3D element-based cohesive model	32
Figure 4.1: Adhesives tensile tests: (a) Polyurethane (ADEKIT A 236/H 6236); (b) Epoxy (SIKAPower-1277). [11]	33
Figure 5.1: Boundary Condition for 2D Model.....	42
Figure 5.2: Boundary Condition for 3D Model.....	43
Figure 6.1: Mixed-mode failure envelope illustrating the interaction between Mode I and Mode II loading conditions [48].....	47
Figure 6.2: Bilinear traction-separation law depicting Mode I, Mode II, and mixed-mode fracture behaviours in cohesive zone models [48].	48
Figure 7.1: Geometric Configuration of the Single-Lap Joint Specimen (Based on Abbasi et al., A novel approach for damage assessment in adhesively bonded composite joints using backface strain technique [09] and Backface strain as index to damage initiation in composite single-lap bonded joints: Effects of adhesive type and joint dimensions [06]).....	59
Figure 7.2: Comparison of Force-Displacement curve of Pu-L2W2T2 specimen with different techniques.....	63
Figure 7.3. Position of the Zero Strain Point Measurement: (a) and (b) are for the 3D model, (c) for the 2D model.	65
Figure 7.4: Experimental Strain Distribution along the Overlap Length of L2W2T2 Specimen under Various Load Levels (Adapted from "A novel approach for damage assessment in adhesively bonded composite joints using backface strain technique") [09].....	66
Figure 7.5: Strain Distribution over the Overall Length along the Adhesive to detect ZSP for Pu-L2W2T2, Numerical result	67
Figure 7.6: Strain distribution of the Zero Strain Point (ZSP) at different load levels for L2W2T2, Numerical result	68
Figure 7.7: Evolution of Zero Strain Point (ZSP) Under Different Load Conditions for Pu-L2W2T2	69
Figure 7.8: Strain Distribution on the Backface of Pu-L1W1T1 through Overlap Length under Different Loads for (a) Experimental [09] and (b) Numerical Results	72
Figure 7.9: Strain-displacement and force-displacement curves for numerical result of Pu-L1W1T1	72

Figure 7.10: Strain Distribution on the Backface of Pu-L1W2T1 through Overlap Length under Different Loads for (a) Experimental [09] and (b) Numerical Results	73
Figure 7.11: Strain-displacement and force-displacement curves for the numerical result of Pu-L1W2T1.....	74
Figure 7.12: Strain Distribution on the Backface of Pu-L1W2T2 through Overlap Length under Different Loads for (a) Experimental [09] and (b) Numerical Results	75
Figure 7.13: Strain-displacement and force-displacement curves for the numerical result of Pu-L1W2T2.....	75
Figure 7.14: Strain Distribution on the Backface of Pu-L1W2T3 through Overlap Length under Different Loads for (a) Experimental [09] and (b) Numerical Results	76
Figure 7.15: Strain Distribution on the Backface of Pu-L1W3T1 through Overlap Length under Different Loads for (a) Experimental [09] and (b) Numerical Results	77
Figure 7.16: Strain-displacement and force-displacement curves for numerical result of Pu-L1W3T1	78
Figure 7.17: Strain Distribution on the Backface of Pu-L2W2T3 through Overlap Length under Different Loads for (a) Experimental [09] and (b) Numerical Results	79
Figure 7.18: Strain-displacement and force-displacement curves for numerical result of Pu-L2W2T3	79
Figure 7.19: Strain Distribution on the Backface of Pu-L2W1T1 through Overlap Length under Different Loads for (a) Experimental [09] and (b) Numerical Results	80
Figure 7.20: Strain-displacement and force-displacement curves for numerical result of Pu-L2W1T1	81
Figure 7.21: Strain Distribution on the Backface of Pu-L2W2T1 through Overlap Length under Different Loads for (a) Experimental [09] and (b) Numerical Results	82
Figure 7.22: Strain-displacement and force-displacement curves for numerical result of Pu-L2W2T1	83
Figure 7.23: Strain Distribution on the Backface of Pu-L2W3T1 through Overlap Length under Different Loads for (a) Experimental [09] and (b) Numerical Results	84
Figure 7.24: Strain-displacement and force-displacement curves for numerical result of Pu-L2W3T1	84
Figure 7.26: Strain-displacement and force-displacement curves for numerical result of Ep-L1W1T1	86
Figure 7.28: Strain-displacement and force-displacement curves for numerical result of Ep-L1W2T1	87
Figure 7.30: Strain-displacement and force-displacement curves for numerical result of Ep-L1W3T1	89
Figure 7.32: Strain-displacement and force-displacement curves for numerical result of Ep-L2W1T1	90
Figure 7.34: Strain-displacement and force-displacement curves for numerical result of Ep-L2W2T1	92
Figure 7.36: Strain-displacement and force-displacement curves for numerical result of Ep-L2W3T1	93
Figure 7.38: Strain-displacement and force-displacement curves for numerical result of Ep-L2W1T2	95
Figure 7.40: Strain-displacement and force-displacement curves for numerical result of Ep-L2W2T2	96

Figure 7.42: Strain-displacement and force-displacement curves for numerical result of Ep-L2W3T2	98
Figure 7.44: Strain Distribution on the Backface of Ep-L1W2T2 through Overlap Length under Different Loads for (a) Experimental [06] and (b) Numerical Results	100
Figure 7.45: Strain Distribution and Zero Strain Point (ZSP) Locations Across Overlap Length for Various PU Specimens Using 3D Surface-Based Cohesive Approach: (a) Pu-L1W1T1, (b) Pu-L2W3T1, (c) Pu-L1W2T1, (d) Pu-L1W2T2, (e) Pu-L1W3T1, (f) Pu-L2W2T2, (g) Pu-L2W1T1, (h) Pu-L1W2T3, (i) Pu-L2W2T1, (j) Pu-L2W2T3	104
Figure 7.46: Strain Distribution and Zero Strain Point (ZSP) Locations Across Overlap Length for Various EP Specimens Using 3D Surface-Based Cohesive Approach: (a) Ep-L1W1T1, (b) Ep-L1W1T2, (c) Ep-L1W2T1, (d) Ep-L1W2T2, (e) Ep-L1W3T1, (f) Ep-L1W3T2, (g) Ep-L2W1T1, (h) Ep-L2W1T2, (i) Ep-L2W2T1, (j) Ep-L2W2T2, (k) Ep-L2W3T1, (l) Ep-L2W3T2	106
Figure 7.47: Strain Distribution and Zero Strain Point (ZSP) Locations Across Overlap Length for Various PU Specimens Using 2D Cohesive Element Approach: (a) Pu-L1W1T1, (b) Pu-L2W3T1, (c) Pu-L1W2T1, (d) Pu-L1W2T2, (e) Pu-L1W3T1, (f) Pu-L2W2T2, (g) Pu-L2W1T1, (h) Pu-L1W2T3, (i) Pu-L2W2T1, (j) Pu-L2W2T3	108
Figure 7.48: Strain Distribution and Zero Strain Point (ZSP) Locations Across Overlap Length for Various EP Specimens Using 2D Cohesive Element Approach: (a) Ep-L1W1T1, (b) Ep-L1W1T2, (c) Ep-L1W2T1, (d) Ep-L1W2T2, (e) Ep-L1W3T1, (f) Ep-L1W3T2, (g) Ep-L2W1T1, (h) Ep-L2W1T2, (i) Ep-L2W2T1, (j) Ep-L2W2T2, (k) Ep-L2W3T1, (l) Ep-L2W3T2	110
Figure 7.49: Comparison of ZSP Position Across Specimens with Polyurethane Adhesive (1:Pu-L1W1T1, 2:Pu-L2W3T1, 3:Pu-L1W2T1, 4:Pu-L1W2T2, 5:Pu-L1W3T1, 6:Pu-L2W2T2, 7:Pu-L2W1T1, 8:Pu-L1W2T3, 9:Pu-L2W2T1, 10:Pu-L2W2T3).....	111
Figure 7.50: Comparison of ZSP Position Across Specimens with Epoxy Adhesive (1:Ep-L1W1T1, 2:Ep-L1W1T2, 3:Ep-L1W2T1, 4:Ep-L1W2T2, 5:Ep-L1W3T1, 6:Ep-L1W3T2, 7:Ep-L2W1T1, 8:Ep-L2W1T2, 9:Ep-L2W2T1, 10:Ep-L2W2T2, 11:Ep-L2W3T1, 12:Ep-L2W3T2)	112
Figure 7.51: Experimental Load-Displacement curve for Polyurethane adhesive specimens [9]	113
Figure 7.51: 2D Surface-Based Cohesive Method in Load-displacement curves of Polyurethane different specimens	113
Figure 7.52: 3D Surface-Based Cohesive Method in Load-displacement curves of Polyurethane different specimens	114
Figure 7.53: 2D Cohesive Element Method in Load-displacement curves of Polyurethane different specimens.....	115
Figure 7.54: Experimental Load-Displacement curve for Epoxy adhesive specimens [6]	116
Figure 7.55: 2D Surface-Based Cohesive Method in Load-displacement curves of Epoxy different specimens.....	116
Figure 7.56: 3D Surface-Based Cohesive Method in Load-displacement curves of Epoxy different specimens.....	117
Figure 7.57: 2D Cohesive Element Method in Load-displacement curves of Epoxy different specimens	118
Figure 7.58: Peak Load Comparison Across Specimens with Polyurethane Adhesive (1:Pu-L1W1T1, 2:Pu-L2W3T1, 3:Pu-L1W2T1, 4:Pu-L1W2T2, 5:Pu-L1W3T1, 6:Pu-L2W2T2, 7:Pu-L2W1T1, 8:Pu-L1W2T3, 9:Pu-L2W2T1, 10:Pu-L2W2T3)	119

Figure 7.59: Displacement at Peak Load for Different Approaches Across Specimens with Polyurethane Adhesive (1:Pu-L1W1T1, 2:Pu-L2W3T1, 3:Pu-L1W2T1, 4:Pu-L1W2T2, 5:Pu-L1W3T1, 6:Pu-L2W2T2, 7:Pu-L2W1T1, 8:Pu-L1W2T3, 9:Pu-L2W2T1, 10:Pu-L2W2T3)	119
Figure 7.60: Peak Load Comparison Across Specimens with Epoxy Adhesive (1:Ep-L1W1T1, 2:Ep-L1W1T2, 3:Ep-L1W2T1, 4:Ep-L1W2T2, 5:Ep-L1W3T1, 6:Ep-L1W3T2, 7:Ep-L2W1T1, 8:Ep-L2W1T2, 9:Ep-L2W2T1, 120 10:Ep-L2W2T2, 11:Ep-L2W3T1, 12:Ep-L2W3T2)	120
Figure 7.61: Displacement at Peak Load for Different Approaches Across Specimens with Epoxy Adhesive (1:Ep-L1W1T1, 2:Ep-L1W1T2, 3:Ep-L1W2T1, 4:Ep-L1W2T2, 5:Ep-L1W3T1, 6:Ep-L1W3T2, 7:Ep-L2W1T1, 8:Ep-L2W1T2, 9:Ep-L2W2T1, 120 10:Ep-L2W2T2, 11:Ep-L2W3T1, 12:Ep-L2W3T2)	120

1. INTRODUCTION

Adhesively bonded joints, particularly single-lap joints (SLJs), have found wide application in many industries where lightweight, structurally efficient design is required [1,18]. In aerospace engineering, weight reduction is always of prime importance without any compromise on mechanical integrity, and bonded joints are relied upon to reduce stress concentration at joint ends [1]. In the automotive industry, the important criterion is economy coupled with low weight, which, in turn, leads to better fuel consumption and performance [2]. Adhesive bonding shows great promise in this regard by providing uniform load distribution and hence design flexibility that would be advantageous for applications requiring durability and corrosion resistance as well as structural integration [18].

The joining of unlike materials, such as composites with metals, is another factor contributing to the wide field of application. The trend toward electric cars and new light aircraft improves the value of correct simulation of adhesive joints under real-life loading conditions [3, 34]. Without correct modelling, surprising failures of joints could lead to a drop in performance, higher maintenance costs, or even a disastrous failure. Early damage detection is key to achieving reliability, especially through precise strain measurement [4,35].

1.1. Motivation

While the damage mechanisms have been well explored in adhesive bonding [5], numeric modelling has yet to strike a good balance in reliably predicting the Zero Strain Point, particularly with ductile adhesives like polyurethane. [6] The Zero Strain Point is described as a critical point within overlap length where strain changes from compression to tension and where possible damage initiation starts [16]. If this transition could be captured, failure prediction would become much more accurate [16].

Polyurethane is more challenging than epoxy-based adhesives because, the strain distribution is rather complex due to its ductile nature and large deformation capacity [6, 8]. Mismatch relations between numerical predictions and experimental data are often in geometrically complex specimens or configurations under mixed-mode loading. Where such mismatches originate needs to be identified for improvement in predictiveness [8].

1.2. Objective

This study extends the experiments presented in [6] and [9], which include two main articles: “A novel technique for damage measurement in adhesively bonded composite joints using backface strain” and “Backface strain as a parameter to detect damage initiation in composite single-lap bonded joints: Effect of the adhesive type and the joint dimensions”. Novel experimental methods for damage initiation detection by one-sided or backface strain techniques were presented, providing a solid foundation for rigorous numerical validation in the form of cohesive zone models. By replicating both of these authors setups and comparing numerical results with their results, this thesis assesses the accuracy of cohesive surface and element-based methods to predict the mechanical behaviour of bonded joints.

The accuracy of determining the zero strain point location and the corresponding strain distribution under various conditions is the focus of this work using 2D and 3D finite element models developed in Abaqus [10]. (Fig. 1.1 and 1.2) Based on epoxy and polyurethane adhesive performance, despite the complexity of adhesive ductility affecting damage evolution and strain demand, the results are discussed for different configurations and loading scenarios as well as their implications on design. Each cohesive element model is compared to a surface-based cohesive interaction method to assess different modelling approaches, ultimately identifying advantages and disadvantages of both modelling strategies

based on their predicted strain distribution and damage evolution characteristics. Furthermore, various material properties tuning and mesh refinement approaches were implemented to achieve reasonably realistic numerical results that better matched experimental observations. Through this approach, the research improves the reliability of numerical simulations for adhesively bonded joints, supporting their application in high-performance structures where early damage detection and failure prevention are essential [6, 9]. This also helps ensure the reliability of numerical simulations of adhesively bonded joints, enabling their use in the design of advanced structures where early damage detection leads to the prevention of potential failures.

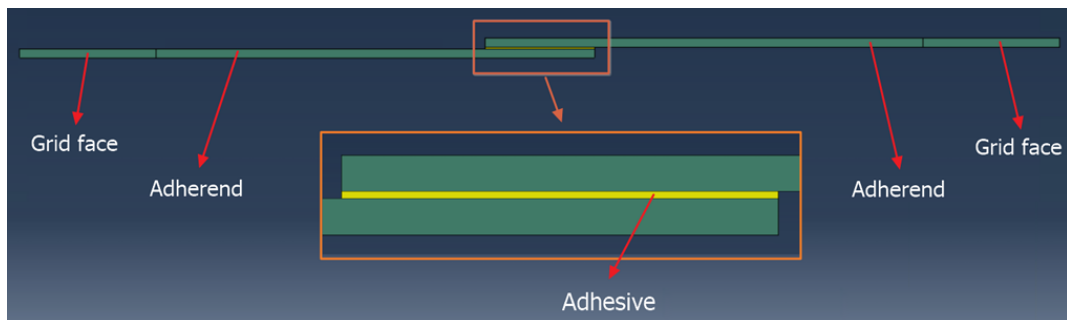


Figure 1.1: Single Lap Joint (2D)

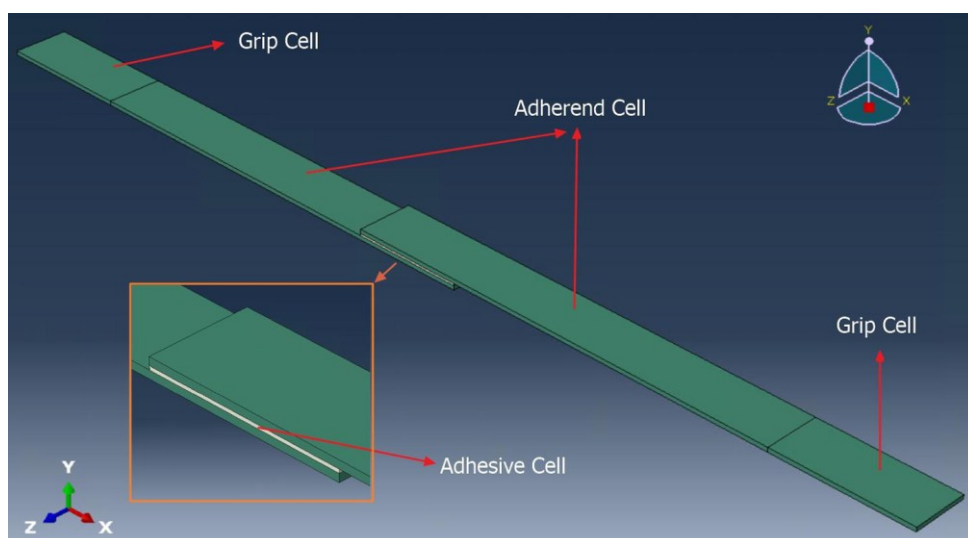


Figure 1.2: Single Lap Joint (3D)

2. LITERATURE REVIEW

One of the significant studies related to this thesis was conducted in [15]. Their research investigates various back-face strain (BFS) techniques, combining strain gauge (SG), digital image correlation (DIC) and finite element method (FEM) to obtain more insight into damage initiation and propagation of adhesively bonded joints. The study presents experimental data validating numerical models by correlating BFS data with crack initiation at the material's critical points (especially zero strain point (ZSP)) [15]. Adhesive composite material test of overlap joint using S700MC BL steel and EN AW-7075 T6 metal adherends.

BFS measurements were shown in to be capable to of properly detecting the onset of damage during the tensile loading process prior to macro crack growth [15]. Their experimental data on force-displacement curves matched well with FEM simulation for up to maximum peak force, which supports the potential of BFS as an effective early damage detection technique [15].

Finally, the strain distribution analysis showed that although there were slight fluctuations in strain distribution due to measurement errors, both the FEM and experimental results followed the same trend. Such results underscore the need for properly calibrated numerical models to closely approximate experimental conditions. Through analysing strain transitions for both simulations and experiments, the authors pointed out the zero strain point and established its significance as a damage initiation point, verifying the importance of this finding in terms of bonded joint analysis [15]. Their findings serve as a foundation for this thesis, which describes FEM simulations developed to reproduce and build upon their experimental results, most notably by relating surface vs. element-based cohesive model parameters to enable improved characterization of ZSP and damage evolution.

One more important contribution is the study in [16], titled “Damage Detection in Adhesively Bonded Single Lap Joints by Using Backface Strain: Proposing a New Position for Backface Strain Gauges”. The present work greatly improves the detection of damage by determining the optimal site for back face strain (BFS) gauges when placed on the adherent surface, which is determined by ZSP on the back side of the adherents. Using a combination of experimental testing and finite element analysis, the authors investigated the interplay between strain from applied loads and strain from bending moments in single lap joints bonded with Araldite 2015-1 epoxy adhesive, and either S700MC steel or EN AW-7075-T6 aluminium adherents. [16]

High accuracy must be ensured when strains are measured from the ZSP, which remains unchanged for undamaged joints but translocate to another position as damage propagates [16]. By embedding ZSP strain gauges across the ZSB, damage on the ZSB could be detected early enough by monitoring the variation of the strain distribution [16]. BFS measurements were experimentally validated using tensile testing and digital image correlation (DIC) to be sensitive to crack initiation and propagation [16]. These results were validated with finite element simulations that accurately predicted strain trends and also enabled the discerning of the cohesive failure modes involved, key determinants of joint integrity.

One of the most essential research conducted which falls under the scope of this thesis is presented in [9], titled “A Novel Approach for Damage Assessment in Adhesively Bonded Composite Joints Using Backface Strain Technique”. In this study, the proposed method for damage monitoring in the composite is conducted by integrating the benefits of BFS with DIC, and FOS for the non-destructive detection of damage in structural members in real-time during static and cyclic loading applications [9]. The adhesive type is ADEKIT A236/H6236

polyurethane whereas the reinforced substrate type is carbon fiber/epoxy prepreg (XPREG XC130) to study one of the major failure zones, namely the zero strain point [9].

Their results indicated that BFS measurements consistently crack position and crack growth. Under the undamaged condition, the ZSP was a stable indicator, but it changed in a predictable way with the propagation of cracks during static and cyclic loading. Geometrical factors, such as overlap length and joint thickness, etc. have also been studied. The findings showed that increased overlap lengths and thicker substrates produced more uniform stress distributions, which is favourable for better detection of ZSP [9].

This work is an important reference for the numerical fit in this thesis, where finite element simulations are used to reproduce the distribution of strain and force-displacement relations observed experimentally [9]. Overall, the work described in this thesis effectively addressed the ZSP shift and the cyclic damage evolution in numerical models, which forms the basis for developing more accurate predictive tools for adhesively bonded composite joints, which in turn can facilitate realistic and cost-effective designs in real-life scenarios [9].

The paper in [6], titled “Backface Strain as an Index to Detect Damage Initiation in Composite Single-Lap Bonded Joints: Effects of Adhesive Type and Joint Dimensions”, highlights further necessary consideration of the variables which determine damage initiation, and in particular the zero strain point behaviour in adhesively bonded joints and the influence of methodology and geometry on this behaviour. Carbon fiber/epoxy prepreg laminate (XPREG XC130) with polyurethane-based adhesive (ADEKIT A 236/H 6236) or epoxy-based adhesive (SIKAPOWER-1277) are used during this study. [6] The evaluation of the ZSP is an important part of structural health monitoring, and a sequence of peak experimental and numerical analyses is essential in finding out the extent to which adhesive properties,

overlap length, and substrate thickness influence the distribution of strain [6]. This is the character of their study.

The study showed that joint dimensions, especially overlap length and substrate thickness, were crucial to establishing the position of the ZSP [6]. More stable ZSP detection was achieved with longer overlap lengths and thicker substrates [6]. The experimental findings showed the ZSP undergoes a regular shifting as damage progresses, supporting its usage as a damage sensing mechanism [6]. Similar behaviour for transition in strain with the epoxy adhesive joints was more emphasized than with polyurethane adhesive joints, which also showed nonlinear observation due to higher ductility. This increased the difficulty of identifying ZSPs in polyurethane joints and emphasised the effectiveness of adhesive material in structural health monitoring [6].

Finally, they validated the numerical simulations with experimental data and the Bigwood and Crocombe analytical model predicting strain distribution in epoxy joints well before damage initiation. However, the model gave a less accurate prediction for polyurethane joints because they exhibit a nonlinear response [6, 17]. The agreement between experimental and simulated strain distributions suggests that the finite element method can be utilized in damage detection and design optimization as a design tool and accurately predicts the locations of the ZSP and crack initiation points [6, 17].

This study directly relates to the thesis, providing the experimental setup and validation metrics for the numerical replication efforts. This thesis seeks to characterise the ZSP behaviour across a range of adhesive and geometrical configurations, simulating these geometries through cohesive zone models with a focus on possible perspectives on predictive modelling of damage initiation and assessment of structural response in adhesively bonded joints [6].

The review in [18], titled “A Review of Finite Element Analysis of Adhesively Bonded Joints”, highlights how finite element methods (FEM) using tools like ABAQUS and LS-DYNA have been applied in adhesive joint analysis, making it highly relevant to this thesis [18]. The article provides an overview of their historical applications in predicting failure modes and detecting damage progression in bonded joints, offering foundational guidance for selecting the appropriate modelling techniques [18]. Specifically, the insights from this review support the validation of cohesive zone models by addressing the strengths and limitations of FEM software in simulating complex adhesive behaviour, a key focus of this thesis [18].

The study in [19], titled “Cohesive Zone Modeling of Adhesively Bonded Interfaces: The Effect of Adherend Geometry, Element Selection, and Loading Condition” is designed to inform this thesis directly through consideration for the accurate usage of cohesive zone models (CZMs) in ABAQUS. It illustrates the impact of element selection, connection method and bond line geometry on the stability and accuracy of the simulation results [19]. It is especially relevant to the choice of using either shell or solid elements to model the thickness of the adherends, which will affect the cohesive element behaviour under different modes of loading [19].

As described throughout this thesis, its main aim is to accurately predict the strain distribution and zero strain point (ZSP) behaviour of composite materials. The parametric study presented in [19] showed that using solid elements with type cohesive elements as the bond element produces sufficiently accurate force-displacement response over the simulation phase [19]. Moreover, the use of offset cohesive elements with shell element adherends while correctly accounting for rotational and translational degrees of freedom is recommended considering the accurate representation of ZSP behaviour under complex loading conditions and their comparison to experimental observations [19].

Additionally, the study in [19] addresses the restrictions of specific cohesive models to simulate Mode II and mixed-mode loading, which is highly applicable to the understanding of the adhesive failure in adhesive joints under combined tensile and shear loading in this thesis. This paper applied desired cohesive models and connection methods, and it is used for achieving close matches between numerical simulations and experimental observations for the thesis, thus enhancing the reliability of damage prediction and ZSP detection [19].

The study in [21], titled “Experimental and FE Investigations on the Influential Parameters in Positioning and Measurement of Strain Gauges in Adhesively Bonded Single Lap Joints”, is used for validation of the FEM model employed in the thesis. This article [21] discusses how tolerance on the thickness of bondline, and strain gauge misalignment affects strain distribution, failure loads, and damage detection, which is directly related to this research on zero strain point behaviour and damage initiation. Their experimental analysis [21] was performed on single lap joints (SLJ) with similar adhesive thickness, which corresponds exactly to my numerical settings in ABAQUS.

Moreover, their application of BFS measurements in conjunction with FE simulations to forecast damage initiation under tensile loading parallels the implementation of cohesive zone models (CZMs) that accurately correspond with strain transitions at the ZSP [21]. This paper improves its accuracy in predicting experimental strain trends and failure progressions for adhesively bonded joints by utilising its understanding of how geometric variations impact strain recordings [21].

Another study in [20], titled “Failure Load Prediction of Adhesively Bonded Single Lap Joints by Using Various FEM Techniques”, provides direct support for the methodology and validation processes used in this thesis. It explores several finite element methods (FEM) for failure-prediction, including cohesive elements and surface-based cohesive modelling, which are also utilized in this work. The article stresses the importance of choosing

meaningful initiation and propagation criteria, which relates to the tuning steps discussed in this thesis to accurately predict ZSP and force-displacement responses [20].

The study in [20] presents validation benchmarks that are relevant to this thesis since the comparative nature across bond-line thicknesses and the FEM techniques (cohesive elements, XFEM and VCCT) will point out the discrepancies and help calibrate the technique used in this thesis. Moreover, the analysis of failure loads at different bond line conditions serves as a counterpart to the sensitivity analyses performed within this thesis to establish confidence in cohesive zone models for failure behaviour [20]. These results highlight the importance of mesh convergence and the appropriate definition of the traction-separation laws, aspects which are directly reflected during the optimization procedure of the herein-developed numerical models [20].

3. METHODOLOGY

In this chapter the methodological framework employed in the analysis of adhesively bonded single-lap joints is introduced and explained in detail. Using finite element modelling, cohesive zone models were applied to represent damage initiation, propagation, and progression in the adhesive and adherend materials. Boundary conditions were meticulously designed to match experimental configurations and convergence tests were performed to verify the robustness of the numerical results. The investigation was done utilizing both 2D and 3D modelling approaches to evaluate ZSP detection and strain distribution accuracy.

3.1. Finite Element Models

The mechanical behaviour of adhesively bonded joints under loading conditions is greatly dependent upon finite element modelling. In this study, surface-based cohesive interactions and cohesive elements were utilized to develop 2D and 3D models in Abaqus [10]. The aim was to evaluate both approaches in terms of computational efficiency, ZSP detection accuracy, and to assess the damage mechanisms in the adhesive zone.

Abaqus is an integrated software suite for finite element analysis and computer-aided engineering and has been fundamental in the design, modelling, and assessment of adhesively bonded joints [10]. It can be used to analyse complex behaviours of joints under different loading scenarios, as its strong capabilities in modelling contacts, nonlinear materials and failure mechanisms are well-suited for this study [10]. This study chose to utilize Abaqus because it has advanced features for implementing cohesive zone models and traction-separation laws, thus enabling accurate predictions of damage initiation and propagation [10]. The cohesive elements and surface-based cohesive in Abaqus allowed for the comparison of strain distributions and ZSP positioning and indicated the advantages and disadvantages of

the method. Focusing on efficient prediction and tackling the discrepancy between experimental and numerical results, this study utilizes the software package Abaqus in a novel way by iterating material tuning, as well as conducting mesh sensitivity assessments.

One of the most valuable aspects of conducting these simulations in Abaqus was its capability to model both 2D and 3D bonded configurations, which helped to clarify the differences in strain distributions in ductile adhesives like polyurethane [10]. Moreover, its feature of allowing user-specified material laws (e.g., bilinear and trapezoidal traction-separation models) ensures that the adhesives' different characteristics are not lost [10]. Key factors are to enable correct through-thickness stress distributions, especially in thick adhesive layers. For instance, surface-based cohesive interfacial interaction is efficient for thin (e.g. adhesive) layers and large assemblies where the computational cost is a concern [20].

Cohesive zone models are implemented in Abaqus by using cohesive elements or surface-based cohesive interactions. The implementation of such algorithms is crucial for accurate predictions. The cohesive elements are capable of performing detailed three-dimensional stress analysis across the thickness of the components with lower-scale mesh elements, while surface-based interactions provide computational savings at the expense of modelling accuracy and can be applied for scaling up to larger simulations [10, 12].

The main difference between the two modelling approaches is that with the first one, the adhesive is considered a non-penetrable element. Surface-based cohesive models treat the adhesive as an interaction between the two adherends without explicitly modelling its thickness. Alternatively, cohesive element-based models treat the adhesive layer with explicit volume elements, which allows for a more detailed representation of through-thickness deformation [10, 12, 16].

Mesh generation in finite element analysis is one of the most critical aspects that take a significant part in deciding the accuracy, quality, efficiency and reliability of proof outputs from numerical simulations. The meshing methods are generally free meshing, structured meshing or sweep meshing, while each of these uses element types of quadrilateral, quad-dominated or triangular elements. This leads to various effects on stress-distribution and numerical correctness by the method and various types of elements [10].

The advantage of free meshing is that it can conform to complex geometries, but it can lead to lower accuracy since the element sizes will differ more and will have more numerical noise. Structured meshing can yield very high accuracy with evenly distributed elements but can be challenging to generate for complex geometries requiring simpler geometrical shapes. Although sweep meshing is very useful for extruded and revolution-based geometries, it is very useful for layered structures, but it is not ideal for non-extruded models [10].

In addition, quad elements need less elements for the same level of accuracy than other element shapes and have high accuracy in stress and strain computations and stress distributions. However, for complex shapes with high irregularities, they suffer from mesh distortion. Quad-dominated elements can provide a good compromise between flexibility and accuracy, meaning that they are more adaptable for complex geometries than tri-dominated, but less accurate. Triangular elements are very flexible for describing complex and curved geometries, having however less accuracy and they are computationally more expensive, requiring configuring higher number of elements to achieve same accuracy in contrast with quadrilateral elements [10].

Since single lap joints have notably simple geometry, especially the overlap region, thus structured meshing with quad elements would be the best at predicting stress and strain distribution, mainly around the bond line.

3.2. Surface-Based Cohesive Models

Such models can assist in modelling for relevant cases, particularly in cases with surface-based cohesive models where a focus on computing efficiency is desired. Instead of applying continuum mechanics to the adhesive, adhesive behaviour is implemented through traction-separation laws imposed on an interface at the surface of the adherends. The traction-separation law is used to describe surface interactions in tension, shearing, and mixed-mode loading conditions in both the 2D and 3D cases [10, 16].

In the 2D model, the geometry was simplified to reduce computational cost without compromising prediction accuracy along the overlap length, scheme with plane strain assumptions was used. Both the adherends and the adhesive were discretized by order of plane strain elements, CPE4R and the cohesive interaction applied between the surfaces. (Fig 3.1)

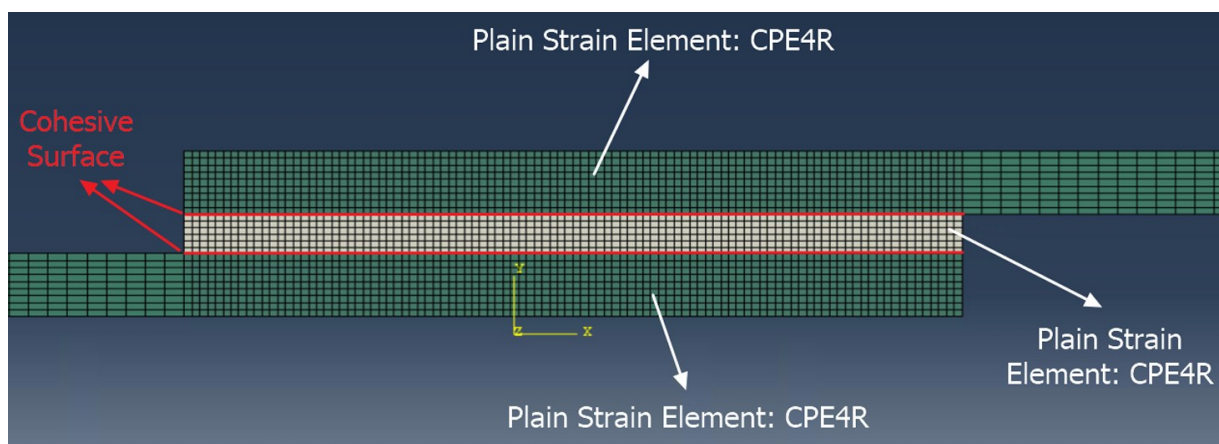


Figure 3.1: Element types of the SLJ mesh setup showing both the adherend and adhesive regions in 2D surface-based approach.

The 3D surface-based model expanded this concept by incorporating the joint's width as a third dimension. Such a model facilitated the capturing of strain gradients and stress concentrations along the width that the 2D model could not achieve. For both the adherends and the adhesive, a mesh using 3D continuum elements (C3D8R) was used and cohesive

properties were assigned based on surface-to-surface interaction. This approach works well in identifying the differences in ZSP over the joint width if the differences exist. (Fig 3.2)

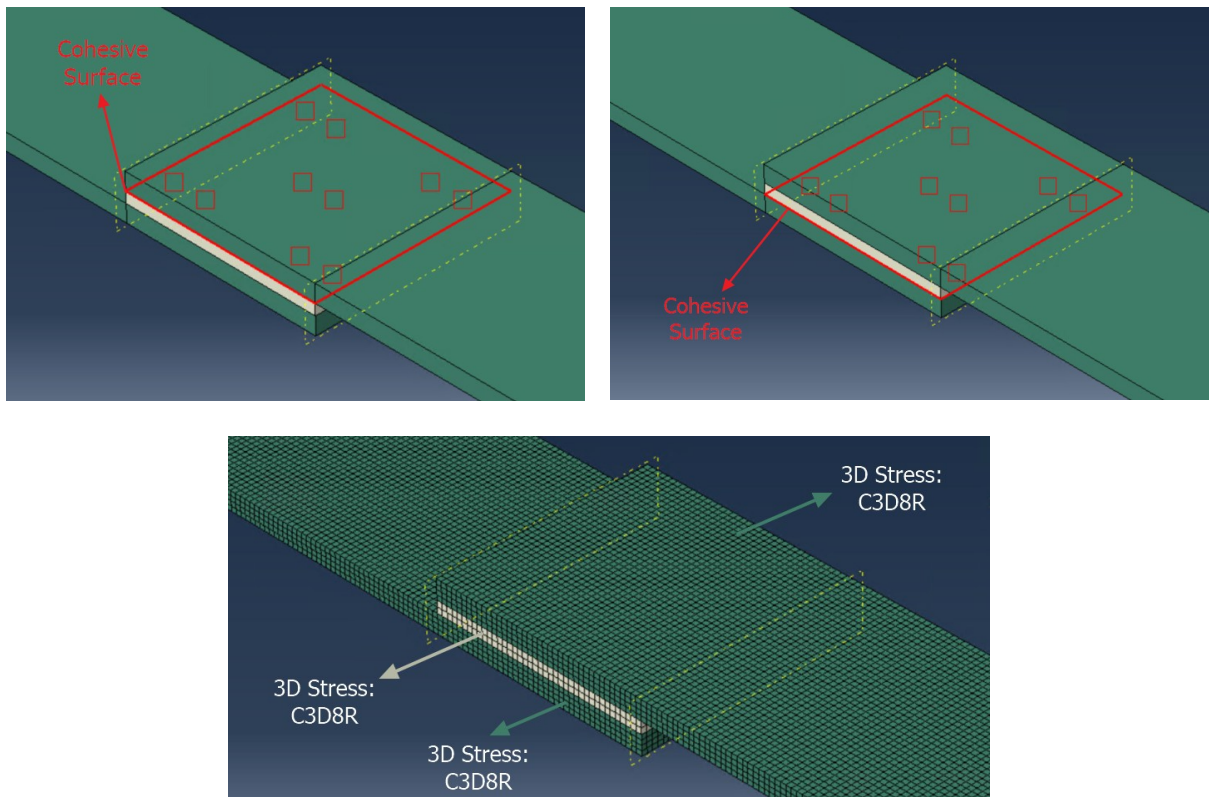


Figure 3.2: Element types of the SLJ mesh setup showing both the adherend and adhesive regions in 3D surface-based approach.

Cohesive models employed on the surface have a series of advantages, especially related to computer processing, since they have a lower number of degrees of freedom than element-based cohesive models. This efficiency in computational time renders them suitable for extensive parametric studies and initial analyses with urgent assessments of design variations. However, despite their advantages, surface-based models have drawbacks. A significant limitation of such approaches is their inability to model through-thickness deformation of the adhesive layer, which can be a pivotal factor in failure when the adhesive thickness is relatively large. This may cause building errors in accurately modelling joints with high adhesive thickness, which, in turn, may result in local stress concentration and damage progression errors [10, 12].

3.3. Cohesive Element-Based Models

The element-based approach also affords a more detailed representation of the adhesive layer. The adhesive is explicitly modelled with cohesive elements which facilitates in-plane and through-thickness damage progression. The adhesive layer was discretized in 2D using COH2D4 elements wherein the thickness was defined explicitly in the cohesive element model. For the adherends, CPE4R plane strain element type formulation is used. (Fig 3.3)

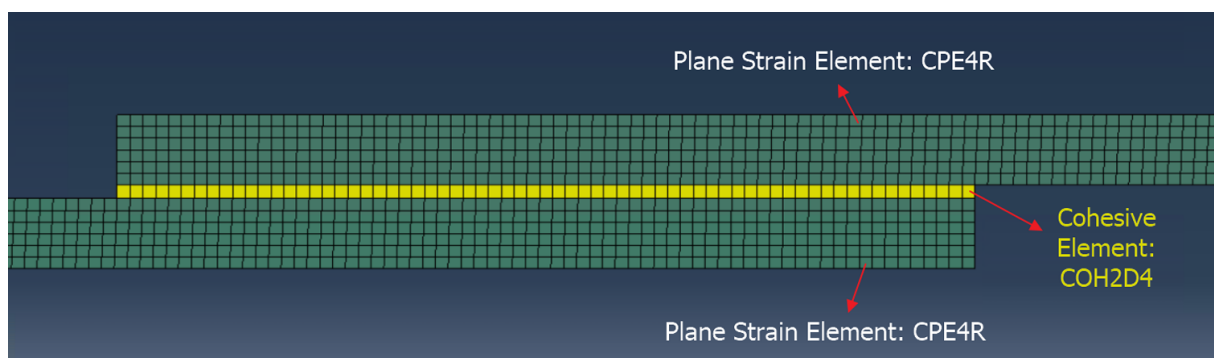


Figure 3.3: Element types of the SLJ mesh setup showing both the adherend and adhesive regions in 2D.

A 3D cohesive element model was developed to represent the adhesive in 3D using COH3D8 elements. The interaction between the adherends was better captured in the 3D model, especially for joints with approving adhesive thickness. For the adherends, C3D8R 3D stress element type formulation is used. (Fig 3.4)

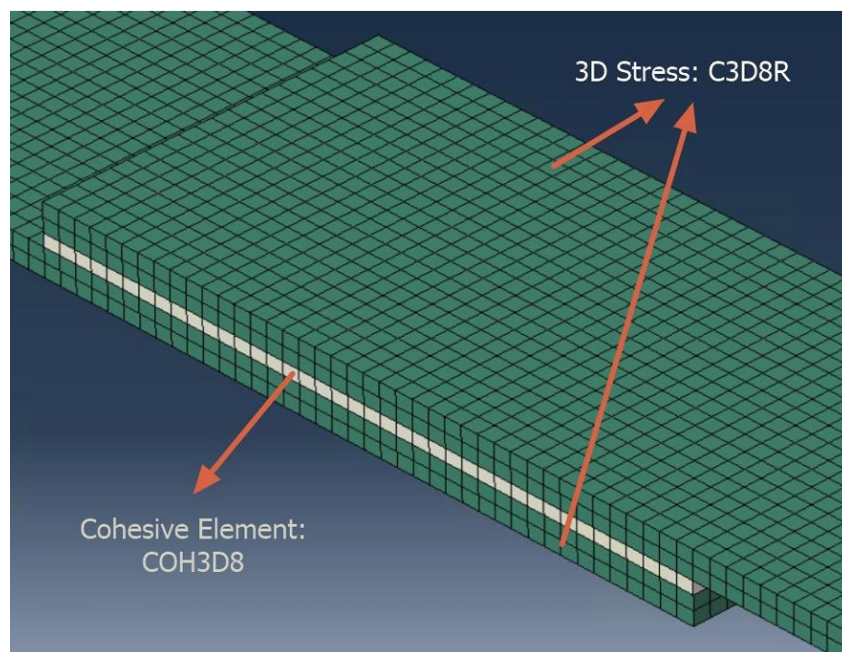


Figure 3.4: Element types of the SLJ mesh setup showing both the adherend and adhesive regions in 3D.

The element formulation mentioned before, CPE4R is a continuum plane strain 4-node reduced integration element and is commonly adopted in finite element modelling for certain structural applications. Continuous elements are denoted with the abbreviation "C," and they are used for the solid continuum representation so that they are appropriate for using material types such as adherents and "PE" represents plane strain (Strain in out-of-plane direction is negligible). This assumption can be relatively valid for cases with high aspect ratio such as single lap joints where thickness is mere fraction of other dimensions. The number "4" at CPE4R indicates that the element has four corner nodes (quadrilaterals are often four-cornered elements). The "R" in the name stands for reduced integration, which indicates that the element uses fewer integration points to reduce computation costs and to avoid numerical problems such as locking effect in the elements while keeping reasonably good accuracy. [10, 13, 14]

COH2D4 is cohesive 2D 4-node quadrilateral element which is designed to model adhesive layers. The "COH" is a magic element type or the element is intended for cohesive zone modelling, the COH element type is typically appropriate for modelling interfaces or bonds and so forth, and is particularly useful for modelling adhesive layers between two materials. This development enabled enforcement of crack initiation and propagation simulations that are of great importance in damage mechanics. The designation "2D" indicates that this element is a two-dimensional element and only computes displacements in the X and Y directions. This becomes especially effective to emulate where cohesive layers are utilized in, for example, single lap joints, because the most deformation and damage behaviours exist within a planar area. "4" indicates that having four corner nodes is a fundamental feature of finite element analysis for quadrilateral elements [10, 13, 14].

These properties make the COH2D4 element particularly effective for simulating the behaviour of adhesive bonds, in particular a model that is capable of adequately capturing debonding and crack propagation. This model is used often in simulations where damage initiation and propagation through the adhesive layer are important to represent accurately so the model is crucial to study failure mechanisms for bonded members.

C3D8R, known as the Continuum 3D 8-node Reduced Integration Element, is a hexahedral solid element for 3D stress analysis. "C" indicates that this is a solid continuum element and it represents bulk material and not interfaces or thin films. "3D" means that the element is 3-d space, so it computes deformations along the X, Y and Z axis. "8" indicates that the element has eight corner nodes that create a hexahedral (or brick) shape, allowing for better stress distribution in highly structured meshes. "R" states that the element employs lesser integration points for saving the computational cost and prevents volumetric locking for retaining accuracy [10, 13, 14].

COH3D8 is a three-dimensional cohesive element used to model interface behaviour in bonded materials to achieve cohesive zone modelling in 3D, “COH” indicates a cohesive zone model that simulates bonds between materials (like adhesives) or existing material interfaces, this element can simulate crack propagation and initiation. “3D” refers to the fact that the element behaves in a three-dimensional space (considering deformations in the X, Y, and Z directions). “8” indicates the eight corner nodes forming a hexahedral (brick) element, which is the mainly applied element type in 3D [10, 13, 14].

Correctly simulating crack propagation and adhesive failure behaviour depends on the stack orientation of the cohesive elements, or the alignment of their material axes to the global coordinate system. (Fig 3.5) Normal stiffness and strength are exerted along the Y-axis (Mode I), while shear stiffness and strength are oriented along the X-axis (Mode II) and Z-axis [25]. Cohesive elements are able to effectively simulate crack propagation and stress transfer under tensile and shear loading conditions correctly as long as they are properly oriented [10, 22].

For instance, if the normal stiffness is aligned to the X or Z-axis as opposed to the Y-axis the stack direction is misaligned, which may lead to errors in the predicted crack paths and predicted failure loads. It has been shown that misalignment of the cohesive zone with the load path is detrimental to the ability of the material to replicate simultaneous layer separation of the adhesive layer, resulting in erroneous predictions of damage onset and propagation in the system. Maintaining the proper orientation of the stack is hence crucial for providing realistic and accurate simulation outcomes, particularly for cases with mixed-loading wherein the materials are subjected to both tension and compression [10, 22].

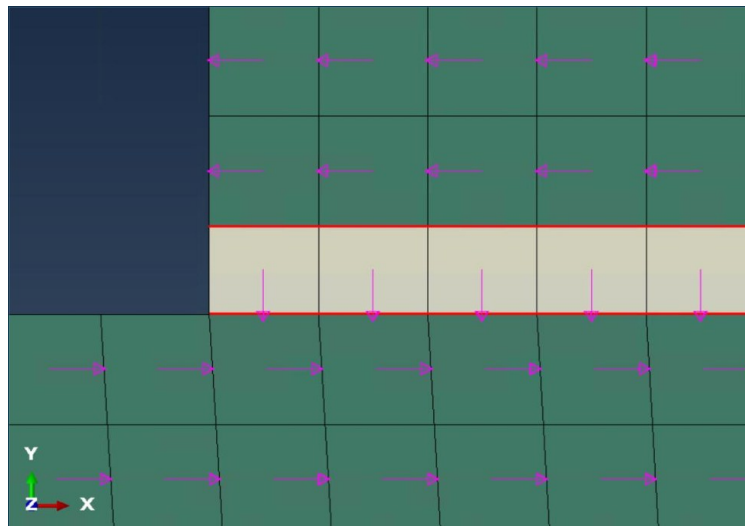


Figure 3.5: Mesh and Stack Orientation for Cohesive Elements in a Single Lap Joint

A cohesive element-based model will not only represent the through-thickness adhesive behaviour much better than the current implementation, but it is also able to capture the local stress distributions and variations of strain in the adhesive layer in conjunction with both the adhesive and bonded materials [23]. They are suitable for simulating the failure of complex mechanisms like delamination [33, 37] and debonding, which requires a detailed description of progressive damage [24]. These models, however, have limitations. A significant downside to them is that they are very cost-sensitive: more elements will require greater memory and longer simulation times. At the same time, cohesive element-based models tend to necessitate an increasingly fine mesh refinement to obtain convergence and reliable results, increasing both the computational demand and complexity of the model setup [26, 27].

Comparative analysis between both methodologies showed that while surface-based models were useful for quick screening purposes, cohesive element-based models allowed to obtain deeper insights into the evolution of adhesive damage in the previous literature review

[20]. Cohesive element models were essential to fully account for the damage behaviour for certain geometries, e.g. for thicker adhesive layers [16].

3.4. Mesh Configuration

The effectiveness of finite element simulations, specifically for adhesive joint simulation, is heavily reliant on the quality of the mesh further focusing on critical areas such as the adhesive layer and the adherend interface [10, 18]. A range of mesh configurations were employed for each model to find a compromise between computational efficiency and numerical accuracy [18, 20, 26]. Mesh sizes were chosen from convergence studies to achieve accurate strain distribution, ZSP detection and load-displacement predictions [16].

3.4.1. 2D Surface-Based Cohesive Model

The 2D surface-based cohesive model uniformly used a mesh size of 0.2 mm for any region. (Fig. 3.6) This fine mesh was required to catch the strain distribution along the overlap length and the ZSP transition [16, 18]. This definition of the surface interaction needed to be accurate enough to describe the behaviour of the interface without introducing numerical instabilities [16, 18].

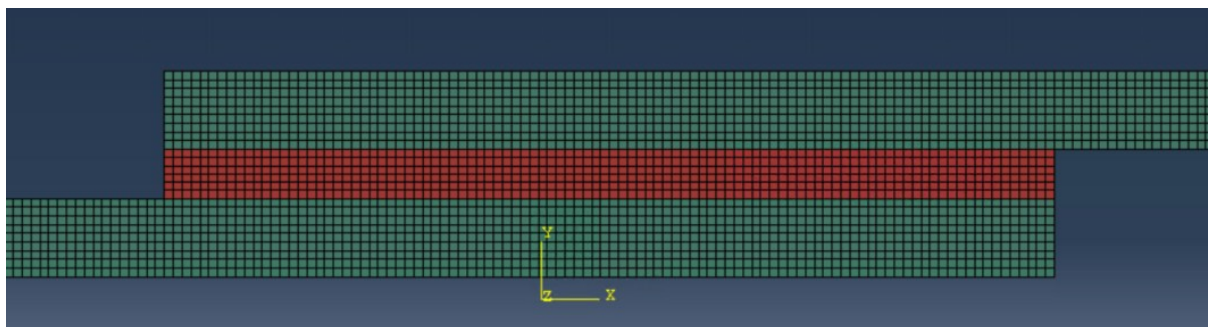


Figure 3.6: Meshing in the 2D surface-based model

3.4.2. 2D Element-Based Cohesive Model

A constant mesh size of 0.4 mm was used for the entire 2D cohesive element model. (Fig. 3.7) The cohesive part was embedded within the adhesive layer having a sufficient mesh refining that permitted to see the variation of the through-thickness strain. The mesh size was selected to ensure computational efficiency while also allowing the cohesive zone to capture crack initiation and propagation adequately. Because if cohesive elements are not in the single row order, it is observed that the convergence issues occur often [10, 20]. That is the reason why, the thickness of the adhesive layer is decreased to 0.4 mm in the 2D cohesive element models in order to avoid convergence problems. Because it is also observed that the decrease in the adhesive thickness does not dramatically affect the results. Therefore, this is a good compromising to refine mesh for cohesive element model.

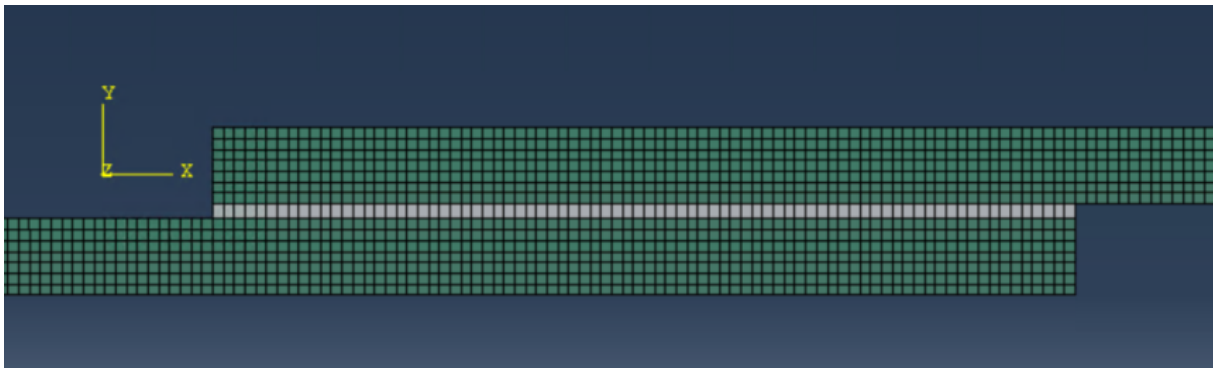


Figure 3.7: Meshing in the 2D element-based cohesive model

3.4.3. 3D Surface-Based Cohesive Model

In the case of the 3D surface-based cohesive model, the mesh size was 0.5 mm uniformly all over the model. (Fig. 3.8) Despite the complex nature of 3D modelling, using a mesh size of 0.5 mm provided a cost-effective compromise between simulation complexity and the resolution needed to resolve the interface adhesive behaviour. In particular, mesh

density was critical in capturing experimental strain trends in the case of surface-based cohesive interaction in 3D [10, 20].

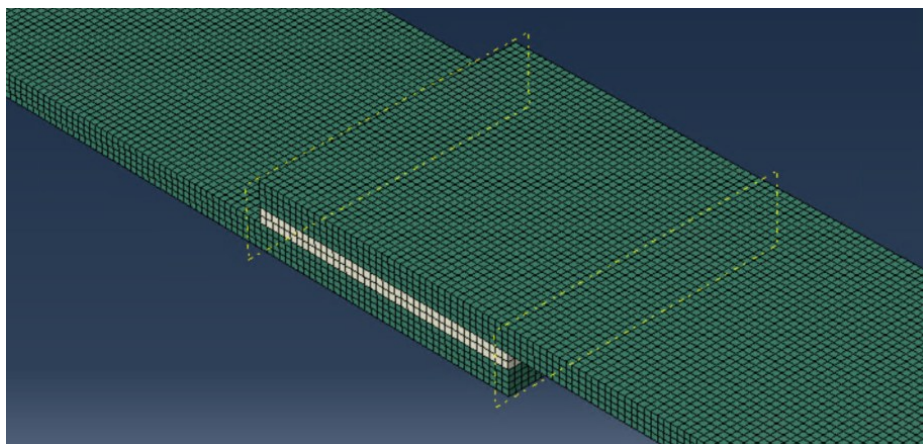


Figure 3.8: Meshing in the 3D surface-based cohesive model

The mesh configuration was validated in all cases by performing convergence tests to confirm that further refinement of the mesh did not produce significant changes in the numerical results.

3.4.4. 3D Element-Based Cohesive Model

In the case of the 3D element-based cohesive model, the mesh size was 0.5 mm uniformly all over the model. (Fig. 3.9) As in the 2D cohesive element model, in this model, the adhesive layer thickness was reduced to 0.5 mm to prevent convergence issues and a single row of cohesive elements was obtained.

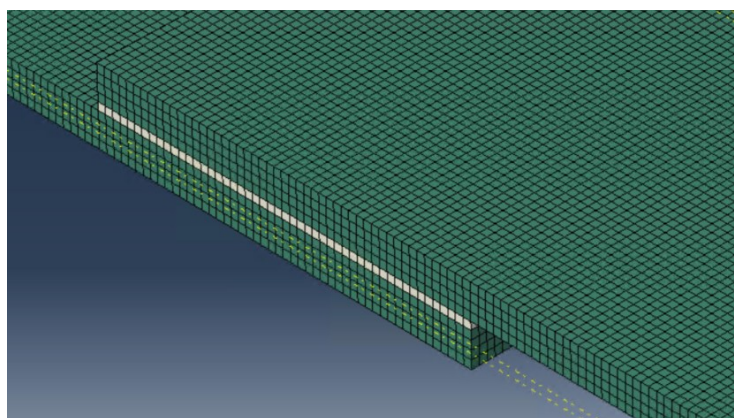


Figure 3.9: Meshing in the 3D element-based cohesive model

4. MATERIAL PROPERTIES

The mechanical behaviour of adhesively bonded single-lap joints is highly dependent on the material properties of the adhesive and adherends. Accurate modelling of these properties in finite element models is a crucial step for the accurate simulation of the mechanisms of load transfer, deformation and failure [18, 30]. Material parameters for adhesives and adherends used in the study were outlined based on experimental data, literature, and tuning. Table 4.1 lists the important mechanical properties that are taken into consideration for both polyurethane and epoxy adhesives as well as CFRP adherends.

4.1. Adhesive Material Properties

The adhesives referred to in this study are of both types such as polyurethane and epoxy to analyse their mechanical performance behaviours. Polyurethane is ductile and can absorb energy but epoxy is hard and suffers from brittle fracture. (Fig 4.1) These varying properties allowed for a closer analysis of how the different properties of the adhesive would affect the strain distribution and the ZSP.

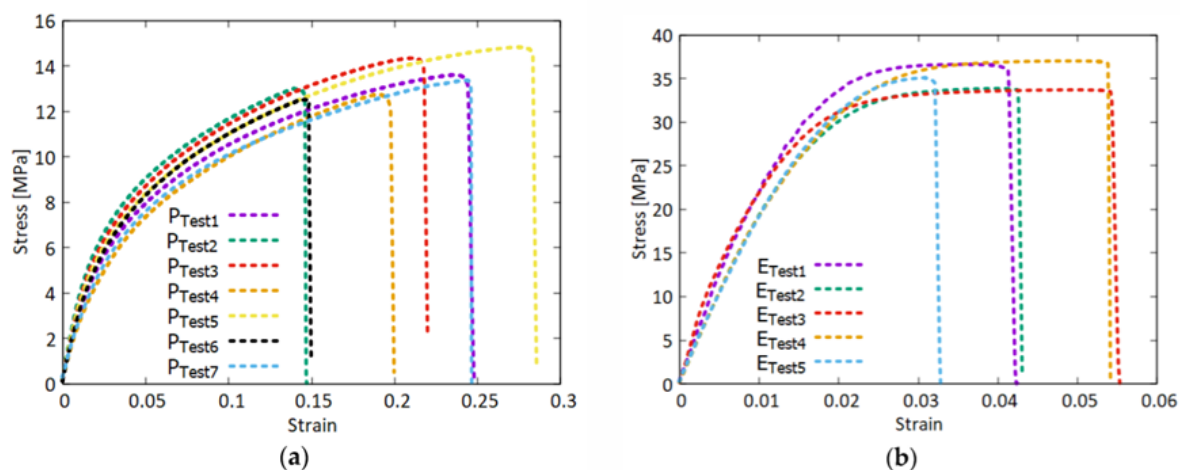


Figure 4.1: Adhesives tensile tests: (a) Polyurethane (ADEKIT A 236/H 6236); (b) Epoxy (SIKAPOWER-1277). [11]

The parameters of the materials, as shown in Tables 4.1, 4.2, 4.3 and 4.4, have a significant impact on correctly predicting the initiation and the evolution of damage in adhesively bonded joints. Since some of the parameters (highlighted in red with * symbol) were used to tune the model owing to the unavailability of experimental data, their effect on the force-displacement response, crack initiation and crack propagation response is most noticeable.

In finite element analysis, choosing interface stiffness parameters is crucial in terms of numerical stability and computational efficiency [31, 32]. A setter value too low may lead to stiffness instability in the system and numerical convergence difficulties. This is because low stiffness values may lead to large deformations at the interface, where non-physical oscillations and divergence of solution can occur. In order to avoid this, a very high interface stiffness is usually given to stabilize the simulations in surface-based cohesive approach. On the contrary, if the stiffness is too high, it will cause stiff system behaviour, so the numerical method will need smaller and smaller time steps to be stable, which also means more iterations and more costs. High stiffness values can lead to numerically stiff systems requiring implicit integration schemes or smaller time increments to resolve rapid variations. Hence, it is crucial to choose an appropriate interface stiffness for the simulations to strike a balance between numerical stability and computational efficiency [10, 36, 46]. Similar to the surface-based approach, in the element-based approach, the penalty stiffness [46] value was applied to the adhesive stiffness. For this purpose, the Young's modulus of the adhesive materials determined by experimental methods [11] was divided by the existing adhesive thickness (1.1 mm for polyurethane; 0.35 mm for epoxy) and penalty stiffnesses were calculated [46]. (Table 4.1, 4.2, 4.3, 4.4)

In the element-based cohesive method, the shear stiffness values tuned to 85 MPa for polyurethane and 2230 MPa for epoxy are crucial for simulating the adhesive resistance against shear deformation. This parameter plays a direct role in the Mode II energy dissipation and the strengthening of delamination. Too low shear stiffness would lead to underestimating the load transfer capability of the adhesive, while too high values could postpone lamination or suppress crack initiation in shear-dominated regions [10, 36].

The critical interface stress under tensile loading (Mode I) is defined as the threshold for damage initiation, which is 13.5 and 35 MPa for polyurethane and epoxy-based adhesives, respectively. These values were not tuned, they were obtained experimentally.

The shear stress at the interface is tuned to 12.5 MPa for polyurethane and 20 MPa for epoxy respectively. This parameter affects the ability of the adhesive to handle a combination of tensile and shear loads. Accurate shear stress tuning is particularly important in mixed-mode loading cases, such as in single-lap joints where the interaction of Mode I and II damage mechanisms must be taken into account [06, 09].

G_I and $G_{II,III}$, respectively, denote the energy release rates as the fracture energy required for cracking under both tensile (Mode I) and shear (Mode II and Mode III) loading. Polyurethane $G_{II,III}$ values (17 N/mm) are slightly higher than those of epoxy (13 N/mm) because polyurethane is a ductile material. Higher values (energy release rates) delay crack propagation, inducing gradual damage evolution.

The interaction between different damage modes is controlled by the power law exponent [38], which was tuned to 0.65 for polyurethane and 0.4 for epoxy. In fact, a higher exponent for polyurethane suggests that damage progression in mixed-mode is less influenced by the contributions of each mode, as it means that energy dissipation can be obtained in a more effective manner in mixed mode and across multiple modes. Conversely, the lower

value of epoxy suggests a more mode-specific damage evolution due to a higher sensitivity to the dominant mode (either Mode I or Mode II) [39, 29]. Careful tuning of this parameter leads to crack propagation paths that fit experimental observations.

Tuned parameters are crucial for experimental result replication, as they balance stiffness, stress thresholds, and energy dissipation pathways. For polyurethane, the modified parameters mimic its lower stiffness and ductility, while for epoxy, the increased stiffness and higher stress thresholds reflect its brittle nature. Properly calibrated parameters are critical to the performance of the cohesive zone models to correctly capture both damage initiation and propagation, providing meaningful force-displacement response and ZSP prediction.

Surface-based cohesive approach			
<u>Initiation</u>			
Interface Stiffness [MPa/mm]	Adhesive Shear Stiffness [MPa/mm]	Normal Interface Strength [MPa]	Shear Interface Strength [MPa]
K_n	K_s	$t_{n,0}$	$t_{s,0}$
10^6 *	95*	13.5	12.5*
<u>Evolution</u>			
Type	Softening	Mode Behaviour	
Energy	Linear	Power Law	
Mode I fracture toughness [N/mm]	Mode II,III fracture toughness [N/mm]	Exponent	
G_I	$G_{II,III}$	n	
2.3	17	0.65*	

Table 4.1: Tuned Traction-Separation Properties of Polyurethane for the surface-based approach

Element-based cohesive approach			
<u>Initiation</u>			
Normal Stiffness [MPa/mm]	Shear Stiffness [MPa/mm]	Normal Strength [MPa]	Shear Strength [MPa]
K_n	K_s	$t_{n,0}$	$t_{s,0}$
240*	85*	13.5	12.5*
<u>Evolution</u>			
Type	Softening	Mode Behaviour	
Energy	Linear	Power Law	
Mode I fracture toughness [N/mm]	Mode II,III fracture toughness [N/mm]	Exponent	
G_I	$G_{II,III}$	n	
2.3	17	0.65*	

Table 4.2: Tuned Traction-Separation Properties of Polyurethane for the element-based approach

Surface-based cohesive approach			
<u>Initiation</u>			
Interface Stiffness [MPa/mm]	Adhesive Shear Stiffness [MPa/mm]	Normal Interface Strength [MPa]	Shear Interface Strength [MPa]
K_n	K_s	$t_{n,0}$	$t_{s,0}$
10^6 *	892*	35	20*
<u>Evolution</u>			
Type	Softening	Mode Behaviour	
Energy	Linear	Power Law	
Mode I fracture toughness [N/mm]	Mode II,III fracture toughness [N/mm]	Exponent	
G_I	$G_{II,III}$	n	
2.5	13	0.4*	

Table 4.3: Tuned Traction-Separation Properties of Epoxy for the surface-based approach

Element-based cohesive approach			
<u>Initiation</u>			
Normal Stiffness [MPa/mm]	Shear Stiffness [MPa/mm]	Normal Stress [MPa]	Shear Stress [MPa]
K_n	K_s	$t_{n,0}$	$t_{s,0}$
6250*	2230*	35	20*
<u>Evolution</u>			
Type	Softening	Mode Behaviour	
Energy	Linear	Power Law	
Mode I fracture toughness [N/mm]	Mode II,III fracture toughness [N/mm]	Exponent	
G_I	$G_{II,III}$	n	
2.5	13	0.4*	

Table 4.4: Tuned Traction-Separation Properties of Epoxy for the element-based approach

4.2. Adherend Material Properties

The adherends used in this research were carbon fibre reinforced polymer (CFRP) composites. Carbon fibre is widely used in aerospace and automotive applications because of its very high strength-to-weight ratio, its resistance to fatigue, and the fact that the layup configuration can be customized. The mechanical behaviour of CFRP is influenced by fibre orientation and matrix properties, as well as interlayer interaction. (Table 4.5)

Orthotropic elastic materials were used to simulate the CFRP adherends in the finite element models, which enabled accurate prediction of directional stiffness and stress distribution. One of such key parameters defined in the model is orthotropic elastic

properties: Elastic modulus, shear modulus, and Poisson's ratios are defined in three principal directions.

<u>Property</u>	<u>Mean Value</u>	<u>Standard Deviation</u>
Density [kg/m ³]	1450	-
Poisson's Ratio	0.12	-
Longitudinal modulus [MPa]	58000	340
Longitudinal tensile strength [MPa]	440	16
Longitudinal tensile ultimate strain	0.0072	-
Longitudinal compressive strength [MPa]	453	36
Longitudinal compressive ultimate strain	0.096	-
Transverse tensile strength [Mpa]	440	16
Transverse compressive strength [Mpa]	453	36
In-plane shear modulus [MPa]	3900	-
In-plane shear strength [MPa]	72	-

Table 4.5: Material Properties of Adherends [11]

5. BOUNDARY CONDITIONS

Next to constitutive relations, boundary conditions are a core element of finite element modelling, as they describe how loads and constraints are applied to the system and have a direct influence on the simulation results. For adhesively bonded single-lap joints, boundary conditions must be correctly specified to accurately represent experimental conditions, represent load transfer at the bonded interface and accurately capture damage mechanisms such as Zero Strain Point detection.

For the numerical models developed in this study, boundary conditions were applied to simulate experimental tensile tests on SLJs [06, 09]. Specific constraints were applied at one end of the adherend while displacement-driven loading was applied at the opposite end. The simulation of actual joint behaviour was achieved through the implementation of boundary conditions between the 2D and 3D models that considered potential relative translation and rotation.

5.1. Boundary Conditions for 2D Models

5.1.1. Fixed End (Left Side)

All degrees of freedom (DOFs) at the left end of the joint were fully constrained to mimic the clamped boundary condition seen experimentally [06, 09]. The displacements U_x , U_y and the rotation θ_z were set to remain fixed, which inhibited motion or rotation in the longitudinal, transverse and rotational direction of the structure. This arrangement kept the left edge of the adherend fixed where tensile machine grips located while applying the load.

5.1.2. Loaded End (Right Side)

A ramped displacement function applied a displacement-controlled load to the right end of the adherend in the longitudinal direction (x -axis). This gradual displacement of the

model is helpful the smooth application of tensile loading which did not cause numerical instability. Only U_x was defined as displacement, so it accurately reflected the tensile deformation, while other rotational and lateral displacements were forbidden.

5.1.3. Symmetries for 2D Models

Plane strain conditions were assumed due to the large width-to-thickness ratio of the adherends. The out-of-plane displacement, U_z was set to zero to simulate the infinite width assumption and prevent any unintended displacement in the z axis (see Fig. 5.1). This assumption guarantees uniform stress and strain fields in the width direction.

5.2. Boundary Conditions for 3D Models

5.2.1. Fixed End (Left Side)

Like the 2D models, the left side of the adherend was restrained by the same constraint set ($U_x=U_y=U_z=0$ and $\theta_x=\theta_y=\theta_z=0$ (encastre boundary condition [10])). The set-up avoids any motion translation and rotation, mimicking the experimental clamped conditions. (see Fig. 5.2)

5.2.2. Loaded End (Right Side)

A ramp function was defined in the x-direction and a displacement-controlled load was applied incrementally. The amount of the imposed displacement was defined so that the loading rate was comparable to the experimental one, thus producing a gradual tensile loading of the joint. The displacements U_y and U_z and the rotations θ_x , θ_y and θ_z were constrained in order to keep the load in x direction of the test specimen. (see Fig. 5.2)

5.2.3. Off-Plane Boundary Conditions

Additional constraints were applied to prevent unexpected out-of-plane displacements and movements along the specimen width. All these conditions helped maintain the loading conditions in the 3D models in close resemblance with the experimental scene and hindered deformation along parasitic axes (see Fig. 5.2). This configuration effectively acted the deformation of the adhesive layer subjected to tensile loading without compromising computational stability.

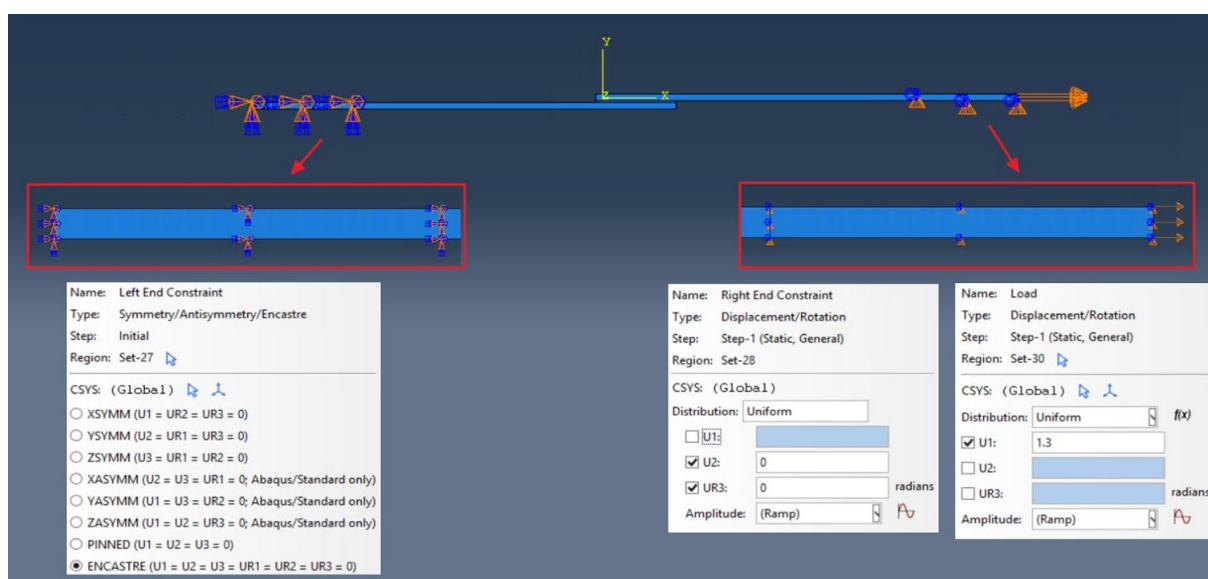


Figure 5.1: Boundary Condition for 2D Model

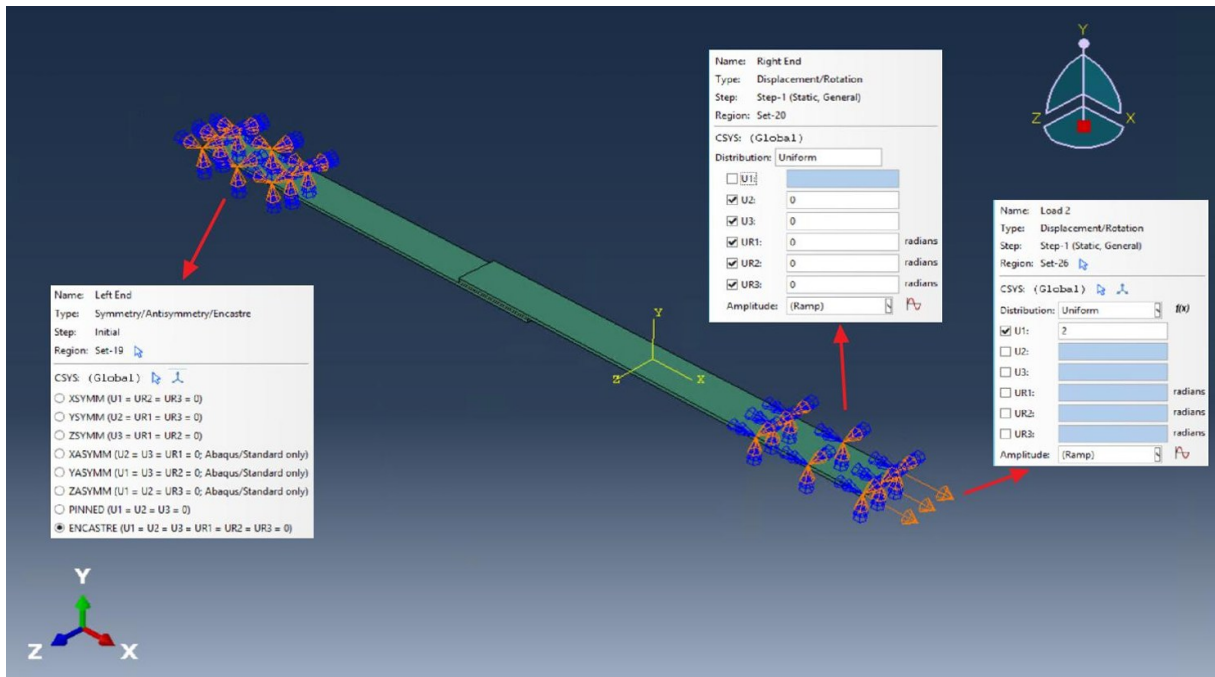


Figure 5.2: Boundary Condition for 3D Model

6. THEORETICAL BACKGROUND

An essential aspect of investigating adhesively bonded joints, especially in composite materials, is familiarity with the fundamental principles governing damage initiation, damage propagation, and the mechanics of bilinear traction-separation relationships [40, 41].

Adhesives are essential in defining the structural strength of the bonded joints, so modelling the adhesive mechanism under different types of loads is also very important. This part will formulate the main theoretical terms required to numerically simulate the mechanical response of such systems (e.g. via the finite element method) including damage initiation and damage propagation, which details how damage grows once it starts. An overview of the bilinear traction-separation law, a commonly employed technique for modelling the cohesive response of adhesives, is presented as well to highlight its role in simulations. A comprehensive understanding of these principles is key to predicting failure mechanisms and optimizing the design of bonded components.

6.1. Bilinear Traction-Separation Laws and Their Role in Simulations

The bilinear traction-separation law forms a key part of cohesive zone models for simulating damage initiation and propagation in adhesively bonded joints. This law describes the link between the cohesive tractions at the interface of the bonded materials and the respective separations, delivering a realistic insight of adhesive behaviour under different loading scenarios. The bilinear traction-separation law may not represent detailed constitutive behaviour in fracture processes. Its simplicity and its ability to capture at least the gross natural features of fracture processes have made it a widely used representation in finite element simulations [42, 43]. The theoretical foundation of the bilinear traction-separation law is discussed, its mathematical formulation, and its practical applications, as well as its limitations and potential enhancements.

In this case, the bonded joint usually fails in a mixed failure mode, combining both adhesive and cohesive failure mechanisms due to the progressive degradation of the adhesive layer [44]. The cohesive zone models govern the relationship between the stresses (tractions) present at the adhesive interface and the corresponding displacements (separation) to adequately capture this behaviour [42].

Some models, such as the bilinear traction-separation law, assume a critically damaging elastic separation of the adhesive interface which, beyond a maximum stress level, will start to fail and continue to degrade until failure [07, 42]. There are three distinct areas of the law:

1. **Elastic Region:** The first linear region with traction proportional to separation. In this region, the adhesive acts elastically, and the relationship between traction and separation is linear [07, 42, 46, 47,49]:

$$t = K\delta$$

The slope of this region is given by the cohesive stiffness, K . The point δ_0 represents the onset of damage, determined by the damage initiation criterion (e.g., quadratic stress criterion) [07, 42, 46, 47, 49].

2. **Softening Region:** A linear degradation of the traction as the separation δ increases beyond the damage initiation point δ_0 . Beyond this point, the traction decreases linearly as the separation increases, representing the gradual degradation of the adhesive [07, 42, 46, 47, 49]:

$$t = K\delta_0 \left(1 - \frac{\delta - \delta_0}{\delta_f - \delta_0} \right)$$

The energy dissipated during this phase corresponds to the fracture toughness of the adhesive and is equal to the area under the traction-separation curve [07, 42, 46, 47].

3. **Failure Region:** The point where the separation δ reaches δ_f the cohesive traction, t reaches zero, indicating complete failure. At this point, the cohesive traction reaches zero, indicating complete failure and separation of the adhesive interface [42, 46, 47].

The bilinear traction-separation relationship can be described mathematically as follows [07, 42, 46, 47, 49]:

$$t = \begin{cases} K\delta & \text{for } 0 \leq \delta \leq \delta_0 \\ K\delta_0 \left(1 - \frac{\delta - \delta_0}{\delta_f - \delta_0}\right) & \text{for } \delta_0 \leq \delta \leq \delta_f \\ 0 & \text{for } \delta \geq \delta_f \end{cases}$$

Where:

- t is the cohesive traction.
- δ is the separation displacement.
- δ_0 is the separation at damage initiation.
- δ_f is the separation at complete failure.
- K is the cohesive stiffness.

One of the key parameters in the bilinear traction-separation law is the fracture energy G , which represents the total energy required to propagate a crack through the adhesive. This energy is related to the area under the traction-separation curve and is given by [07, 42, 46, 47]:

$$G = \int_0^{\delta_f} t d\delta$$

For the bilinear law, this integral simplifies to [07, 42, 46, 47]:

$$G = \frac{1}{2} t_{max} \delta_f$$

t_{max} , where is the maximum traction corresponding to the onset of damage. The fracture energy is typically divided into its mode-specific components (Mode I, Mode II, and Mode III) for mixed-mode loading conditions [07, 42, 46, 47]:

$$G_{total} = G_I + G_{II} + G_{III}$$

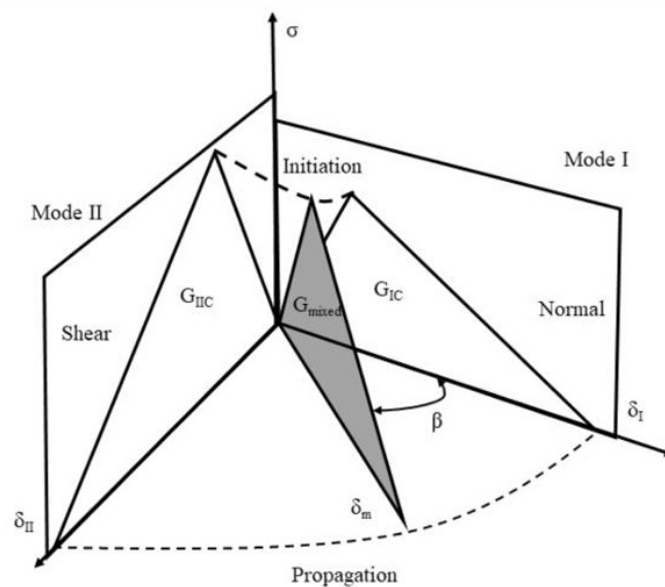


Figure 6.1: Mixed-mode failure envelope illustrating the interaction between Mode I and Mode II loading conditions [48].

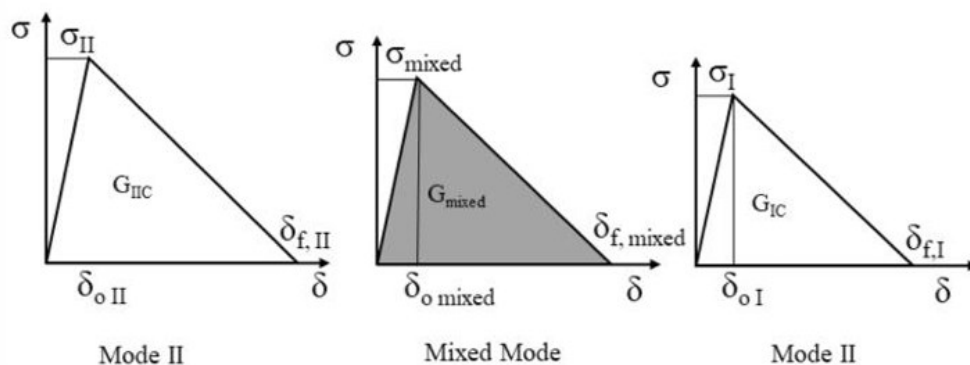


Figure 6.2: Bilinear traction-separation law depicting Mode I, Mode II, and mixed-mode fracture behaviours in cohesive zone models [48].

In finite element simulations, cohesive elements or cohesive interactions based on surfaces implement the bilinear traction-separation law. In both methods, the adhesive layer is modelled as a thin interface. Its mechanical response is described by a traction-separation relation [10].

In element-based cohesive method, these elements are located in between the adherends and defined through a bilinear traction-separation law. It guarantees that the softening/hardening of the adhesive is properly represented as the element stiffness matrix is updated at each step according to the current separation [10, 50].

Surface-based cohesive method is typically applied in thin adhesive layers, in which the definition of cohesive elements may be infeasible. The bilinear law is enforced through the contact interface between the adherend and adhesive, where the traction and separation are monitored at all integration points [10].

In simulations, the software checks the separation at every interface point and calculates the traction following the bilinear law. When the normal separation of elements exceeds, damage begins to develop, and the cohesive stiffness in the softening region of the law is progressively reduced [10, 42].

Under mixed-mode loading, the traction-separation law couples with damage initiation and damage propagation criteria including, but not limited to, theoretical quadratic stress criteria for initiation and theoretical propagation criteria such as a power law. The bilinear law gives the mapping from elastic behaviour to damage evolution, and the damage criteria determine when this transition happens and in which mode [07, 39, 47].

For instance, the quadratic criterion could initiate damage in a single lap joint when subjected to both tensile and shear, as it uses the combination of normal and shear stresses [08]. When damage is initiated, the bilinear traction-separation law defines the degradation of adhesive and the power law criterion controls the rate of damage progression [10].

Although this bilinear traction-separation law works well for many applications, it has some limitations, mainly when simulating adhesives that exhibit complex nonlinear behaviour. For ductile adhesives or adhesives with rate-dependent behaviour, the gradual damage process can be better described with other shaped softening curves [51, 52].

Bilinear traction-separation law is widely used for the simulation of mechanical response of adhesive bonded joint. The application of this phenomenological model is very easy and captures the main characteristics of an adhesive very well, which is the reason for its motivations to be used widely in cohesive zone models. As mentioned, by improving upon its shortcomings and introducing prominent material models, the predictive power of bilinear law could be considerably improved aiding towards design and optimization of robust bonded structures.

6.2. Damage Initiation: Quadratic Criteria

Damage initiation in adhesives bonded joints is an important phase of the structural integrity analysis, including fiber-reinforced polymers and adhesive. This damage initiation is

considered the transition point from elastic behaviour to damage and possibly ultimate failure. In cohesive zone modelling studies, accurate prediction of the initiation point is critical for creating meaningful results and depends heavily on criteria such as the quadratic stress criterion, being defined a priori. In this part, the background theory, mathematical formulations and numerical aspects associated with damage initiation in adhesively bonded joints are described using quadratic criteria [03, 10, 53].

The quadratic criterion depends on the incorporation of the various traction components that interact at the interface of the bonded materials. It confirms that either normal or shear stress can initiate damage when combined. This criterion can be written mathematically as [10, 45, 54]:

$$\left(\frac{\langle t_n \rangle}{t_{n,0}}\right)^2 + \left(\frac{\langle t_s \rangle}{t_{s,0}}\right)^2 + \left(\frac{\langle t_t \rangle}{t_{t,0}}\right)^2 = 1$$

Where:

- $\langle t_n \rangle$: Macaulay bracket for normal traction stress ($t_n \geq 0$); compressive stresses ($t_n < 0$) are ignored.
- t_s : Shear traction stress in the first tangential direction.
- t_t : Shear traction stress in the second tangential direction.
- $t_{n,0}$, $t_{s,0}$, $t_{t,0}$: Peak (damage initiation) tractions for normal and shear directions.

The equation above can be interpreted as considering the interaction between normal and shear components in the context of mixed-mode loading conditions, which is essential for edge cracks. If any individual term ≥ 1 , or their collective impact satisfies the equality, damage initiation occurs [10, 54].

The formulation of the quadratic criterion takes into account the synergistic interaction of normal and shear stresses in an adhesive layer. An example of this is a single lap joint experiencing both tensile and shear forces, which causes the adhesive to have normal stress and shear stress applied to it, neither of which on their own would cause the adhesive to fail. Rather, the contribution of each of these stresses, as described by the quadratic criterion collectively, is a realistic predictor of where and when damage initiates [54, 55, 56].

What this means in practice is that normal stress below the threshold could still lead to damage initiation if the shear stresses are high enough (and vice versa). Behaviour that varies in different directions can lead to complex stress profiles, especially in composite structures [54, 55, 56].

The quadratic criterion is usually embedded in cohesive elements or surface-based cohesive formulations in finite element simulations with cohesive zone models [10, 58, 59]. The cohesive zone model describes the adhesive layer using a traction-separation curve, and its linear range corresponds to the elastic response, while the damage initiation criterion leads to an evolution of the softening region [42, 59, 60].

The traction components at each cohesive element are monitored throughout the course of a finite element simulation (e.g., in Abaqus) [10]. It is declared that a damage initiation occurs when the quadratic criterion is satisfied and the cohesive stiffness degradation starts according to the chosen damage evolution law [57].

In most application cases, bonded joints are subjected to mixed-mode loads consisting of Mode I (opening), Mode II (in-plane shear), and Mode III (out-of-plane shear). The quadratic criterion is particularly appropriate since it implicitly incorporates the interaction between normal and shear stresses [61, 62].

The cohesive parameters in the model, including, in particular, the peak tractions and the cohesive stiffness, need to be properly calibrated to provide an accurate prediction of damage initiation. Usually, these parameters are defined by experimental test, such as lap-shear tests or peel tests and then, numerical fitting to experimental results is performed [63].

For many simulation models, a sensitivity analysis is carried out to assess how changes of these parameters impact the simulation outcome [64]. For example, increasing the cohesive stiffness can make for a stiffer adhesive response, as well as a delayed initiation of damage, and vice versa, which may lead to premature initiation and over-prediction of failure [65].

Here, the case of normal and shear stress interaction of quadratic type is considered which is valid only for isotropic adhesive - the one that has the same properties in all directions. Conversely, actual adhesion elements, especially from complex adhesive microstructures, display anisotropic or nonlinear stress interactions. Moreover, the quadratic criterion does not include the rate-dependent behaviour and the effects of external environmental variables such as temperature and humidity explicitly. The predictive capabilities of the damage initiation criterion could potentially be improved by the inclusion of viscoelastic or environmental models [66].

For the single lap joint model, which is introduced in this work, quadratic criterion is used for polyurethane (ADEKIT A 236/H 6236) and epoxy (SIKAPOWER-1277) adhesives. The peak tractions were determined through the calibration of experimental tensile tests, and the value of the cohesive stiffness was tuned to get reasonably close to numerical and experimental force-displacement curves.

The performance of well-known damage initiation criteria, such as the quadratic criterion, has been realized to predict damage initiation in these joints under mixed-mode

loading conditions. Additionally, coupling this method with cohesive zone models and traction-separation laws allows for precise modelling of adhesive failure processes. The predictive accuracy of the criterion can be improved to some extent when it is addressed to its limits and introduce complementary models, which can support the design and optimization approaches for reliable bonded structures [42].

6.3. Damage Propagation: Power Law Criterion

The power law function criteria is essentially an energy-based function (whereas stress-based like quadratic criteria, are only meant for initiation of damage). When damage initiation is detected, the energy release rates are continuously monitored. These rates indicate the energy available to drive crack propagation under each loading mode. Damage propagation initiates after satisfying the power law criterion for energy release rates [10, 67].

The total energy dissipated in damage propagation is represented by the area under the traction-separation curve in cohesive zone models. (Fig. 6.1) A bilinear or trapezoidal traction-separation law is often used, and the softening segment represents the gradual decay of cohesive forces [42, 68].

The accumulation of damage in an adhesively bonded joint is a function of several factors, including joint design, the structure of the adhesive and interface zones, environmental effects, and substrate material properties [69, 70]. Once damage initiation occurs in an adhesively bonded joint, the subsequent propagation of damage becomes a vital consideration in the overall structural failure. Damage propagation refers to the propagation of damage from the location where the damage initiates through the adhesive layer until total failure or interfacial separation occurs. One method that is widely used to model this

damaging phase of evolution is the power law criterion. The power law criterion is discussed in detail, theoretically and mathematically, in cohesive zone models in the following sections.

The power law criterion controls the development of damage corresponding to energy release rates for different failure scenarios. The power law criterion is employed for the prediction of damage under mixed-mode loading, as the energy release rates associated with normal (Mode I) and shear (Mode II) loading cooperate in contributing to the damage process [07, 42, 46, 47].

$$\left(\frac{G_I}{G_{Ic}}\right)^p + \left(\frac{G_{II}}{G_{IIc}}\right)^p + \left(\frac{G_{III}}{G_{IIIc}}\right)^p = 1$$

Where:

- G_I, G_{II}, G_{III} : Energy release rates for Modes I, II, and III.
- $G_{Ic}, G_{IIc}, G_{IIIc}$: Critical energy release rates for each mode.
- p : Power law exponent (material-dependent).

The power law exponents determine the relative contributions of the different modes to the damage evolution. For adhesives with higher shear strength, values of p may be larger, highlighting the contribution of Modes II and III. This is for brittle adhesives whose failure is mainly tensile but now may dominate [71, 72, 73].

In fact, cohesive zone models are key hardware used in finite element simulations, which aim to capture the strain-softening behaviour of adhesive interfaces. The energy lost in the damage propagation phase is controlled by the softening of the cohesive stiffness when the damage variable α increases. The damage variable goes from 0 (no damage) to 1 (ultimate failure) and develops according to the power law criterion [74].

The traction-separation law is amended to include damage influence in the following form:

$$t = (1 - \alpha).t_0$$

Where:

- t is the current traction.
- t_0 is the initial traction before the damage.
- α is the damage variable.

The damage variable evolves driven by the energy release rates and the critical fracture energies. In this way, damage propagates gradually while being consistent with the loading conditions and adhesive material properties [74].

Mixed-mode fracture is common in adhesively bonded joints and even more so in the case of aerospace or automotive applications where complex loading occurs. The combined effect of multiple mode failures can be coordinated using the available (power law criteria in issue) thus, the power law criterion is an ideal criterion for modelling of mixed-mode fracture [10, 75].

The coupling of Modes I and II can be illustrated by means of a failure envelope given in the G_I - G_{II} plane, where the boundary corresponds to the combinations of energy release rates that fulfill the power law condition. The equivalent work of breaking per joint area reflects the sensitivity of the adhesive to load alignments and allows for an optimal joint design [7, 46].

On the other hand, for making accurate predictions on the numerical damage propagation, the power law exponent [79] and the critical fracture energies G_{IC} , G_{IIC} , G_{IIIC}

have to be well tuned. These parameters are usually determined from experimental tests (e.g., mode-mixed fracture toughness tests) [75] and then adjusted.

The prediction of damage propagation has been demonstrated as sensitive to both mesh size and element type in finite element simulations. Cohesive elements need to be fine enough to model gradual damage accumulation, but not so small as to lead to computational cost. Surface-based cohesive interactions are often considered in thin adhesive layers to overcome mesh dependency issues [65, 76].

Although the power law criterion is a sound principle for modelling damage propagation, it has limitations. It assumes that the release rates of energy are independent on the growing direction of the crack and that the adhesive behaves isotropically, for instance. However, adhesives are typically anisotropic or rate-dependent which can cause prediction errors [77].

To overcome these restrictions, some advanced models which consider directional dependency and rate effects have been developed recently. Cohesive zone models can also be used in accordance with viscoelastic model to more accurately characterize time-dependent behaviours. [78]

The power law criterion has been widely used in many industrial applications, for example, for the design of adhesively bonded joints for aerospace and automotive applications. [80] For the polyurethane adhesive (ADEKIT A 236/H 6236), the power law exponents were determined to stress the ductile behaviour of the adhesive in the mixed-mode loading. Due to the relatively brittle nature of epoxy adhesive (SIKAPOWER-1277), the exponent has been modified as well. This is, together with the progressive area of damage propagation and the progressive loss in load-bearing capacity, captured quite well by cohesive zone models.

This proved to be an effective parameter under mixed-mode loading as well [79], and has been used extensively for damage propagation modelling in adhesively bonded joints. By enabling a coupled approach with cohesive zone formulations, it can accurately simulate the progressive degradation in adhesive films and assist with the design and optimization of strong bonded systems. The predictive accuracy of the power law criterion [79] can be further improved by addressing its shortcomings and developing advanced material models.

7. RESULTS

The numerical models presented in this study are built to mimic the experimental conditions and findings described in [6] and [9], where Abbasi, Ciardiello, and Goglio investigated damage initiation in adhesively bonded joints with the use of backface strain techniques. Material properties, boundary conditions, and loading configurations were modified from their work, so that the simulations had geometries that closely match those used in experiments. Specifically, the adhesive types and joint dimensions mentioned in backface strain as an index to detect damage initiation were instrumental in defining the adhesive properties and overlap geometry in the models. Knowing and/or understanding if the present model is adequate for specific situations is critical so numerical analysis can be obtained. Using finite element methods in computer models like Abaqus, they can simulate damage initiation and propagation as well as failure mechanisms. In this study, a numerical investigation aims to compare the two most widely used modelling approaches in cohesive zone modelling, namely, surface-based cohesive models and element-based cohesive models. The implementation of these models varies significantly in terms of computational efficiency and their capacity to accurately capture adhesive behaviour. Moreover, a mesh convergence study is conducted for ensuring that the numerical results are accurate and do not depend on mesh size, which is an important step in obtaining reliable simulations.

7.1. Design of Experiments for Single-Lap Joint Specimens

The design of the experimental test setup of single lap joints is the basis for numerical simulations performed in this thesis. Current work experimental configurations were adopted from [9], "A novel approach for damage assessment in adhesively bonded composite joints using backface strain technique" and [6], "Backface strain as index to detect damage initiation in composite single-lap bonded joints: Effects of adhesive type and joint dimensions" by

Abbasi, Ciardiello and Goglio. The joint geometry and adhesive properties were shown to affect mechanical performance and zero-strain point, used for detecting damage [6], [9].

Figure 7.1 shows the geometric parameters for the single-lap joint specimens in the experiments. The basic overall dimensions of SLJ configuration are defined by overlap length L , adherends' thickness T , and joint width W . The thickness t of adhesive is assumed to be 1.1 mm for polyurethane and 0.35 mm for epoxy, according to experimental designs in Abbasi et al. 's studies [06, 09]. It establishes the foundation for the assessment of strain distributions, zero-strain point responses and dynamic initiation of damage due to tensile loading.

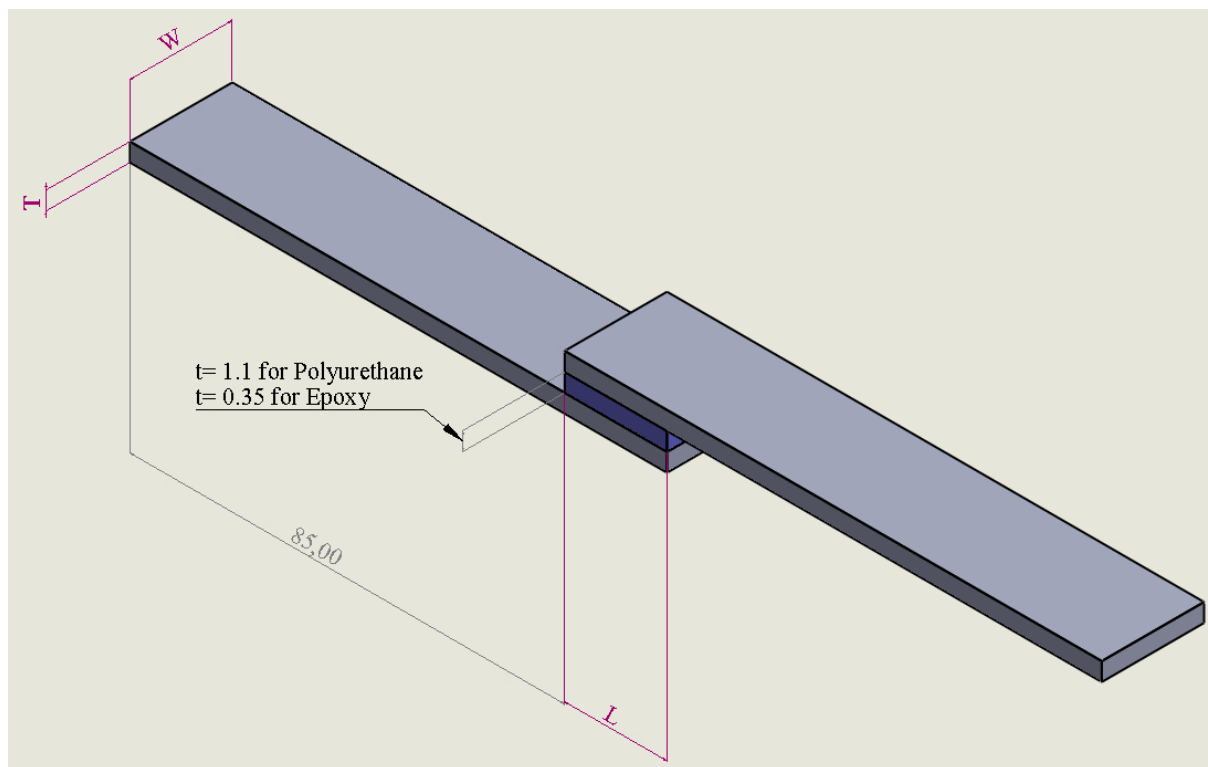


Figure 7.1: Geometric Configuration of the Single-Lap Joint Specimen (Based on Abbasi et al., A novel approach for damage assessment in adhesively bonded composite joints using backface strain technique [09] and Backface strain as index to damage initiation in composite single-lap bonded joints: Effects of adhesive type and joint dimensions [06])

		T1 (1.76 mm)	T2 (3.52 mm)
L1 (10 mm)	W1 (10 mm)	L1W1T1	L1W1T2
L1 (10 mm)	W2 (20 mm)	L1W2T1	L1W2T2
L1 (10 mm)	W3 (30 mm)	L1W3T1	L1W3T2
L2 (20 mm)	W1 (10 mm)	L2W1T1	L2W1T2
L2 (20 mm)	W2 (20 mm)	L2W2T1	L2W2T2
L2 (20 mm)	W3 (30 mm)	L2W3T1	L2W3T2

Table 7.1: Single-Lap Joint Design of Experiments (Based on [6], "Backface Strain as an Index to Detect Damage Initiation in Composite Single-Lap Bonded Joints: Effects of Adhesive Type and Joint Dimensions,")

		T1 (0.88 mm)	T2 (1.76 mm)	T3 (3.52 mm)
L1 (10 mm)	W1 (10 mm)	L1W1T1	L1W1T2	L1W1T3
L1 (10 mm)	W2 (20 mm)	L1W2T1	L1W2T2	L1W2T3
L1 (10 mm)	W3 (30 mm)	L1W3T1	L1W3T2	L1W3T3
L2 (20 mm)	W1 (10 mm)	L2W1T1	L2W1T2	L2W1T3
L2 (20 mm)	W2 (20 mm)	L2W2T1	L2W2T2	L2W2T3
L2 (20 mm)	W3 (30 mm)	L2W3T1	L2W3T2	L2W3T3

Table 7.2: Single-Lap Joint Design of Experiments (Based on [9], "A Novel Approach for Damage Assessment in Adhesively Bonded Composite Joints Using Backface Strain Technique,")

Increasing the adhesive layer thickness would have a relevant influence directly related to its mechanical strategies. Table 7.1 shows the configurations from the first

experimental study, with emphasis on two levels of thickness (T1 and T2) while Table 7.2 shows configurations that add another thickness level in order to extend the scope of the analysis.

In the first test setup, the adhesives were ADEKIT A 236/H 6236 (polyurethane) and SIKAPOW-1277 (epoxy) (Table 7.1), while in the second test setup, only ADEKIT A 236/H 6236 (polyurethane) was used. (Table 7.2). The adherend thickness varied from 1.76 mm to 3.52 mm in the first test setup, while in the second test setup the adherend thickness varied from 0.88 mm to 3.52 mm. That difference in adherend thickness and different type of adhesives analyses how stiffness, or elongation, or ductility governs the overall joint performance (initiation and propagation of cracks).

The strain in both joints was monitored with high spatial resolutions along the overlap length using digital image correlation (DIC) techniques in both experimental works [06, 09]. The ZSP was determined by the shifted evaluation of the change from tensile to compressive strain at the backface of the adherend. Configurations were designed to investigate how width and length of the adhesive and width, length and thickness of the adherend affect the location of the ZSP as well as the mechanisms of failure.

By reproducing these experimental conditions in the finite element models, this thesis aims to catch those important mechanical phenomena occurring in the fracture process, such as stress field distribution, strain localization or damage propagation, are accurately reproduced. The mechanical response at tensile load conditions used the properties of the materials, including the Young's modulus, Poisson's rate, and fracture energy of the adhesive and adherends in the numerical models.

These experimental design approaches not only facilitate the validation of cohesive zone models but also offer valuable information about optimal adhesive joint configurations for enhanced structural performance.

7.2. The Force-Displacement Analysis of Pu-L2W2T2

Tuning material properties is an important part of confirming that numerical simulations accurately represent force-displacement behaviour in the experiments on adhesively bonded SLJs. The configuration of specimen for tuning was selected as L2W2T2 (L=20mm, W=20mm and T=1.76mm) bonded with polyurethane adhesive. This configuration was chosen because it is representative of moderate geometric dimensions and material properties, which makes it suitable to calibration.

Table 7.3 lists the values of the area under the force-displacement curve of the experimental results in comparison with the numerical results obtained during this study for the L2W2T2 specimen under tensile loading and the percentage error, which indicates how much they deviate from each other. Figure 7.2 shows the comparison of the experimental and numerical force-displacement curves. The experimental data are shown in the form of three different force-displacement curves (Experimental 1, 2, and 3), which account for small differences due to experimental inaccuracies and material inhomogeneity. The numerical simulations are divided into two-dimensional and three-dimensional models using both the triangular traction-separation laws and coherent element and cohesive surface approach.

The areas under the force-displacement curves (representing the total energy absorbed up to failure), to allow comparison in quantitative terms, were calculated for each experimental and numerical case. This metric is vital in determining the energy dissipation ability of the adhesive joint and its performance state with respect to mechanical loading.

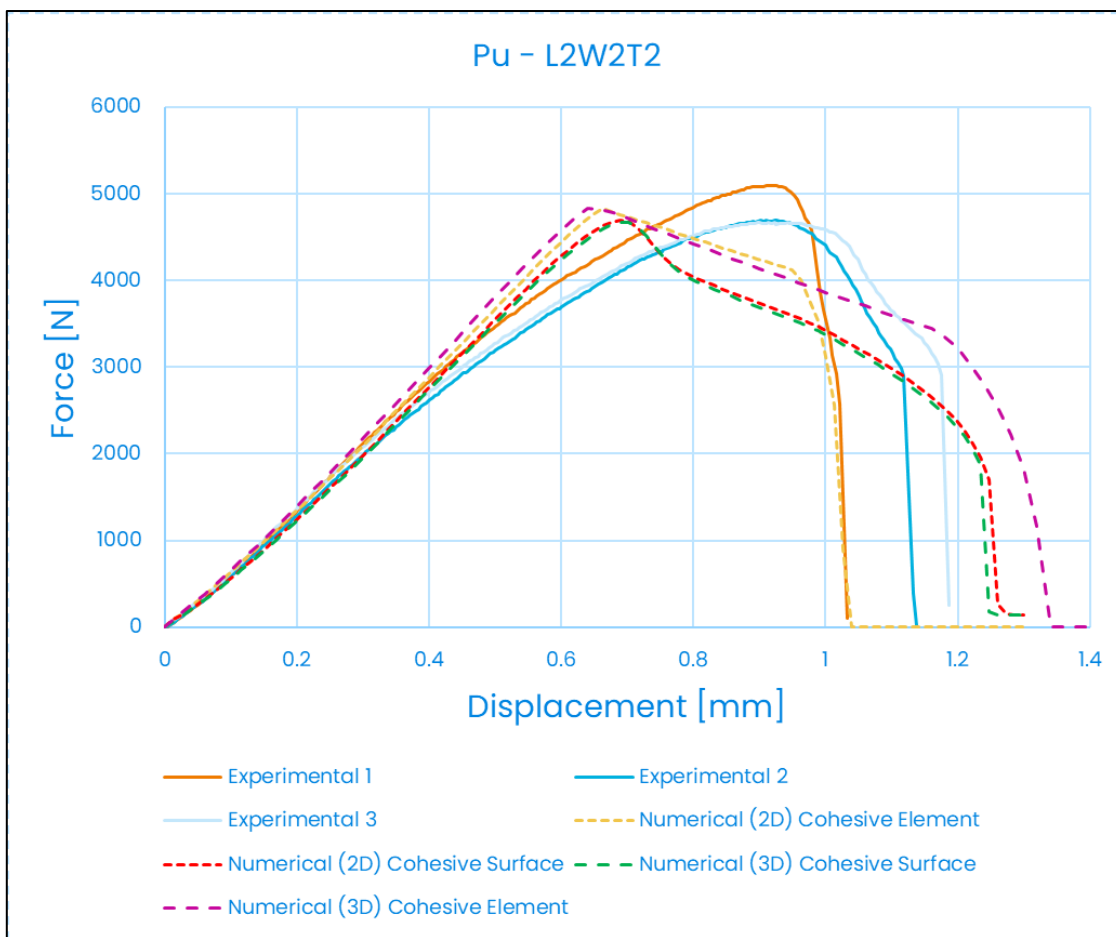


Figure 7.2: Comparison of Force-Displacement curve of Pu-L2W2T2 specimen with different techniques

The calculated results of the energy absorption are presented in Table 7.3. The average experimental energy absorption was 3324.27 N·mm based on three experimental tests. The corresponding energy values from the numerical simulations differ with varying errors, dependent on the modelling approach taken.

	Energy [N·mm]	Error (%)
Experimental 1	3126.90	-
Experimental 2	3351.05	-
Experimental 3	3494.86	-
Experimental Average	3324.27	-

Numerical (2D) Cohesive Element	3114.36	6.3
Numerical (3D) Cohesive Element	4111.59	23.7
Numerical (2D) Cohesive Surface	3568.44	7.34
Numerical (3D) Cohesive Surface	3502.91	5.3

Table 7.3: Energy Absorption and Error Comparison for L2W2T2 Specimen

With the minimum 5.3% error compared to the experimental average, the most accurate results were obtained with the cohesive surface method, where the 3D cohesive surface model was developed. The 2D cohesive surface model also performed fairly well, with an approximately 7.34% error, which is tolerable for numerical simulations. On the other hand, the element-based models with a bonded contact between the elements showed much larger errors, especially in the 3D case, resulting in a deviation of 23.7%. This difference arises from the greater sensitivity of cohesive element models to mesh refinement and the additional degrees of freedom that the cohesive element models require to accurately describe through-thickness adhesive behaviour. In the 2D cohesive element model, this deviation is 6.3%.

The tuned material properties provided a good correlation between experimental and numerical force-displacement responses using the cohesive surface method on L2W2T2 specimen. The error analysis also corroborates the tuning behind the procedure, as the 3D cohesive surface model produced the most accurate energy absorption estimation. These tuned characteristics will be used to the broader population of specimens considered in this thesis to ensure consistency across configurations.

7.3. The Zero Strain Point Analysis of Pu-L2W2T2

The ZSP helps in gaining insight into the strain distribution and load transfer mechanisms in the overlap length of the adhesively bonded SLJs. For this work, a specimen

L2W2T2 ($L=20\text{mm}$, $W=20\text{mm}$ and $T=1.76\text{mm}$) was selected for ZSP analysis using both experimental and numerical approaches. ZSP is the point that marks the transition between tensile and compressive strains, which is critical during damage initiation and propagation stages.

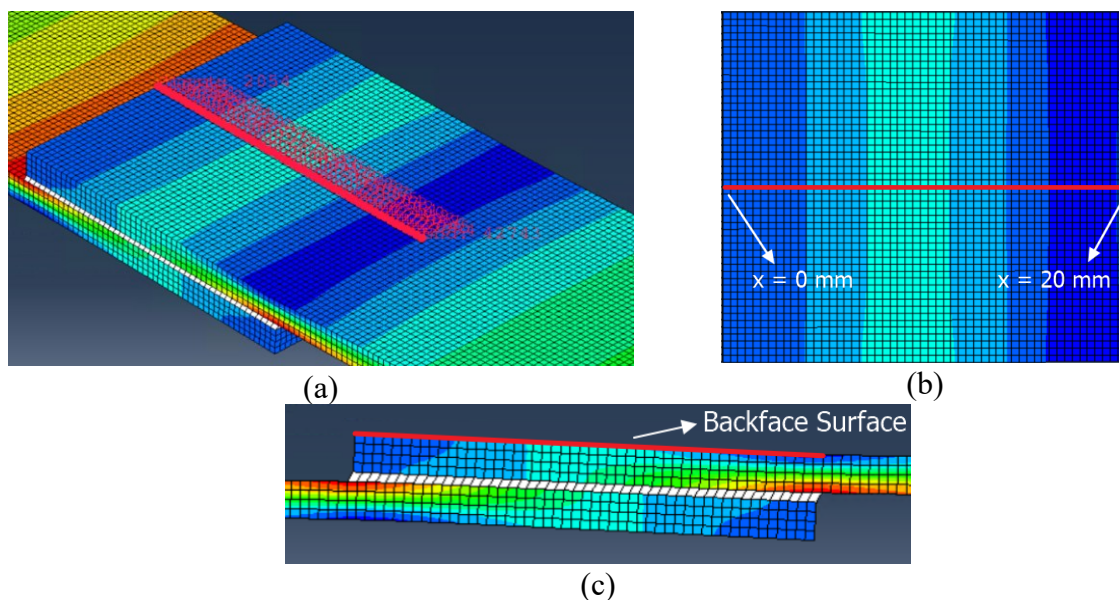


Figure 7.3. Position of the Zero Strain Point Measurement: (a) and (b) are for the 3D model, (c) for the 2D model.

Figure 7.3 shows the numerical setup for measuring ZSP on the backface of the bonded joint for 2D and 3D models. The strain was measured along the x-axis and was distributed over the entire length of the overlap, which was 20 mm, where 0 mm ($x=0$ mm) corresponded to the start of the overlap in the specimen L2W2T2, while 20 mm ($x=20$ mm) indicated its end. The backface surface, indicated for strain evaluation (as shown in section 3), is used as a reference position for ZSP monitoring under varying loading conditions.

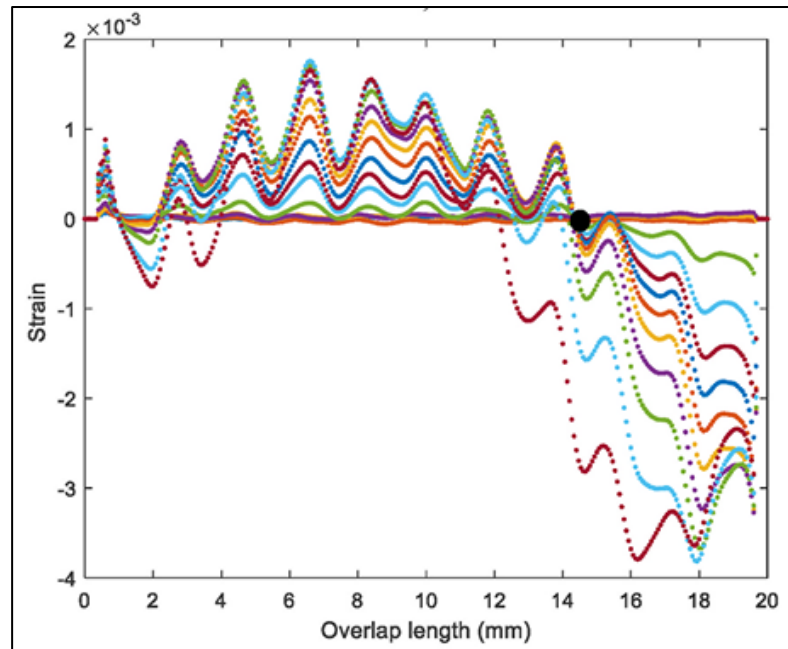


Figure 7.4: Experimental Strain Distribution along the Overlap Length of L2W2T2 Specimen under Various Load Levels (Adapted from "A novel approach for damage assessment in adhesively bonded composite joints using backface strain technique") [09]

Experimental results from [9], "A novel approach for damage assessment of adhesively bonded composite joints using backface strain technique", are shown in Figure 7.4. This shows the progressive nature of damage initiation and as evidence the ZSP location, as seen in the experimental data, shifts with increased load. Since initially the ZSP lies near to the free end of the overlap under low loading conditions, along with the increase of load, it transfers to the middle of the overlap.

Figure 7.5 shows the predicted strain contour in the adhesive using 2D cohesive surface approach. The strain distribution is shown for the cohesive surface-based model which is calibrated against the L2W2T2 specimen. The results show a close agreement with the experimental trends and they also suggest an accurate prediction of the ZSP. The numerical findings reveal an early ZSP close to the free end of the overlap, while progressive

displacement towards the centre occurs with increasing load, in accordance with experimental observations.

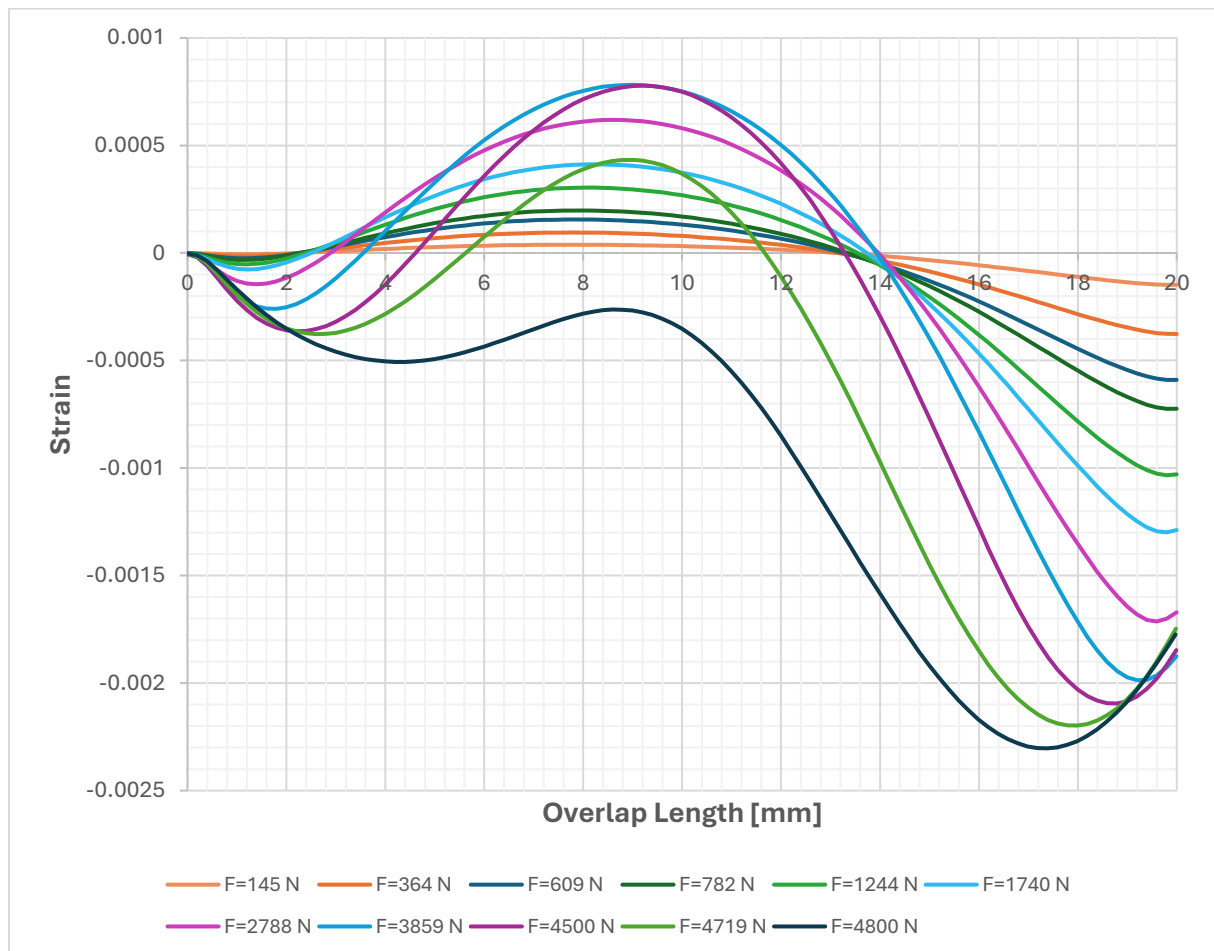


Figure 7.5: Strain Distribution over the Overall Length along the Adhesive to detect ZSP for Pu-L2W2T2, Numerical result

The ZSP location was identified from the numerical model at approximately 14 mm of the overlap length, which validated the ZSP testing of the L2W2T2 specimen. This position is consistent with the experimental readings described in [9], "A novel approach for damage assessment in adhesively bonded composite joints using backface strain technique". The correct identification of the ZSP confirms the model's ability to represent the critical load

transfer point within the adhesive joint, a fundamental parameter of interest for damage initiation predictions.

The relationship between strain and load-displacement for L2W2T2 bonded with polyurethane is shown in Figure 7.6, indicating the main mechanical behaviours in function of tensile load increase. An important aspect to keep in mind is the behaviour of the ZSP to maintain zero strain up to peak load during experimental test. However, in numerical results, although the strain value approaches zero strain up to peak load, it is seen that it is non-linear due to the complexity of modelling the ductile nature of polyurethane.

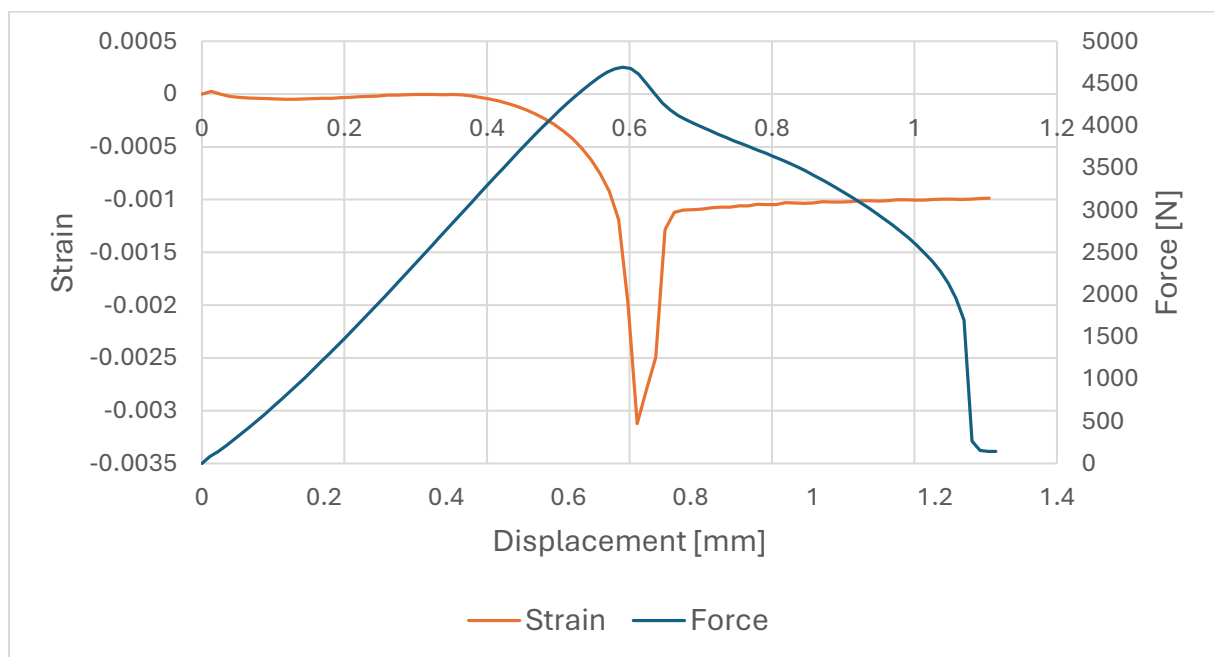


Figure 7.6: Strain distribution of the Zero Strain Point (ZSP) at different load levels for L2W2T2, Numerical result

The change in strain distribution through the overlap length is shown at different load levels ($F=364\text{ N}$ - $F=4800\text{ N}$) in Figure 7.7. The ZSP for both the experimental measurements and previous numerical predictions occurs at approximately 14 mm during initial loading (F

= 364 N). Together with the observation that the resultant ZSP progressively migrates farther into the negative strain region as the applied load varies, a qualitative picture of the initiation and development of large plastic deformation emerges through the overlap length.

At elevated loads, specifically $F = 2788$ N and onwards, ZSP exhibits exacerbated negative strain, linking with the greater damage propagation in the adhesive and composite interface. This numerical model successfully captures such behaviour, which explains its capability of indicating a ZSP deformation with the general trends.

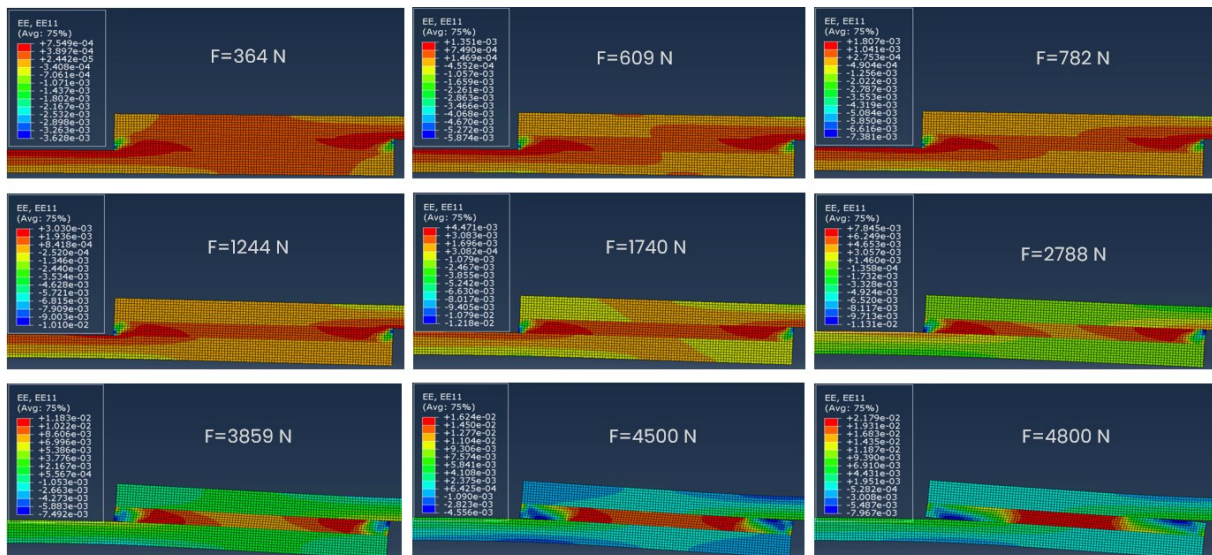


Figure 7.7: Evolution of Zero Strain Point (ZSP) Under Different Load Conditions for Pu-L2W2T2

7.4. Zero Strain Point Analysis for All Specimens

The systematic methodology followed for numerical modelling of different types of adhesive materials (polyurethane and epoxy) using cohesive element and cohesive surface methods has been summarized in an organized frame in Table 7.4. It covers three-dimensional (3D) and two-dimensional (2D) geometrical representations, bilinear traction-separation laws (TSL), and damage modelling criteria.

The adhesive layer is modelled with a bilinear traction-separation law for both polyurethane and epoxy adhesives, which well captures the adhesive layer's linear elastic, damage initiation, and progressive softening response.

Damage Initiation and Growth Criteria

- **Damage Start:** The onset of damage is based on the quadratic stress criterion. This criterion takes into account the combined effect of tensile and shear stresses to predict failure.
- **Damage Evolution:** An energy-based type of power law criterion governs the evolution of damage, allowing for the proper tracking of crack propagation under mixed-mode loading conditions.

Geometries Considered

- **Two-dimensional Analysis:** 2D models are sequentially investigated following cohesive element and cohesive surface techniques. This allows for fast and computationally inexpensive simulations that are accurate enough for first-order analysis.
- **3D Analyses:** Although 3D simulation provides a more accurate prediction of the joint's performance, the cohesive surface model was implemented for both materials. As previously mentioned in the section comparing experimental and numerical energy absorption and error margins (Table 7.3), the least satisfactory results were obtained in the 3D element-based method and also because this method is time-consuming, this method was not analysed for the remaining samples.

Adhesive Material	TSL Model	Damage Initiation Criteria	Damage Evolution Criteria	Geometry	Approach	Analysis Done
Polyurethane	Bilinear	Quadratic Stress Criterion	Power Criterion (Energy Type)	2D	Cohesive Element	✓
					Cohesive Surface	✓
				3D	Cohesive Element	-
					Cohesive Surface	✓
Epoxy	Bilinear	Quadratic Stress Criterion	Power Criterion (Energy Type)	2D	Cohesive Element	✓
					Cohesive Surface	✓
				3D	Cohesive Element	-
					Cohesive Surface	✓

Table 7.4: Summary of Approaches in this Study

7.4.1. The Results of 2D Surface-Based Approach

The numerical and experimental analyses were performed on the Pu-L1W1T1 specimen with 2D surface-based cohesive model and bilinear TSL modelled with its properties for a polyurethane adhesive. The adhesive had a length of 10 mm, a width of 10 mm, a thickness of 1.1 mm, and the adherend had a thickness of 0.88 mm. This comparison was developed to track the detection of the Zero Strain Point and investigate the behaviour of strains under different loads. The strain distribution along the overlap length for both experimental (Figure 7.8a) and numerical (Figure 7.8b & Figure 7.9) analyses confirms that the prediction for the ZSP location is correct. The numerically calculated ZSP position agrees reasonably with that determined experimentally with an acceptable relative deviation of ~10%. (Table 7.5)

The peak strain value has been underestimated in the numerical analysis as well, which happens -2.7×10^{-3} whereas the experimental value is -5×10^{-3} . The relative error in this case is 46%, which indicates that the strain amplitudes differ. This is successfully captured in the numerical simulation (Table 7.5). The model simplifies material behaviour, which causes strain values to be underestimated.

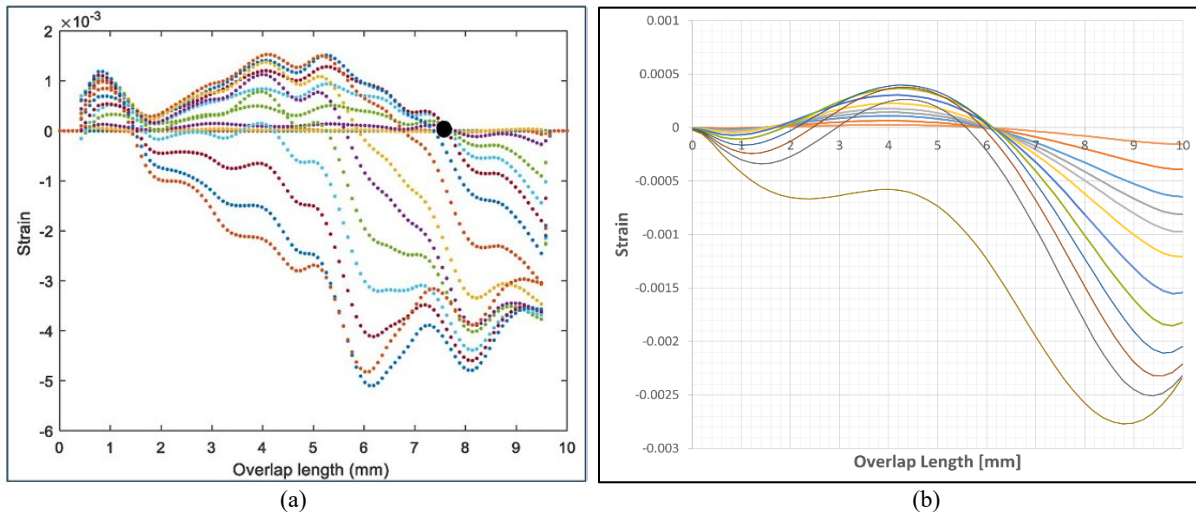


Figure 7.8: Strain Distribution on the Backface of Pu-L1W1T1 through Overlap Length under Different Loads for (a) Experimental [09] and (b) Numerical Results

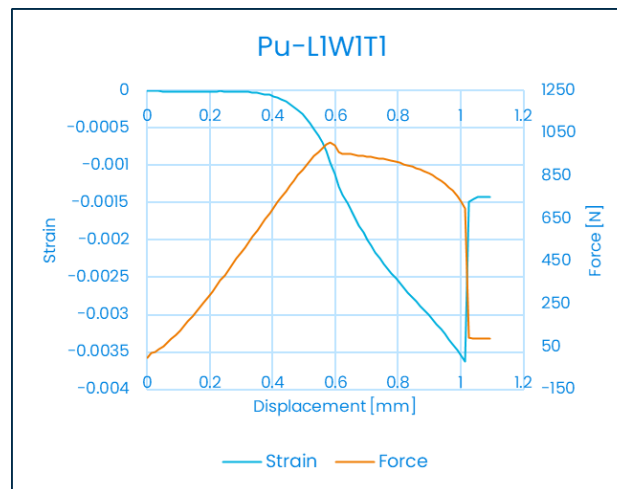


Figure 7.9: Strain-displacement and force-displacement curves for numerical result of Pu-L1W1T1

The 2D surface-based cohesive model with a bilinear traction-separation law was employed to describe the adhesive bonds of the Pu-L1W2T1 specimen. The adhesive had a length of 10 mm, a width of 20 mm, a thickness 1.1 mm, and the adherend had a thickness of

0.88 mm. This comparison was performed in order to assess Zero Strain Point detection as well as the strain behaviour under applied loads.

Both experimental (Figure 7.10a) and numerical (Figure 7.10b & Figure 7.11) analyses reveal strain distribution along the overlap length respectively and confirm accurate prediction of the ZSP location. The ZSP position obtained numerically closely matches the experimental value, and the relative error is acceptable (of the order of $\sim 10\%$) in the absence of any nonlinear Effect to be considered. (Table 7.5)

The maximum strain value is underestimated by numerical analysis up to -2.7×10^{-3} in comparison to the experimental value up to -7×10^{-3} . This corresponds to a relative error of 61%, pointing out the differences in strain amplitude. (Table 7.5)

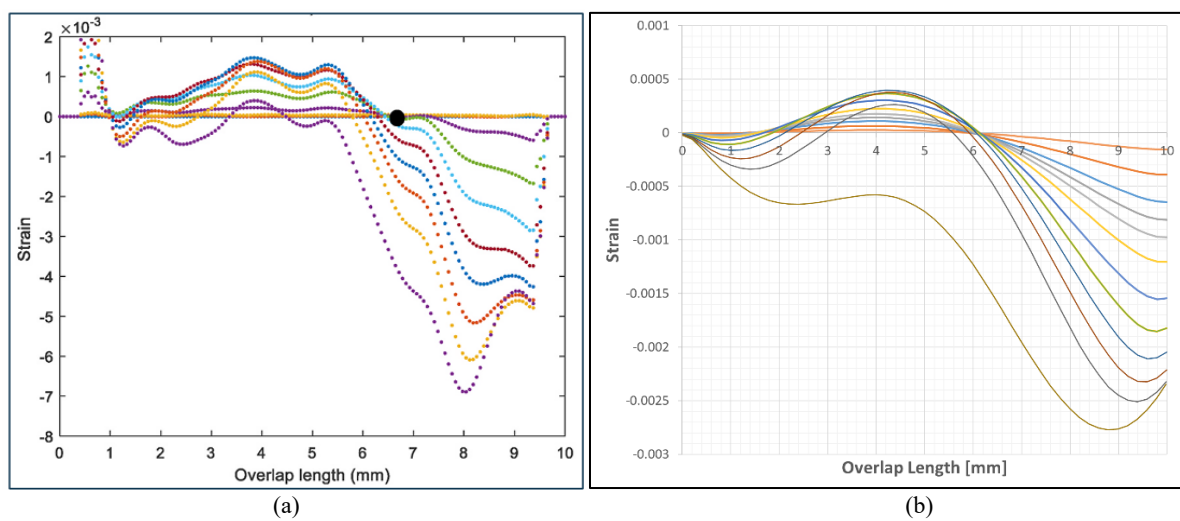


Figure 7.10: Strain Distribution on the Backface of Pu-L1W2T1 through Overlap Length under Different Loads for (a) Experimental [09] and (b) Numerical Results

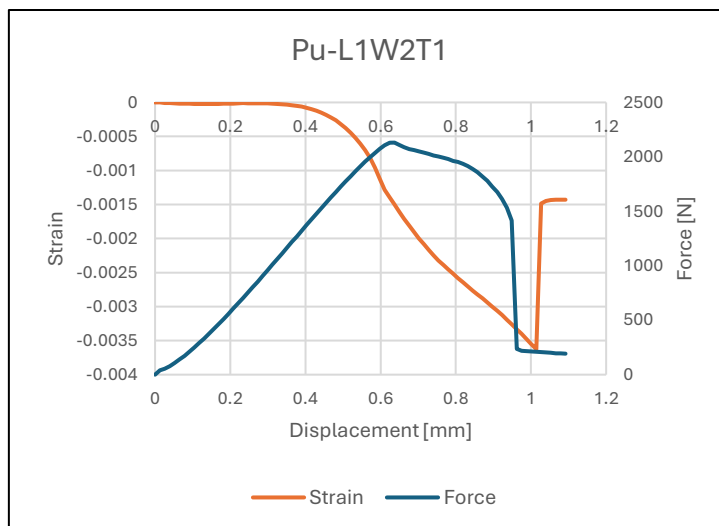


Figure 7.11: Strain-displacement and force-displacement curves for the numerical result of Pu-L1W2T1

The 2D surface-based cohesive model with a bilinear traction-separation law was employed to describe the adhesive bonds of the Pu-L1W2T2 specimen. The adhesive had a length of 10 mm, a width of 20 mm, a thickness 1.1 mm, and the adherend had a thickness of 1.76 mm. This comparison was performed in order to assess Zero Strain Point detection as well as the strain behaviour under applied loads.

The strain distribution along the overlap length from both experimental (Figure 7.12a) and numerical (Figure 7.12b & Figure 7.13) analyses shows complexities in investigating the precise ZSP position, leading to differences between experimental and numerical results. Despite this complex behaviour of the specimen, ZSP was detected in numerical analysis, albeit with difficulty. The strain results are a relatively good match and are still providing useful insights. From the numerical analysis, the maximum strain to be -2.7×10^{-3} is estimated, which is in close agreement with the -3×10^{-3} value observed experimentally. Relative error is 10% and this suggests a good performance of the analytical model in capturing strain amplitudes. (Table 7.5)

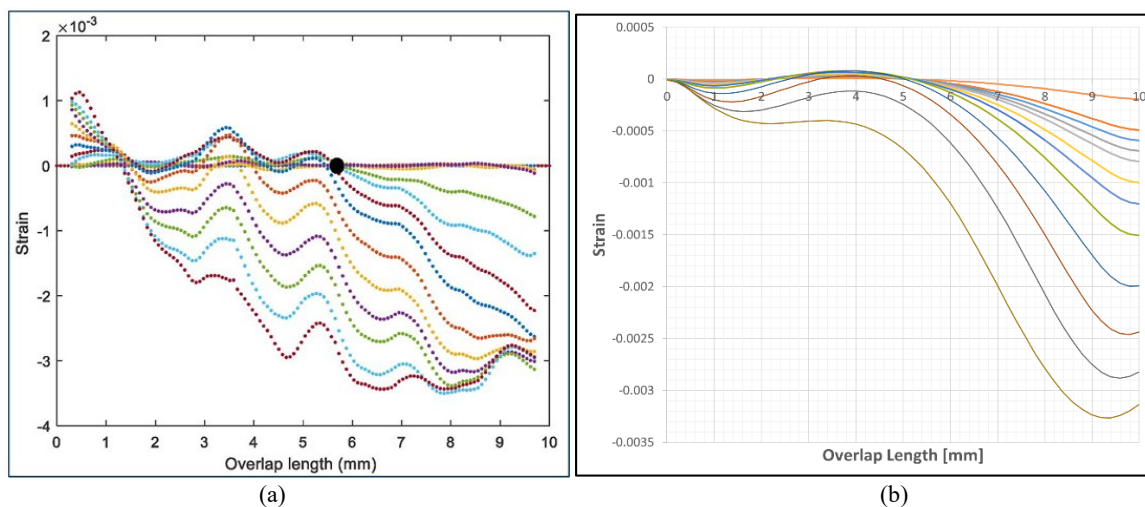


Figure 7.12: Strain Distribution on the Backface of Pu-L1W2T2 through Overlap Length under Different Loads for (a) Experimental [09] and (b) Numerical Results

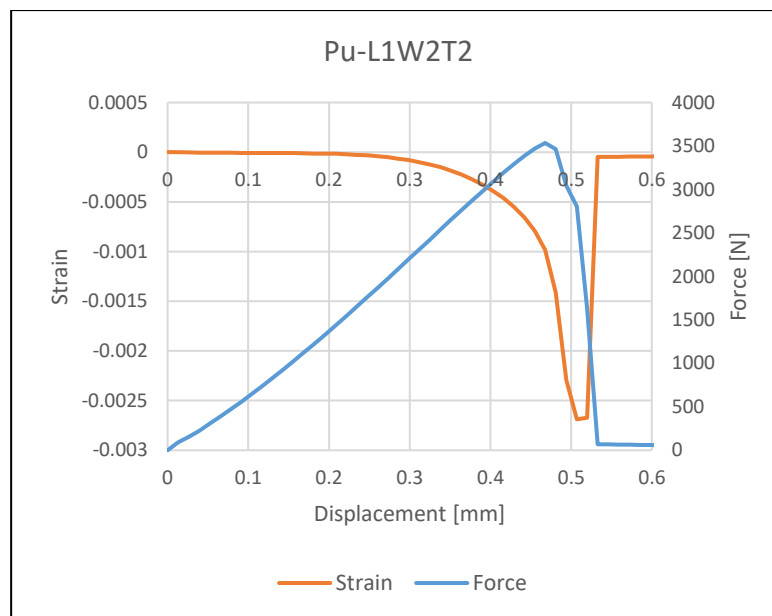


Figure 7.13: Strain-displacement and force-displacement curves for the numerical result of Pu-L1W2T2

The 2D surface-based cohesive model with a bilinear traction-separation law was employed to describe the adhesive bonds of the Pu-L1W2T3 specimen. The adhesive had a

length of 10 mm, a width of 20 mm, a thickness 1.1 mm, and the adherend had a thickness of 3.52 mm. This comparison was performed in order to assess Zero Strain Point detection as well as the strain behaviour under applied loads.

Both experimental (a) and numerical (b) strain distributions along the overlap length are shown in Figure 7.14 & Figure 7.15. Some difficulties in determining the precise location of the ZSP are indicated, with a difference between experimental and numerical results. Nevertheless, the strain values do match fairly well, and the quantities of interest are reflected well in the comparison. The maximum value of the strain is estimated to be -1.6×10^{-3} for the numerical analysis (compared to -2×10^{-3} in the experimental observation) (Table 7.5). The corresponding relative error is 17%, showing an acceptable behaviour of the model when reproducing strain amplitudes. (Table 7.5)

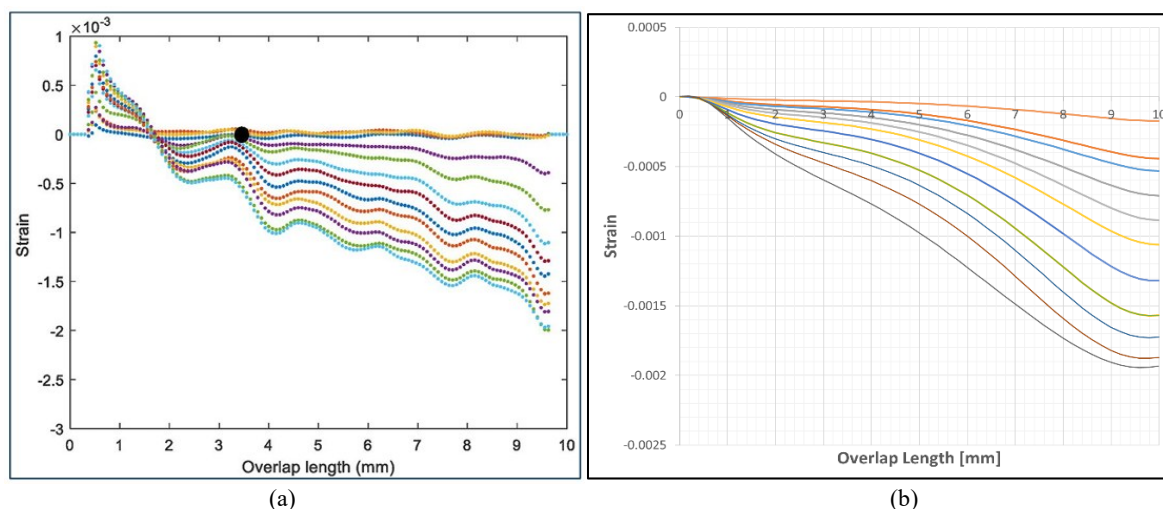


Figure 7.14: Strain Distribution on the Backface of Pu-L1W2T3 through Overlap Length under Different Loads for (a) Experimental [09] and (b) Numerical Results

The 2D surface-based cohesive model with a bilinear traction-separation law was employed to describe the adhesive bonds of the Pu-L1W3T1 specimen. The adhesive had a

length of 10 mm, a width of 30 mm, a thickness 1.1 mm, and the adherend had a thickness of 0.77 mm. This comparison was performed in order to assess Zero Strain Point detection as well as the strain behaviour under applied loads.

The strain evolutions along overlap length from both experimental (Figure 7.15a) and numerical (Figure 7.15b & Figure 7.16) determinations confirmed the identification of the ZSP position whereby numerical predictions closely matched with experimental measurements. This is where the ZSP location falls with a $\sim 16\%$ relative error, but it is still not a significant difference. (Table 7.5)

The maximum strain value has a value of -2.5×10^{-3} , while the experimental value was observed at -7×10^{-3} , which shows that numerical analysis would underestimate the strain value. This results in a 65% relative error. Despite this significant underestimation, the trend and strain evolution of the ZSP are predicted well in the numerical model, confirming that the numerical simulations are valid for predictive purposes.

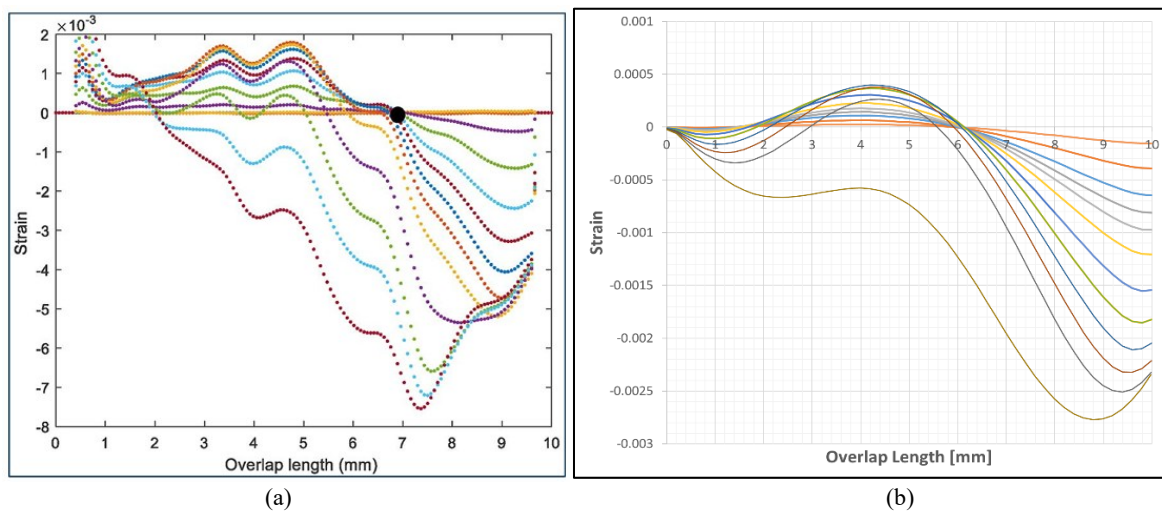


Figure 7.15: Strain Distribution on the Backface of Pu-L1W3T1 through Overlap Length under Different Loads for (a) Experimental [09] and (b) Numerical Results

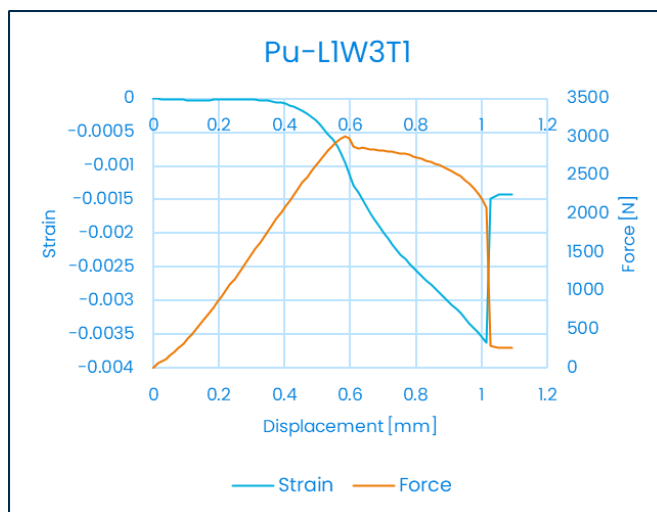


Figure 7.16: Strain-displacement and force-displacement curves for numerical result of Pu-L1W3T1

The 2D surface-based cohesive model with a bilinear traction-separation law was employed to describe the adhesive bonds of the Pu-L2W2T3 specimen. The adhesive had a length of 20 mm, a width of 20 mm, a thickness 1.1 mm, and the adherend had a thickness of 3.52 mm. This comparison was performed in order to assess Zero Strain Point detection as well as the strain behaviour under applied loads.

It is observed from the strain distribution along the overlap length obtained from experimental (Figure 7.17a) and the numerical analysis (Figures 7.17b & 7.18). The numerical model accurately determines the ZSP position with minor deviation according to the results.

The maximum of strain value calculated with numerical analysis is close to the experiment result which is -2.1×10^{-3} versus -2.6×10^{-3} . The related relative error is 19%, indicating that strain estimation is accurate. (Table 7.5)

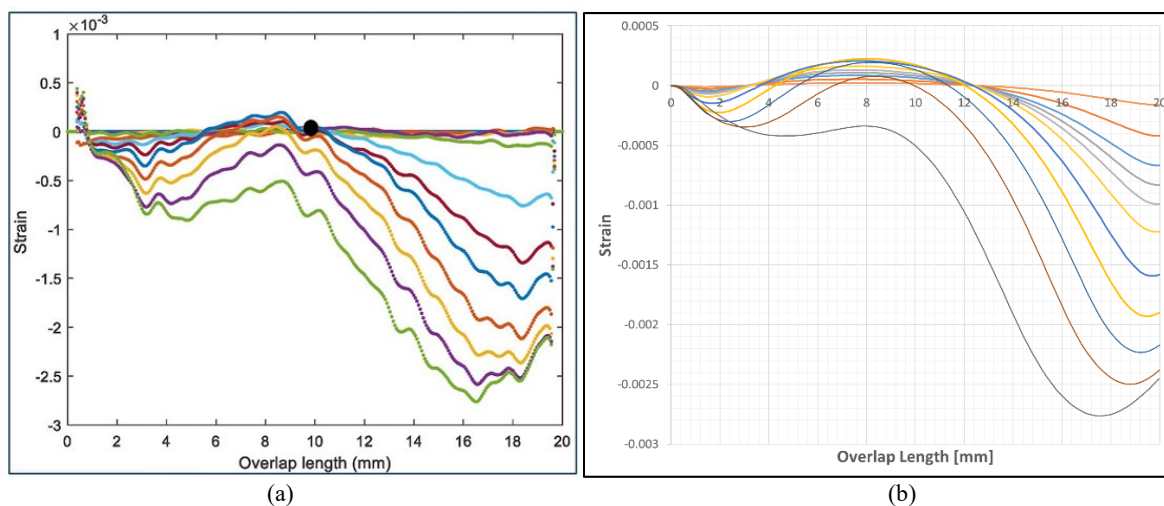


Figure 7.17: Strain Distribution on the Backface of Pu-L2W2T3 through Overlap Length under Different Loads for (a) Experimental [09] and (b) Numerical Results

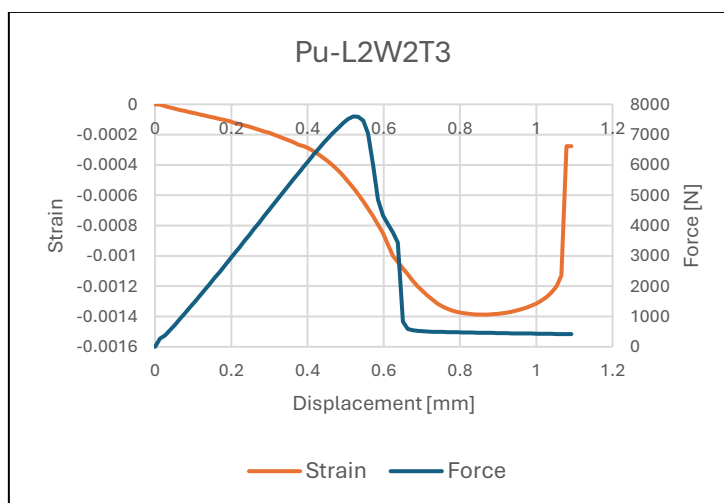


Figure 7.18: Strain-displacement and force-displacement curves for numerical result of Pu-L2W2T3

The 2D surface-based cohesive model with a bilinear traction-separation law was employed to describe the adhesive bonds of the Pu-L2W1T1 specimen. The adhesive had a length of 20 mm, a width of 10 mm, a thickness 1.1 mm, and the adherend had a thickness of 0.77 mm. This comparison was performed in order to assess Zero Strain Point detection as well as the strain behaviour under applied loads.

Figures 7.19(a) and (b) provided strain distribution around the entire overlap length of the adhesive joint from experimental and numerical results, respectively, which proved that the prediction of ZSP position is successful. The ZSP position calculated numerically agrees with the value found experimentally up to an acceptable relative error of $\sim 10\%$. (Table 7.5)

Numerical results show a maximum strain value of -1.7×10^{-3} , while experimental results yield value of -3.2×10^{-3} . The relative error corresponds to 46%, inferring inaccuracy in strain amplitude. Although the ZSP position is predicted well, when looking at the experimental data, it is seen that the ZSP position shifts to the left at high loads, while in the numerical analysis this behaviour first shifts to the right and then to the left. Therefore, the model has some limitations in accurately capturing non-linear adhesive behaviour.

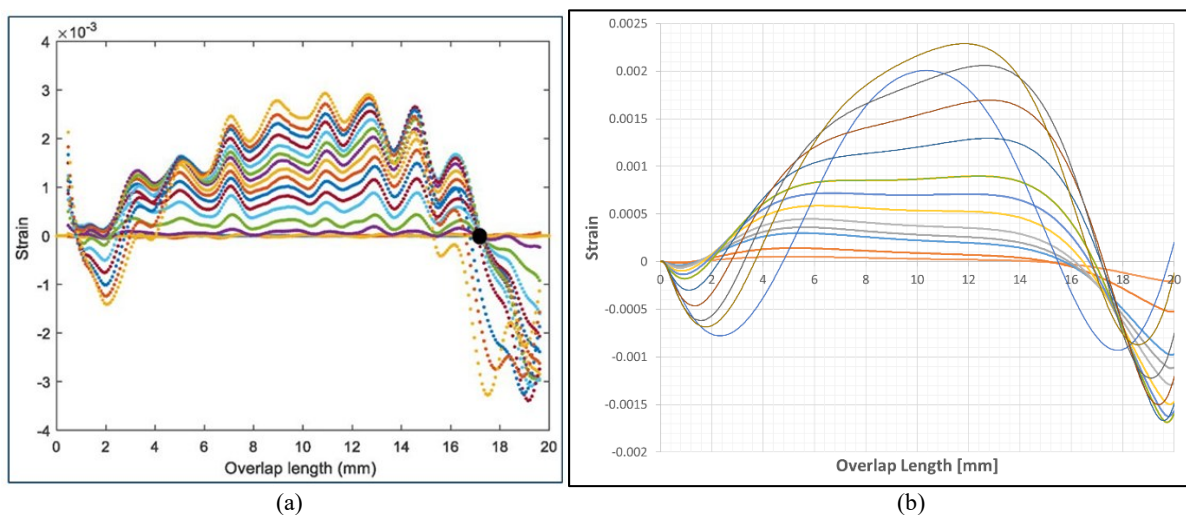


Figure 7.19: Strain Distribution on the Backface of Pu-L2W1T1 through Overlap Length under Different Loads for (a) Experimental [09] and (b) Numerical Results

In addition, when Figure 7.20 is examined, traces of this anomalous behaviour can be seen. Normally, the strain value should be linear and horizontal on the zero value until the peak load, but here it deviates from the zero value earlier.

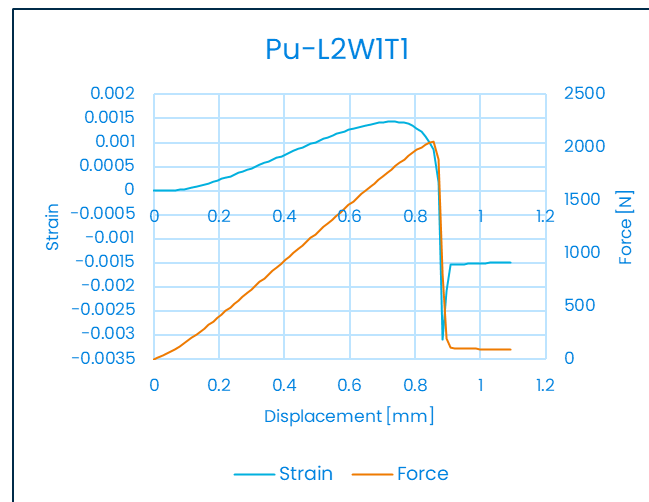


Figure 7.20: Strain-displacement and force-displacement curves for numerical result of Pu-L2W1T1

The 2D surface-based cohesive model with a bilinear traction-separation law was employed to describe the adhesive bonds of the Pu-L2W2T1 specimen. The adhesive had a length of 20 mm, a width of 20 mm, a thickness 1.1 mm, and the adherend had a thickness of 0.77 mm. This comparison was performed in order to assess Zero Strain Point detection as well as the strain behaviour under applied loads.

The strain distribution results from experimental (Figure 7.21a) and numerical (Figure 7.21b & Figure 7.22) analyses along the overlap length show successful prediction of ZSP. The numerically calculated ZSP position is in very good correspondence with an experimental value with a sufficiently low relative error of ~6%. (Table 7.5)

Comparing with the experimental results, the maximum strain value of the numerical calculation is also underestimated, which is -1.7×10^{-3} , while the experimental test is -3.5×10^{-3} . The corresponding relative error in strain amplitude is 50%. (Table 7.5) Although ZSP trend is accurately captured, the attenuation of strain response at high loads in the numerical model has limitations in accurately capturing any non-linear adhesive behaviour. (Figure 7.21b) The strain path in Figure 7.22 also confirms this behaviour.

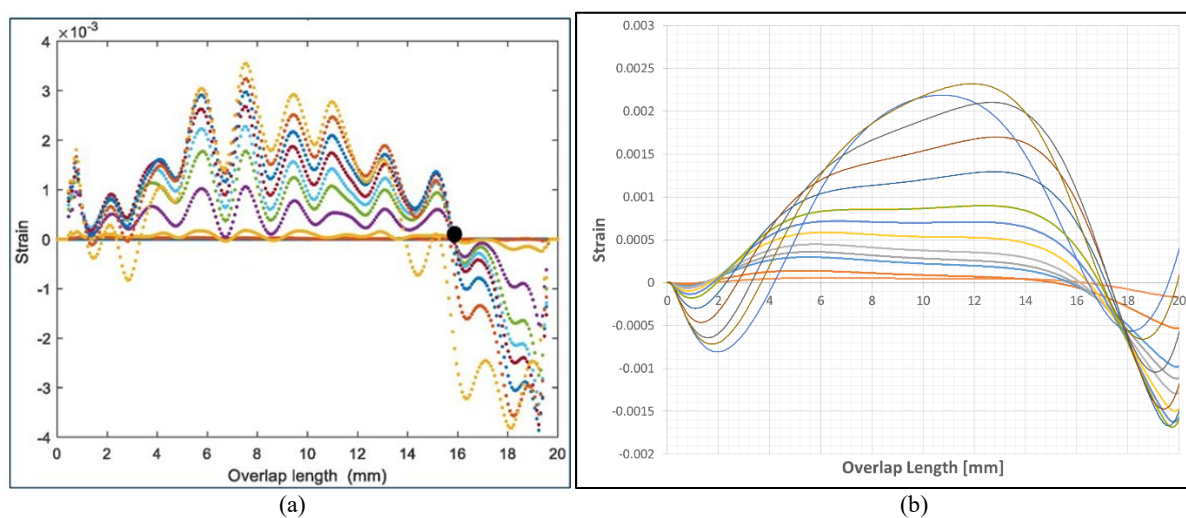


Figure 7.21: Strain Distribution on the Backface of Pu-L2W2T1 through Overlap Length under Different Loads for (a) Experimental [09] and (b) Numerical Results

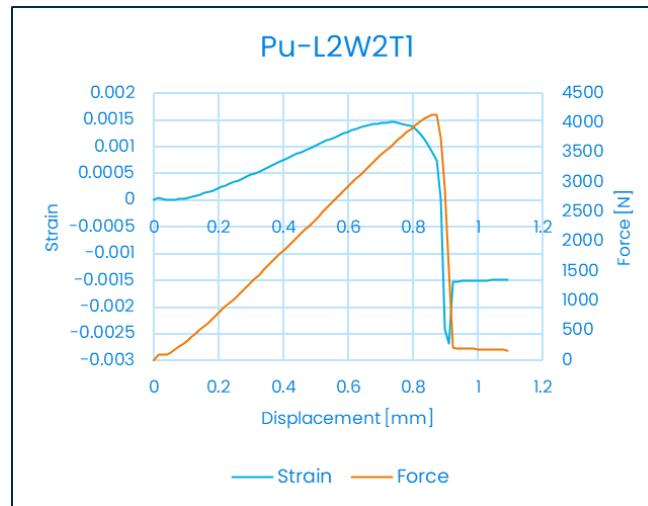


Figure 7.22: Strain-displacement and force-displacement curves for numerical result of Pu-L2W2T1

The 2D surface-based cohesive model with a bilinear traction-separation law was employed to describe the adhesive bonds of the Pu-L2W3T1 specimen. The adhesive had a length of 20 mm, a width of 30 mm, a thickness 1.1 mm, and the adherend had a thickness of 0.77 mm. This comparison was performed in order to assess Zero Strain Point detection as well as the strain behaviour under applied loads.

Both experimental (Figure 7.23a) and numerical (Figure 7.23b & Figure 7.24) analyses on the strain distribution along the overlap length are presented for successful prediction of both ZSP. The numerically obtained ZSP position is very close to the value observed experimentally, ~11% relative error. (Table 7.5)

The maximum value of strain reached is underestimated in the numerical analysis at -1.7×10^{-3} while the experimental value is -3.9×10^{-3} . The relative error, in this case, is 56% giving rise to some amplitude discrepancies in strain. Although the ZSP position is predicted well, when looking at the experimental data, it is seen that the ZSP position shifts to the left at high loads, while in the numerical analysis this behaviour first shifts to the right and then to

the left. Therefore, the model has some limitations in accurately capturing non-linear adhesive behaviour. The strain path in Figure 7.24 also confirms this behaviour.

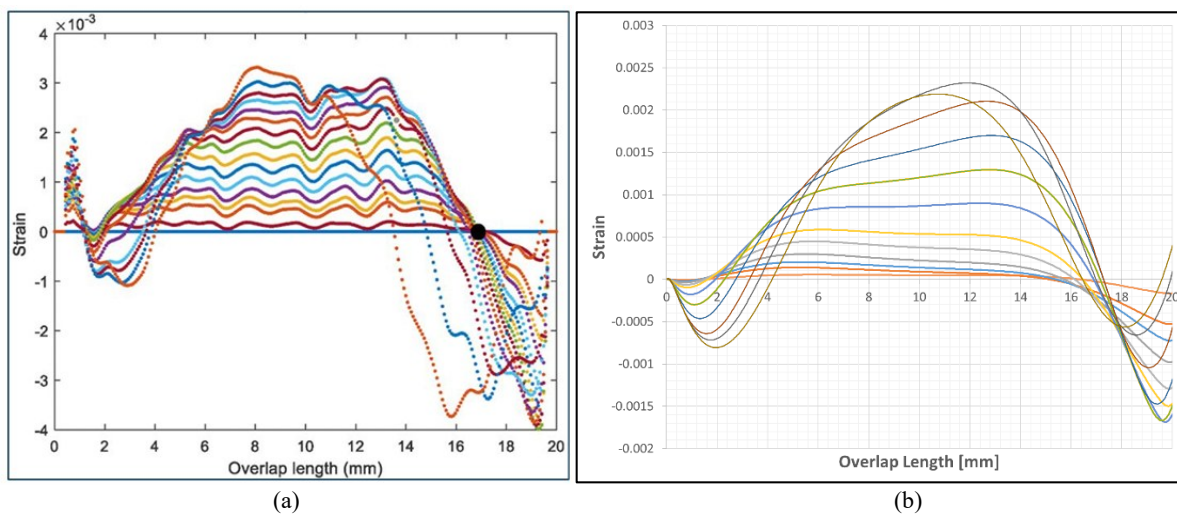


Figure 7.23: Strain Distribution on the Backface of Pu-L2W3T1 through Overlap Length under Different Loads for (a) Experimental [09] and (b) Numerical Results

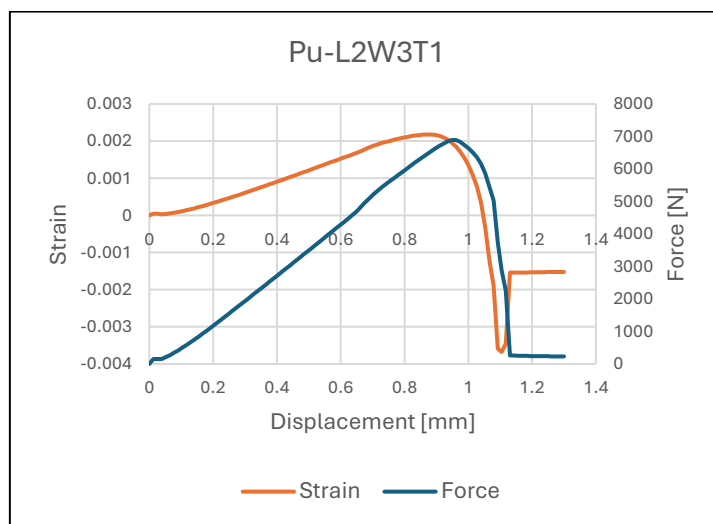


Figure 7.24: Strain-displacement and force-displacement curves for numerical result of Pu-L2W3T1

The 2D surface-based cohesive model with a bilinear traction-separation law was employed to describe the adhesive bonds of the Ep-L1W1T1 specimen. The adhesive had a

length of 10 mm, a width of 10 mm, a thickness 0.35 mm, and the adherend had a thickness of 1.76 mm. This comparison was performed in order to assess Zero Strain Point detection as well as the strain behaviour under applied loads.

The ZSP prediction is also evidenced by the strain distribution along the same overlap length from the experimental (Figure 7.25a) and the numerical (Figure 7.25b & Figure 7.26) analyses. The predicted ZSP position is in good agreement with the observed ZSP position, with a relative error of $\sim 16\%$. (Table 7.5)

The maximum strain value is slightly overestimated in the numerical analysis: -3.2×10^{-3} versus the experimental value of -3×10^{-3} . The relative error corresponding to it is 6%, which suggests a slight shift in strain amplitude. (Table 7.5) The model accurately captures ZSP trends and reflects strain behaviour.

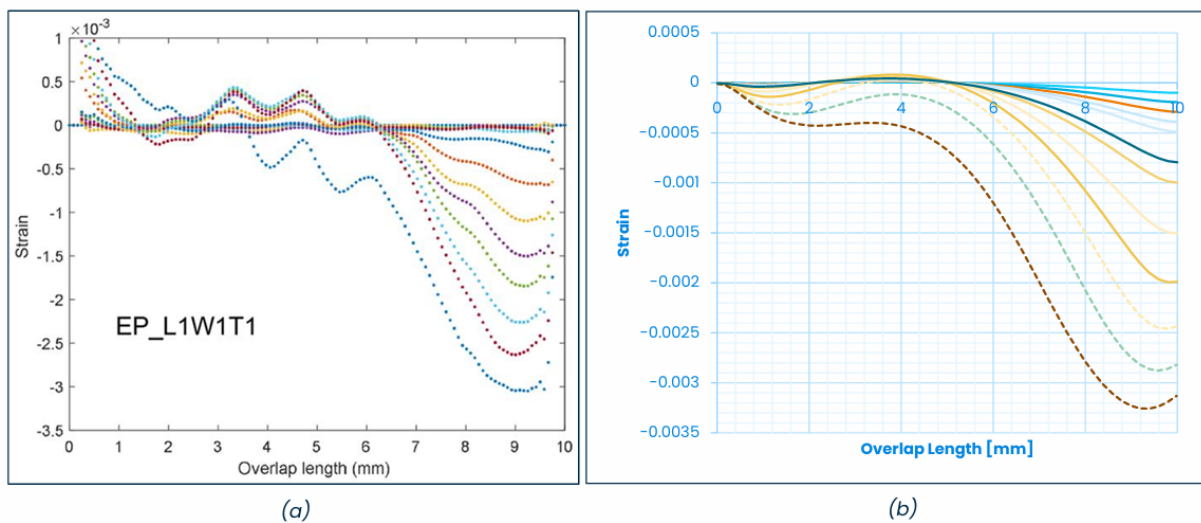


Figure 7.25: Strain Distribution on the Backface of Ep-L1W1T1 through Overlap Length under Different Loads for (a) Experimental [06] and (b) Numerical Results

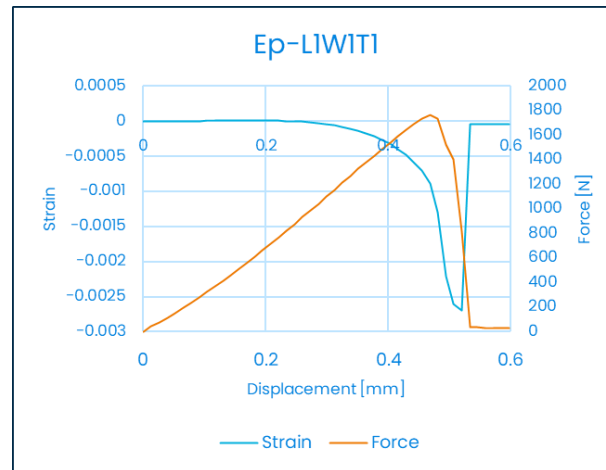


Figure 7.26: Strain-displacement and force-displacement curves for numerical result of Ep-L1W1T1

The 2D surface-based cohesive model with a bilinear traction-separation law was employed to describe the adhesive bonds of the Ep-L1W2T1 specimen. The adhesive had a length of 10 mm, a width of 20 mm, a thickness 0.35 mm, and the adherend had a thickness of 1.76 mm. This comparison was performed in order to assess Zero Strain Point detection as well as the strain behaviour under applied loads.

Successful ZSP prediction has been confirmed in terms of the strain distribution across the overlap length in both experimental (Figure 7.27a) and numerical (Figure 7.27b & Figure 7.28) analyses. The position of the ZSP obtained numerically agrees with the experimental value with relative error of $\sim 16\%$. (Table 7.5)

The maximum value of the strain predicted by the numerical analysis is slightly higher than the experimental value which is -3×10^{-3} . The relative error is 6%, showing that the error in determining strain amplitude is small. Clearly, the model presented accurately describes ZSP trends explaining strain behaviour (Table 7.5).

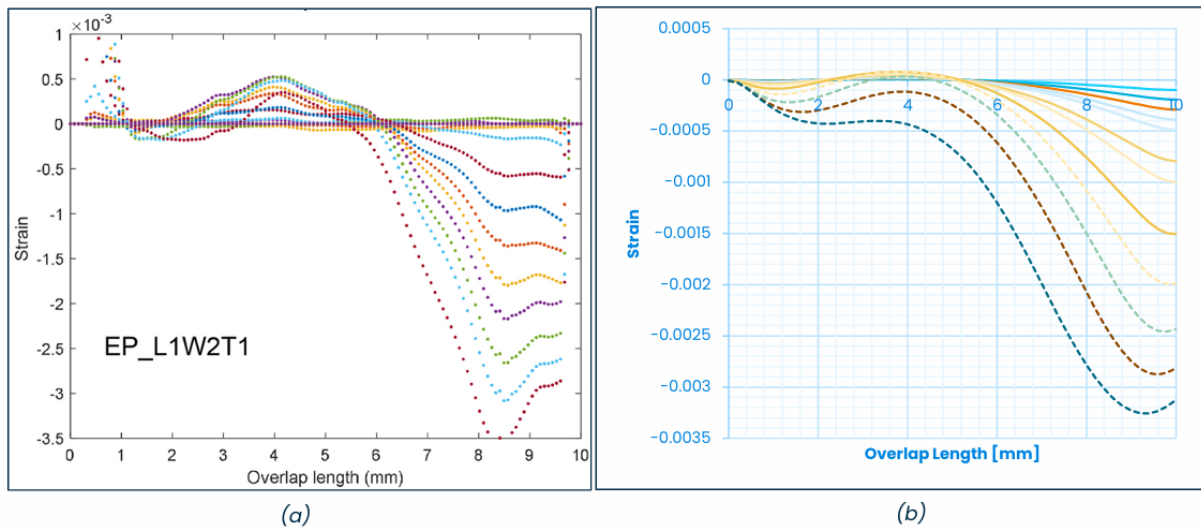


Figure 7.27: Strain Distribution on the Backface of Ep-L1W2T1 through Overlap Length under Different Loads for (a) Experimental [06] and (b) Numerical Results

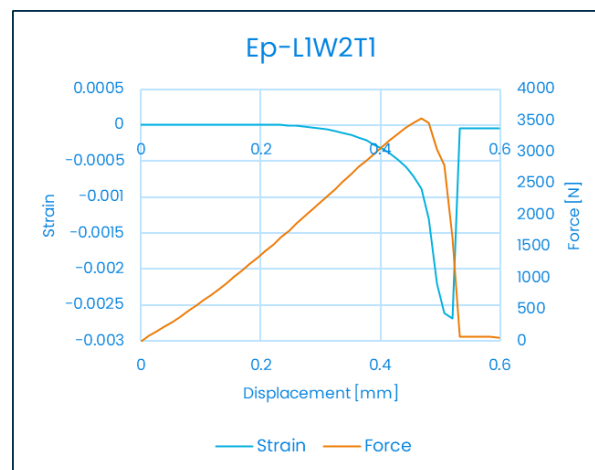


Figure 7.28: Strain-displacement and force-displacement curves for numerical result of Ep-L1W2T1

The 2D surface-based cohesive model with a bilinear traction-separation law was employed to describe the adhesive bonds of the Ep-L1W3T1 specimen. The adhesive had a length of 10 mm, a width of 30 mm, a thickness 0.35 mm, and the adherend had a thickness of 1.76 mm. This comparison was performed in order to assess Zero Strain Point detection as well as the strain behaviour under applied loads.

The ZSP was predicted accurately for the Ep-L1W3T1 specimen (Figure 7.29 & Figure 7.30). The numerically obtained ZSP position closely agrees with the value found experimentally with a relative error of $\sim 16\%$. (Table 7.5)

The maximum strain obtained from the numerical analysis is slightly higher than the experimental value (-3.2×10^{-3} against -3×10^{-3}). The relative error is 6%, which is a small difference in strain amplitude. (Table 7.5) It accurately reflects strain behaviour and captures the observed ZSP trends.

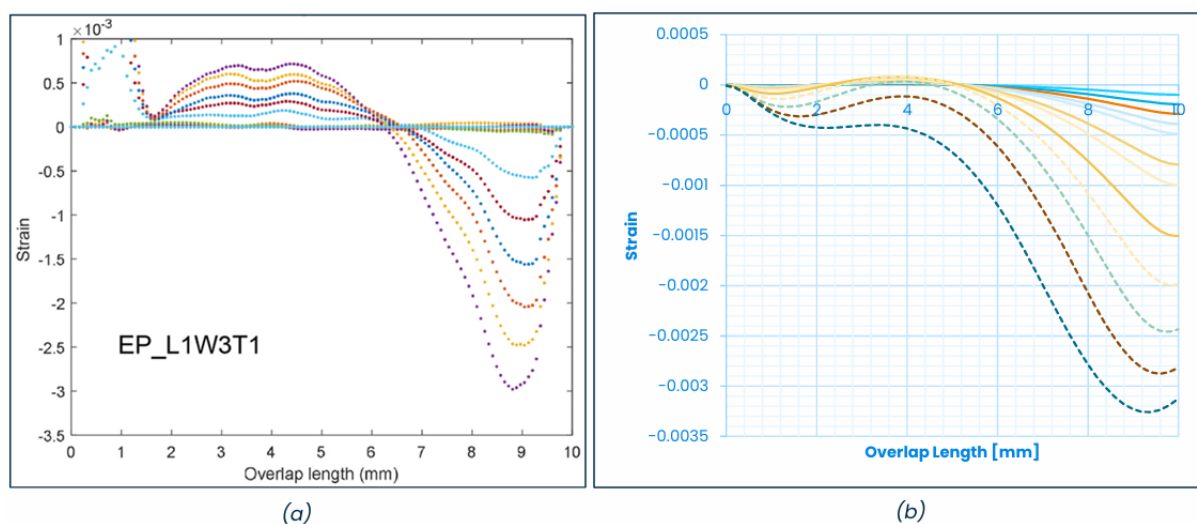


Figure 7.29: Strain Distribution on the Backface of Ep-L1W3T1 through Overlap Length under Different Loads for (a) Experimental [06] and (b) Numerical Results

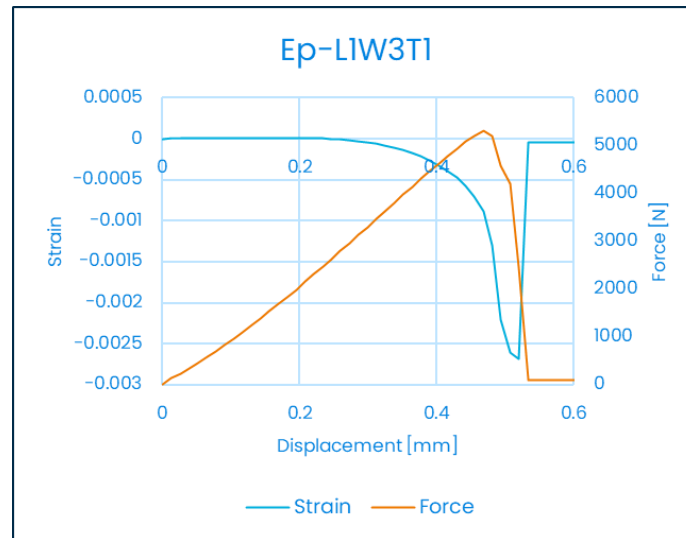


Figure 7.30: Strain-displacement and force-displacement curves for numerical result of Ep-L1W3T1

The 2D surface-based cohesive model with a bilinear traction-separation law was employed to describe the adhesive bonds of the Ep-L2W1T1 specimen. The adhesive had a length of 20 mm, a width of 10 mm, a thickness 0.35 mm, and the adherend had a thickness of 1.76 mm. This comparison was performed in order to assess Zero Strain Point detection as well as the strain behaviour under applied loads.

The distribution of strain on the overlap length from experimental tests (Figure 7.31a) and numerical models (Figure 7.31b & Figure 7.32) indicates significant agreement in the prediction of the position of the ZSP. The numerically ZSP position is nearly equal to the experimental value, and a relative error of $\sim 1\%$ is realized. (Table 7.5)

-2.1×10^{-3} is obtained for both cases in close agreement between numerical analysis and experimental maximum strain values. The corresponding relative error is 0%, demonstrating great agreement. This means that the model predicts both ZSP trends and strain amplitudes with good accuracy (Table 7.5), confirming its capability to adequately model the behaviour of epoxy adhesive for this specimen.

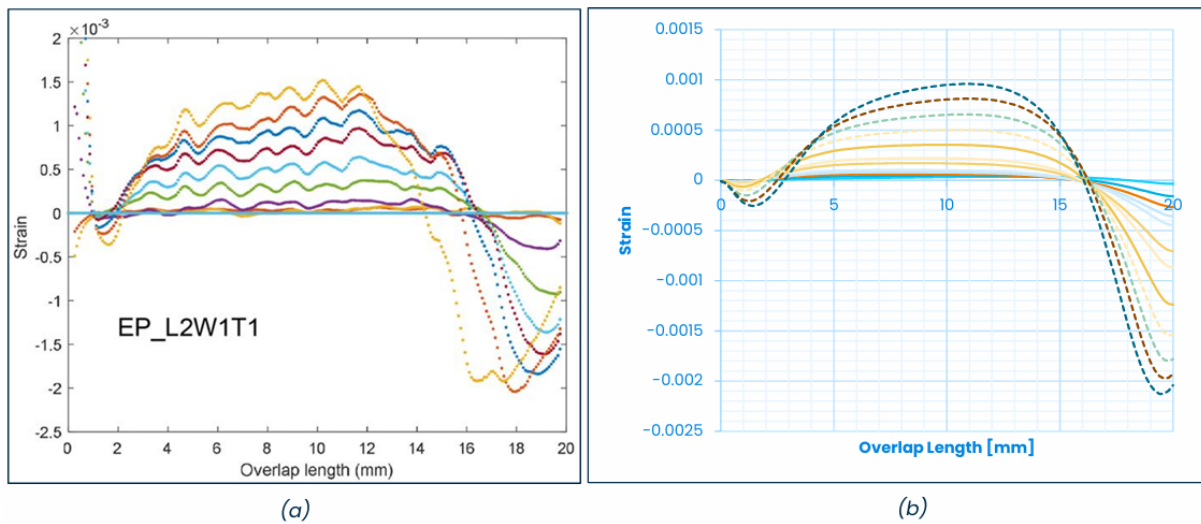


Figure 7.31: Strain Distribution on the Backface of Ep-L2W1T1 through Overlap Length under Different Loads for (a) Experimental [06] and (b) Numerical Results

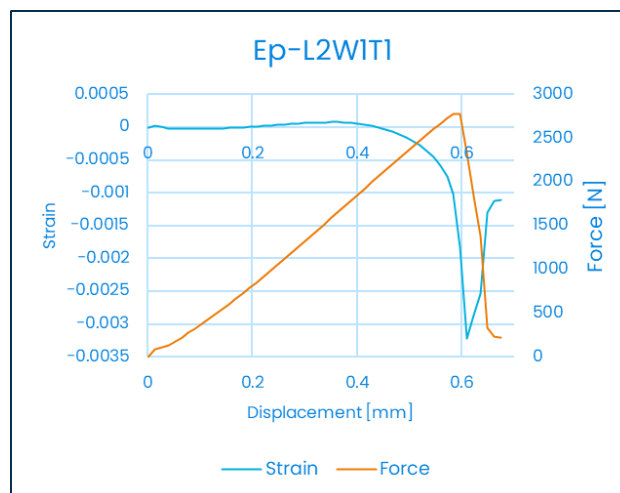


Figure 7.32: Strain-displacement and force-displacement curves for numerical result of Ep-L2W1T1

The 2D surface-based cohesive model with a bilinear traction-separation law was employed to describe the adhesive bonds of the Ep-L2W2T1 specimen. The adhesive had a length of 20 mm, a width of 20 mm, a thickness 0.35 mm, and the adherend had a thickness

of 1.76 mm. This comparison was performed in order to assess Zero Strain Point detection as well as the strain behaviour under applied loads.

Both experimental (Figure 7.33a) and numerical analysis (Figure 7.33b & Figure 7.34) of the strain distribution along the overlap length shows a remarkably good prediction of the ZSP position. Numerically, the ZSP position is nearly identical to the experimental value with a relative error of $\sim 1\%$. (Table 7.5)

The discrepancy between numerical analysis and the experimental value of strain has a perfect agreement with -2.1×10^{-3} for both cases. The relative error is 0%, demonstrating that the agreement between the two curves is rather good. (Table 7.5)

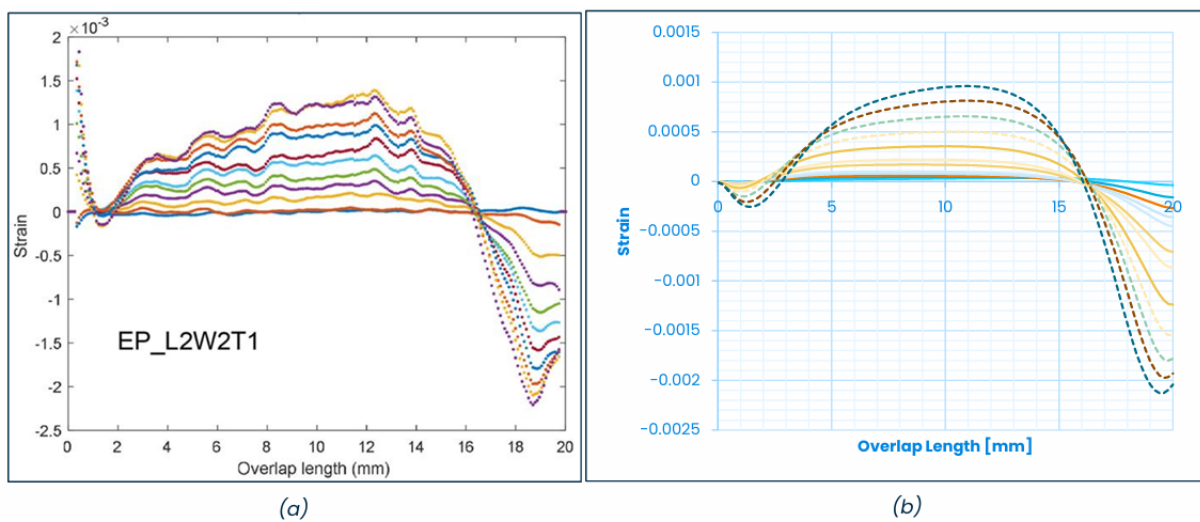


Figure 7.33: Strain Distribution on the Backface of Ep-L2W2T1 through Overlap Length under Different Loads for (a) Experimental [06] and (b) Numerical Results

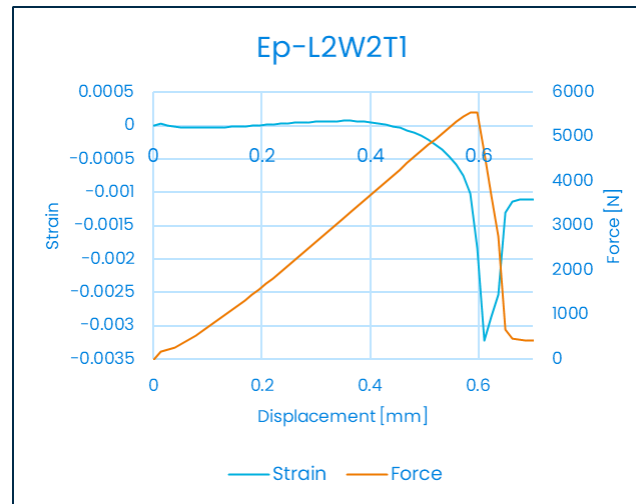


Figure 7.34: Strain-displacement and force-displacement curves for numerical result of Ep-L2W2T1

The 2D surface-based cohesive model with a bilinear traction-separation law was employed to describe the adhesive bonds of the Ep-L2W3T1 specimen. The adhesive had a length of 20 mm, a width of 30 mm, a thickness 0.35 mm, and the adherend had a thickness of 1.76 mm. This comparison was performed in order to assess Zero Strain Point detection as well as the strain behaviour under applied loads.

The strain distribution across the overlap length for both experimental (Fig. 7.35a) and numerical (Fig. 7.35b & Fig. 7.36) analyses shows very close prediction of the ZSP position. The numerically obtained ZSP position is very close to the experimental one, with ~1% of relative error. (Table 7.5)

These values match perfectly with the experimental ones for strain in the numerical analysis, which is -2.1×10^{-3} , consecutively. The relative error is 0% which corresponds to excellent agreement. This outcome illustrates the model's ability to consistently reflect ZSP trends and the corresponding strain amplitudes for various configurations (Table 7.5).

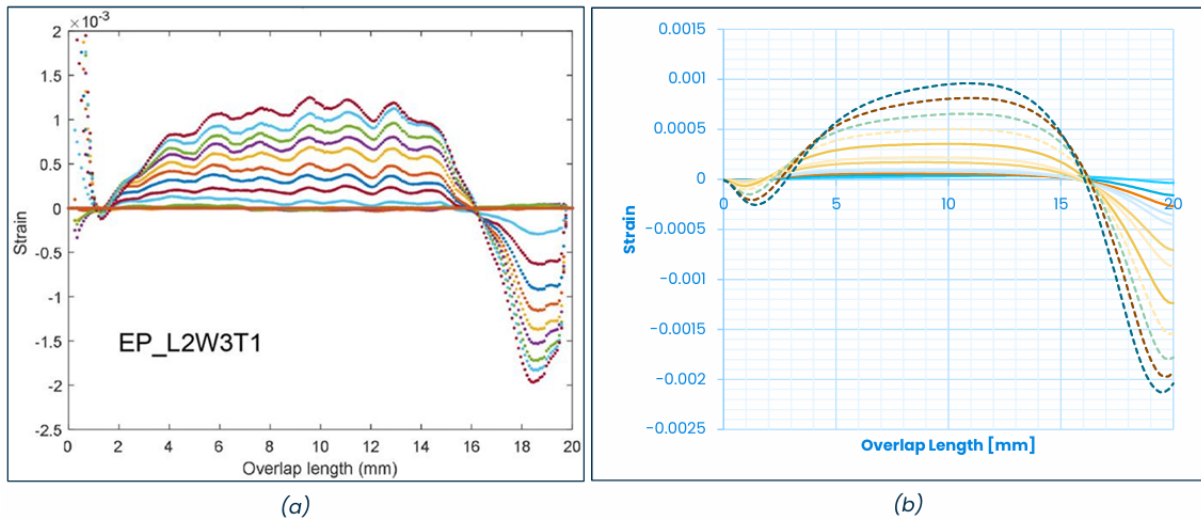


Figure 7.35: Strain Distribution on the Backface of Ep-L2W3T1 through Overlap Length under Different Loads for (a) Experimental [06] and (b) Numerical Results

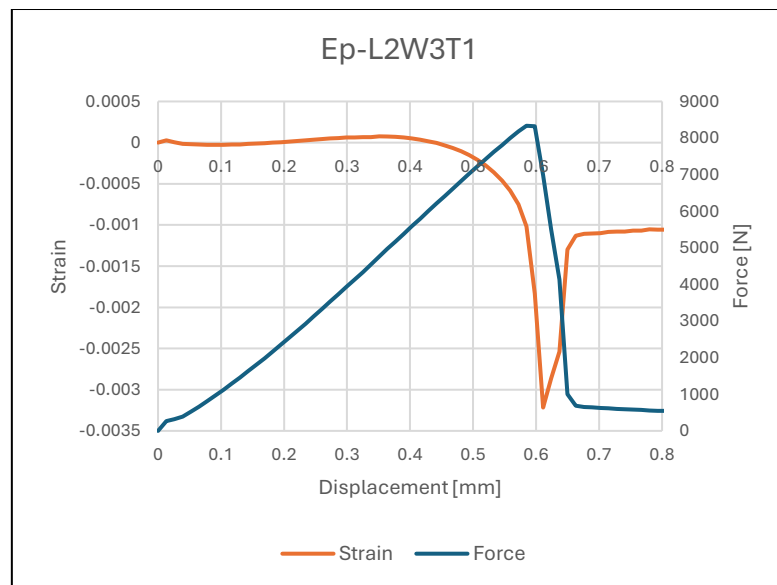


Figure 7.36: Strain-displacement and force-displacement curves for numerical result of Ep-L2W3T1

The 2D surface-based cohesive model with a bilinear traction-separation law was employed to describe the adhesive bonds of the Ep-L2W1T2 specimen. The adhesive had a

length of 20 mm, a width of 10 mm, a thickness 0.35 mm, and the adherend had a thickness of 3.52 mm. This comparison was performed in order to assess Zero Strain Point detection as well as the strain behaviour under applied loads.

Both experimental (Figure 7.37a) and numerical (Figure 7.37b & Figure 7.38) analyses confirm the validity of the ZSP prediction in the strain distribution along the overlap length. The ZSP value numerically obtained is quite close to the experimental value, with ~4% relative error. (Table 7.5)

The maximum strain value obtained via numerical analysis is slightly higher than the experimental value which is -2.5×10^{-3} compared with the experimental value of -2.2×10^{-3} . The relative error is 13%, meaning the strain prediction is reasonably accounted. (Table 7.5)

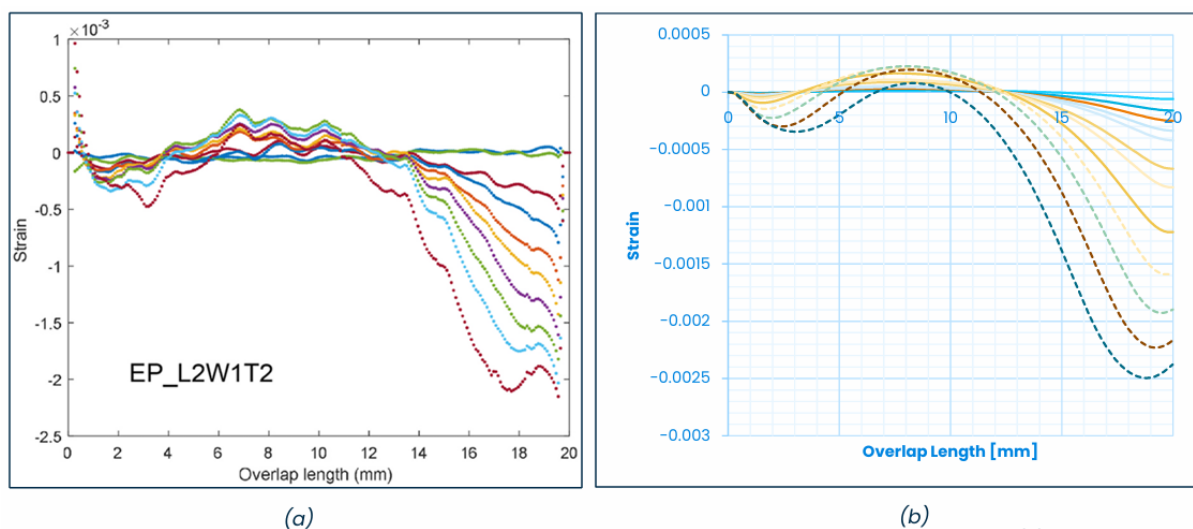


Figure 7.37: Strain Distribution on the Backface of Ep-L2W1T2 through Overlap Length under Different Loads for (a) Experimental [06] and (b) Numerical Results

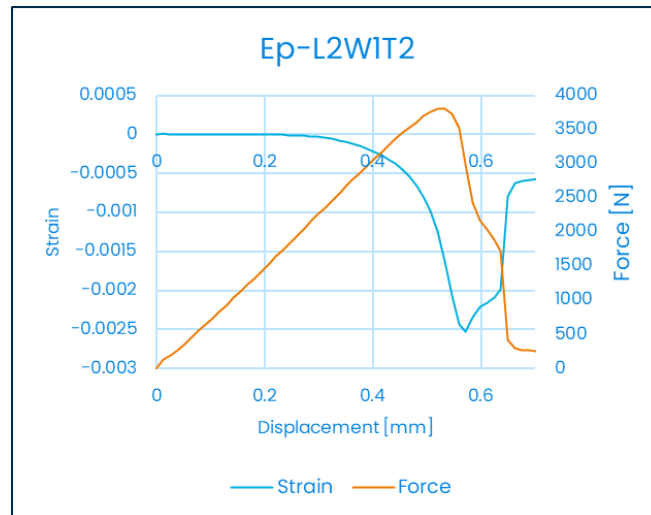


Figure 7.38: Strain-displacement and force-displacement curves for numerical result of Ep-L2W1T2

The 2D surface-based cohesive model with a bilinear traction-separation law was employed to describe the adhesive bonds of the Ep-L2W2T2 specimen. The adhesive had a length of 20 mm, a width of 20 mm, a thickness 0.35 mm, and the adherend had a thickness of 3.52 mm. This comparison was performed in order to assess Zero Strain Point detection as well as the strain behaviour under applied loads.

Figure 7.39b & Figure 7.40 shows that prediction of the ZSP position is very closely assigned to the ZSP position from the experimental value (Figure 7.39a). The numerically obtained ZSP position is close to the experimental value with a relative error of ~4% (Table 7.5).

The maximum strain value predicted by numerical analysis is slightly higher than the experimental data, which is -2.4×10^{-3} . The relative error is 4%. (Table 7.5)

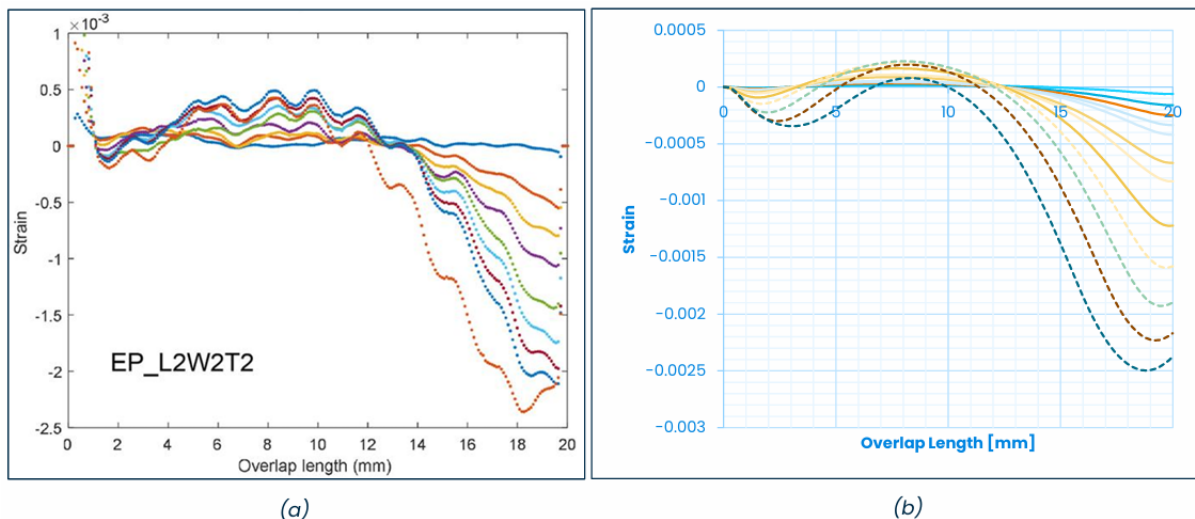


Figure 7.39: Strain Distribution on the Backface of Ep-L2W2T2 through Overlap Length under Different Loads for (a) Experimental [06] and (b) Numerical Results



Figure 7.40: Strain-displacement and force-displacement curves for numerical result of Ep-L2W2T2

The 2D surface-based cohesive model with a bilinear traction-separation law was employed to describe the adhesive bonds of the Ep-L2W3T2 specimen. The adhesive had a length of 20 mm, a width of 30 mm, a thickness 0.35 mm, and the adherend had a thickness

of 3.52 mm. This comparison was performed in order to assess Zero Strain Point detection as well as the strain behaviour under applied loads.

The strain distribution along the overlap length is predicted accurately to detect the ZSP position. (Figure 7.41a, Figure 7.41b and Figure 7.42) The numerically computed ZSP position closely matches the experimental value, having a relative error of $\sim 8\%$ (Table 7.5).

Numerical analysis accurately matches the maximum value of strain, which is -2.5×10^{-3} equivalent to the value derived by the experiment. (Table 7.5) This confirms excellent agreement and the model's ability to reproduce the mechanical behaviour of the adhesive.

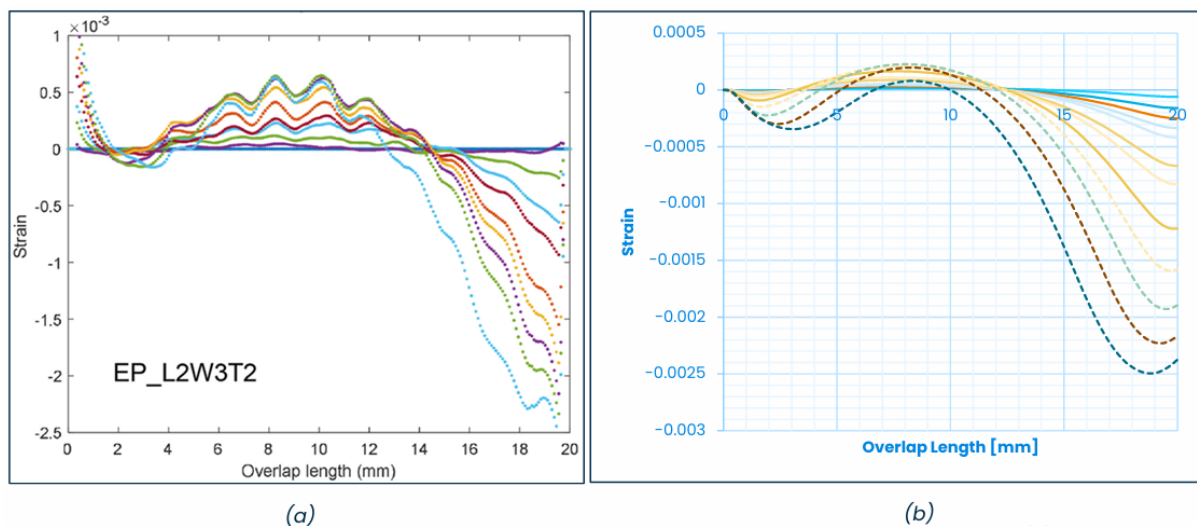


Figure 7.41: Strain Distribution on the Backface of Ep-L2W3T2 through Overlap Length under Different Loads for (a) Experimental [06] and (b) Numerical Results

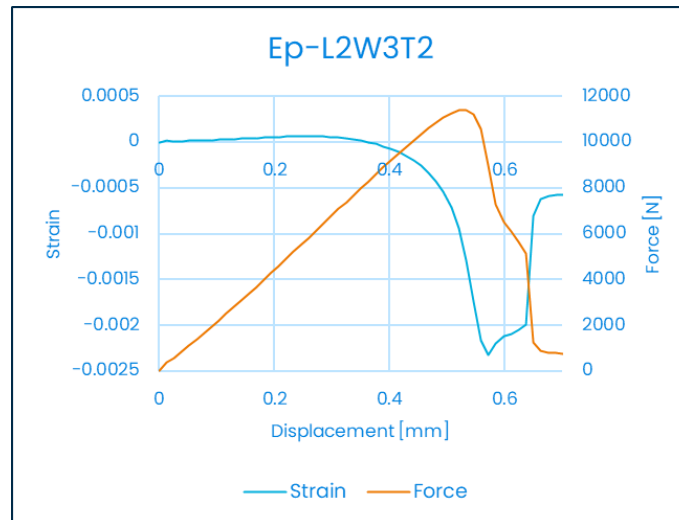


Figure 7.42: Strain-displacement and force-displacement curves for numerical result of Ep-L2W3T2

The 2D surface-based cohesive model with a bilinear traction-separation law was employed to describe the adhesive bonds of the Ep-L1W1T2 specimen. The adhesive had a length of 10 mm, a width of 10 mm, a thickness 0.35 mm, and the adherend had a thickness of 3.52 mm. This comparison was performed in order to assess Zero Strain Point detection as well as the strain behaviour under applied loads.

Figure 7.43a and Figure 7.43b show the strain distribution along the overlap length from experimental and numerical analyses, respectively. They both present difficulties in accurately determining the ZSP location. From the current results, a reliable ZSP position could not be obtained.

In spite of this, reasonable prediction of the maximum strain value is obtained by the numerical analysis. The relative error is 12 % with respect to the experimental maximum strain, which is -2.5×10^{-3} . This shows that the numerical model makes reasonably accurate prediction.

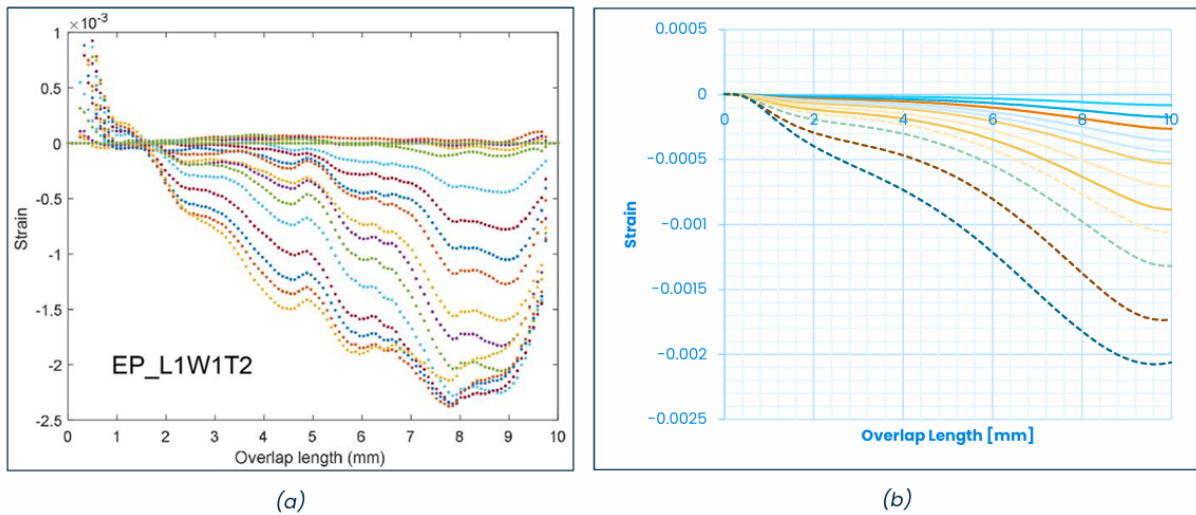


Figure 7.43: Strain Distribution on the Backface of Ep-L1W1T2 through Overlap Length under Different Loads for (a) Experimental [06] and (b) Numerical Results

The 2D surface-based cohesive model with a bilinear traction-separation law was employed to describe the adhesive bonds of the Ep-L1W2T2 specimen. The adhesive had a length of 10 mm, a width of 20 mm, a thickness 0.35 mm, and the adherend had a thickness of 3.52 mm. This comparison was performed in order to assess Zero Strain Point detection as well as the strain behaviour under applied loads.

Indeed, the strain distribution along the overlap length obtained from both experimental (Figure 7.44a) and numerical (Figure 7.44b) analyses does not allow for a precise identification of the ZSP location.

The maximum strain value is -2.1×10^{-3} of numerical analysis, while -2.5×10^{-3} represents the experimental value. The relative error is 12%, indicating discrepancies in amplitude of strain. The results are generally satisfactory for strain values, although the lack of ZSP data suggests that strain capture requires more attention with respect to conditions.

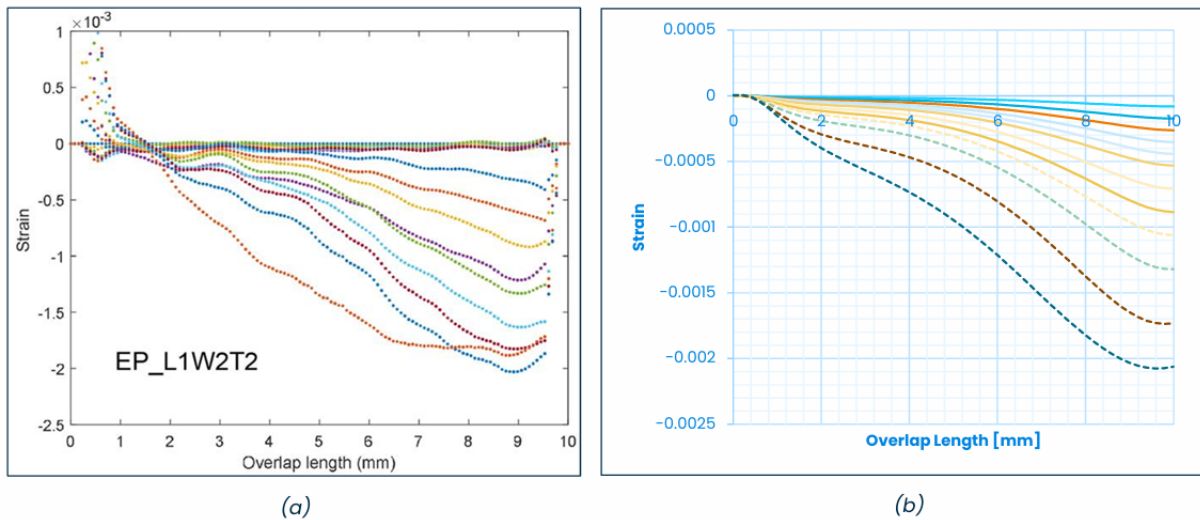


Figure 7.44: Strain Distribution on the Backface of Ep-L1W2T2 through Overlap Length under Different Loads for (a) Experimental [06] and (b) Numerical Results

The 2D surface-based cohesive model with a bilinear traction-separation law was employed to describe the adhesive bonds of the Ep-L1W3T2 specimen. The adhesive had a length of 10 mm, a width of 30 mm, a thickness 0.35 mm, and the adherend had a thickness of 3.52 mm. This comparison was performed in order to assess Zero Strain Point detection as well as the strain behaviour under applied loads.

Both experimental (Figure 7.45a) and numerical (Figure 7.45b) strain distribution along the overlap length through strains suggest the difficulties of using ZSP location in practice. The current comparison resulted in no ZSP data being reported.

In both the experimental and the numerical cases, the maximum strain is obtained as -2×10^{-3} . It means that the agreement between theoretical and experimental strain amplitude is very good.

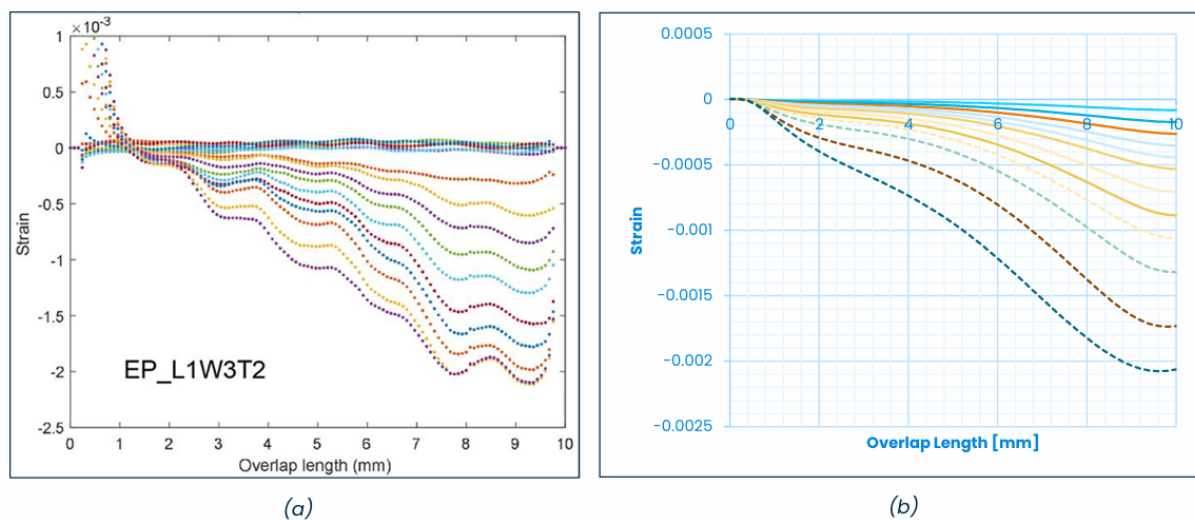


Figure 7.45: Strain Distribution on the Backface of Ep-L1W3T2 through Overlap Length under Different Loads for (a) Experimental [06] and (b) Numerical Results

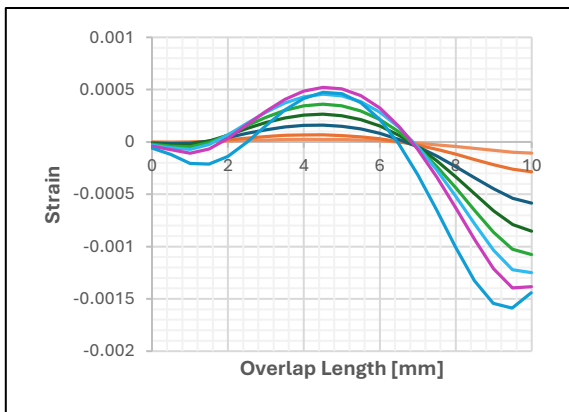
Specimen	ZSP Position (mm) Experimental	ZSP Position (mm) Numerical	ZSP Relative Error (%)	Max Strain Experimental ($\times 10^{-3}$)	Max Strain Numerical ($\times 10^{-3}$)	Max Strain Relative Error (%)
Pu-L1W1T1	7÷8	6÷7	~10	-5	-2.7	46
Pu-L1W2T1	7÷8	6÷7	~10	-7	-2.7	61
Pu-L1W2T2	5÷6	5	~10	-3	-2.7	10
Pu-L1W2T3	3÷4	-	-	-2	-1.6	17
Pu-L1W3T1	7	6÷7	0÷16	-7	-2.5	65
Pu-L2W2T3	9÷10	12	-	-2.6	-2.1	19
Pu-L2W1T1	17÷18	15÷16	~10	-3.2	-1.7	46
Pu-L2W2T1	16	15	~6	-3.5	-1.7	50
Pu-L2W3T1	17	15	~11	-3.9	-1.7	56
Pu-L2W2T2	15	14	7	-4	-2	50
Ep-L1W1T1	6	5	~16	-3	-3.2	6
Ep-L1W2T1	6.2	5.2	~16	-3	-3.2	6
Ep-L1W3T1	6.2	5.2	~16	-3	-3.2	6

Ep-L2W1T1	16÷17	16.2	~1	-2.1	-2.1	0
Ep-L2W2T1	16÷17	16.2	~1	-2.1	-2.1	0
Ep-L2W3T1	16÷17	16.2	~1	-2.1	-2.1	0
Ep-L2W1T2	13	12.4	~4	-2.2	-2.5	4
Ep-L2W2T2	13	12.4	~4	-2.4	-2.5	4
Ep-L2W3T2	14	12.8	~8	-2.5	-2.5	0
Ep-L1W1T2	-	-	-	-2.5	-2.1	12
Ep-L1W2T2	-	-	-	-2.5	-2.1	12
Ep-L1W3T2	-	-	-	-2	-2	0

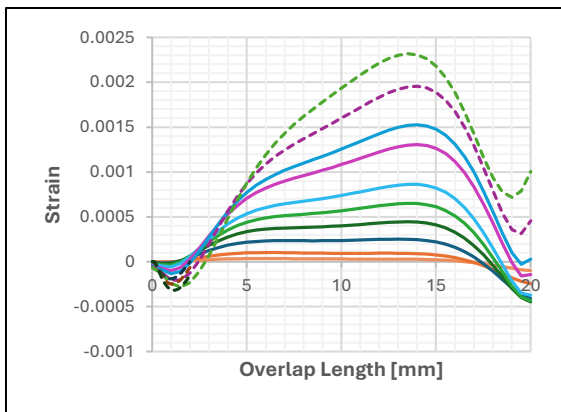
Table 7.5: Relative Error for ZSP Position and Max. Strain for All Specimens

7.4.2. The Results for 3D Surface-Based Cohesive Approach

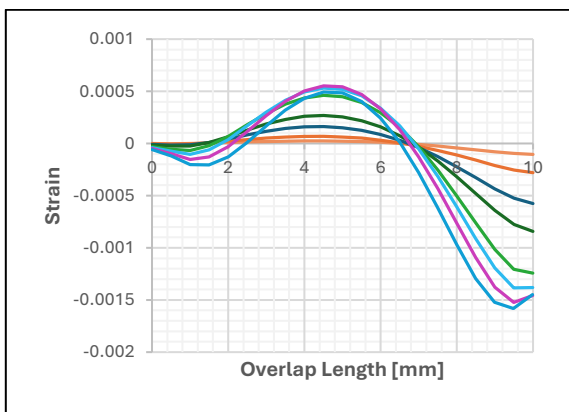
The strain distribution and ZSP location through the entire overlap length across all the PU specimens using the 3D surface-based cohesive method are displayed in Figure 7.45. Overall, all configurations yield reasonable ZSP positions and strain distributions that align with experimental data. However, the deviation of ZSP behaviour is bigger in the Pu-L2WT1 configuration, as the ZSP position moves toward the positive rather than the negative region that is expected. Such discrepancy, which was also found in the 2D surface-based cohesive model, shows the influence of modelling assumptions and boundary conditions on this configuration.



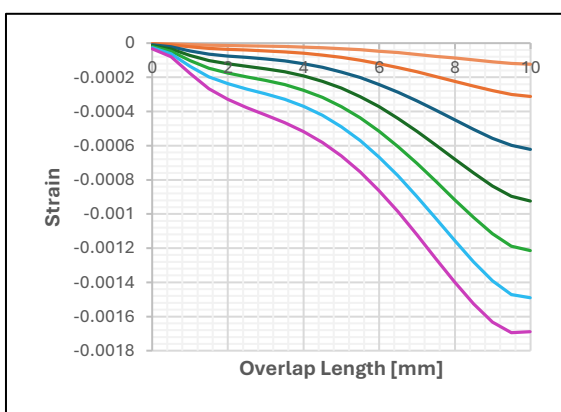
(a)



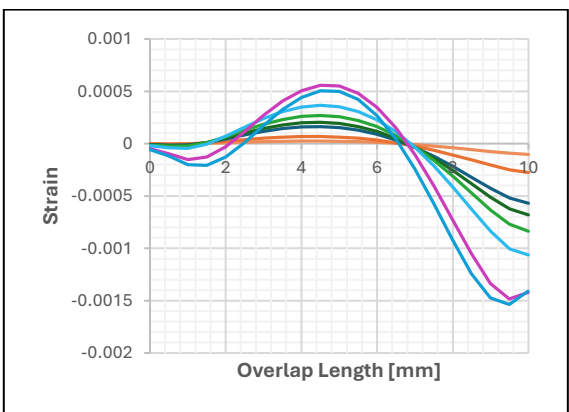
(b)



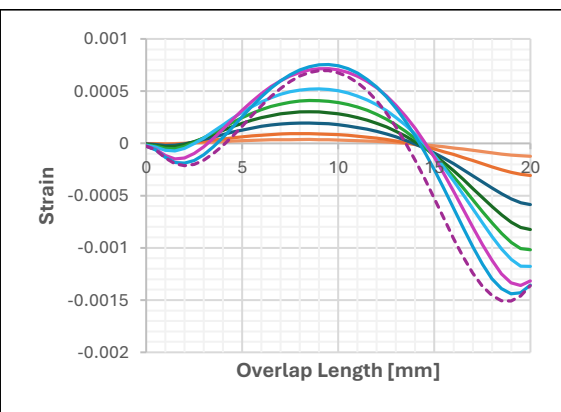
(c)



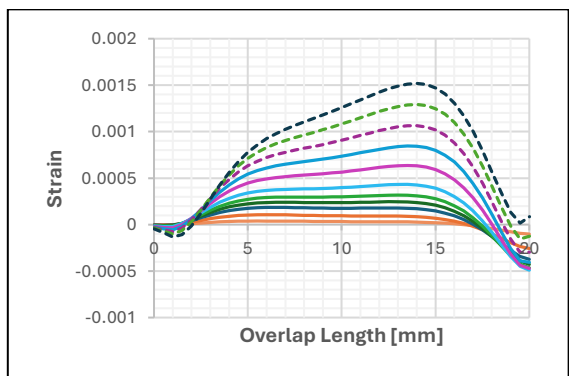
(d)



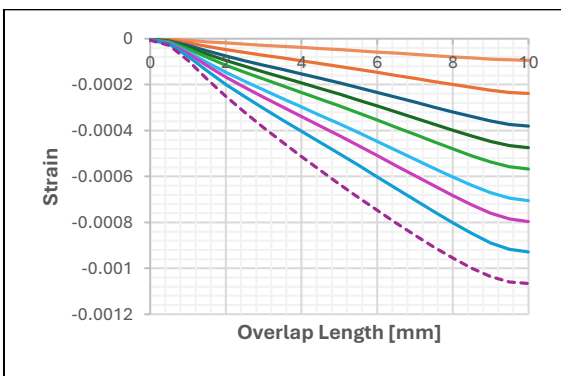
(e)



(f)



(g)



(h)

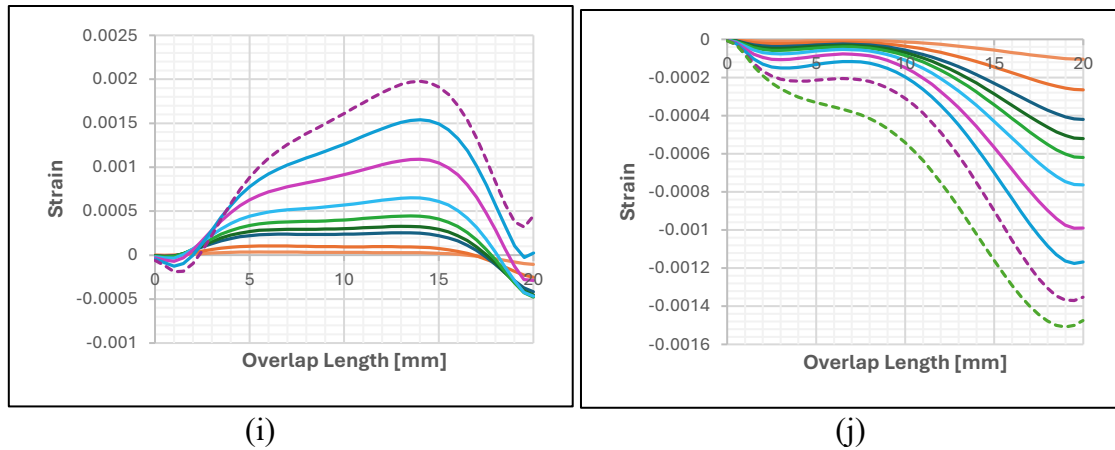
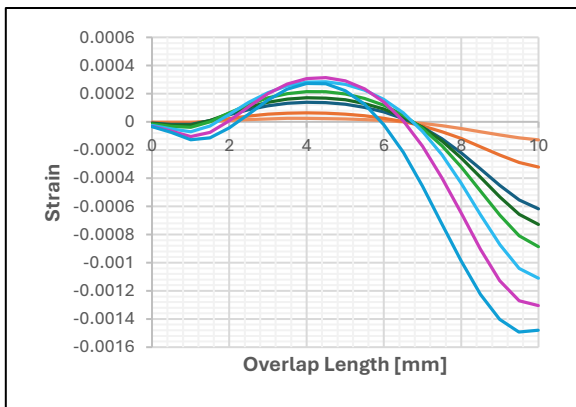
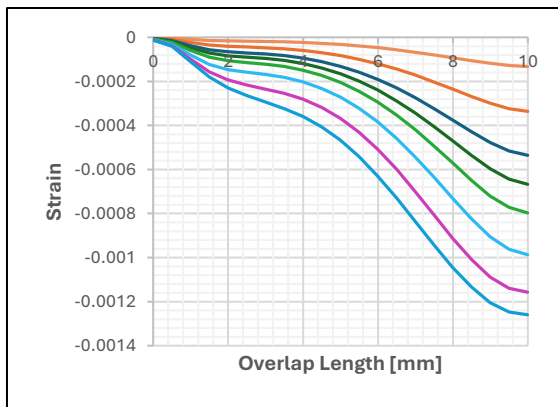


Figure 7.45: Strain Distribution and Zero Strain Point (ZSP) Locations Across Overlap Length for Various PU Specimens Using 3D Surface-Based Cohesive Approach: (a) Pu-L1W1T1, (b) Pu-L2W3T1, (c) Pu-L1W2T1, (d) Pu-L1W2T2, (e) Pu-L1W3T1, (f) Pu-L2W2T2, (g) Pu-L2W1T1, (h) Pu-L1W2T3, (i) Pu-L2W2T1, (j) Pu-L2W2T3

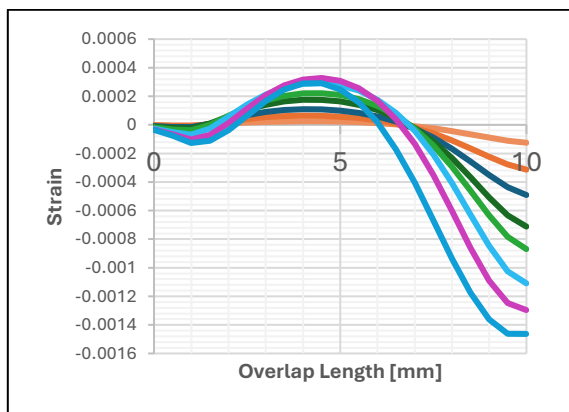
Figure 7.46 shows strain profiles and ZSP locations for different EP specimens at the overlap length based on a 3D surface-based cohesive model. The EP configurations exhibit a more constant and predictable ZSP behaviour with respect to the PU specimens. This observation suggests that the PU errors observed are not as frequent in the EP cases. For the EP specimens, the ZSP positioning maintains its stability where only small deviations can be observed. Therefore, it is possible to affirm that the ZSP positioning achieved a very high degree of accuracy.



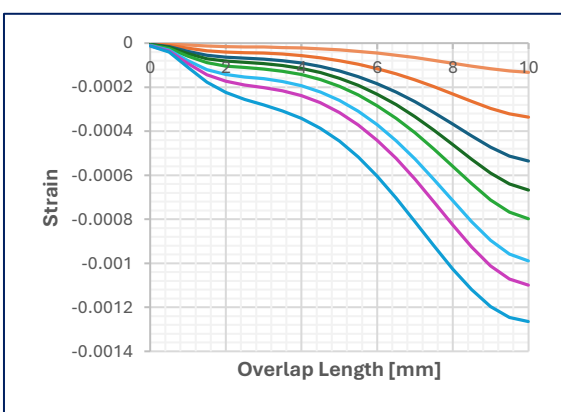
(a)



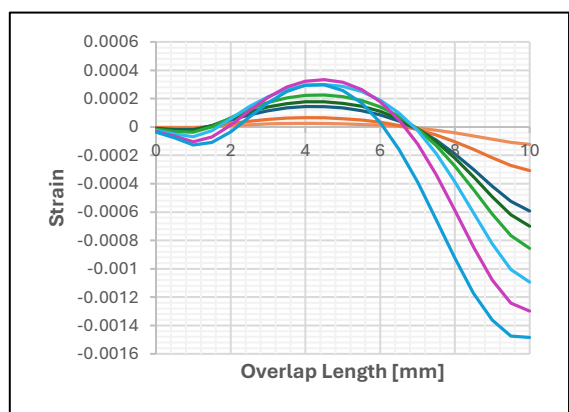
(b)



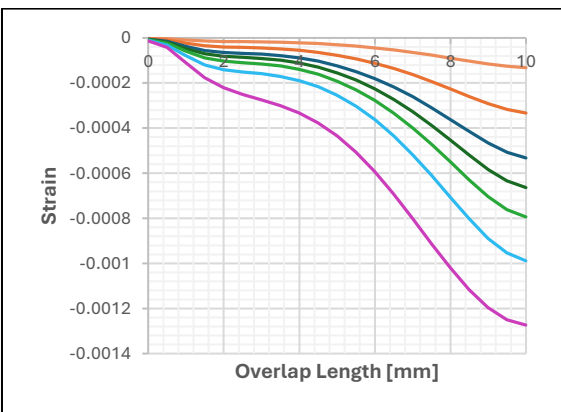
(c)



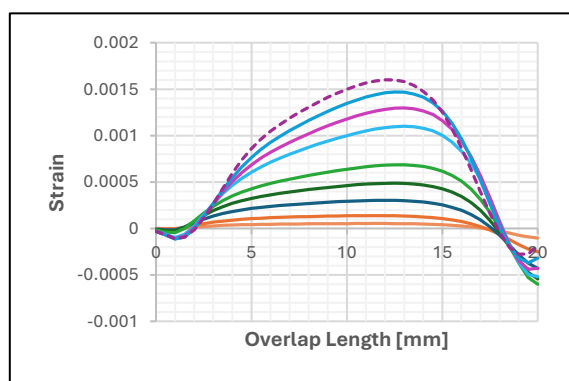
(d)



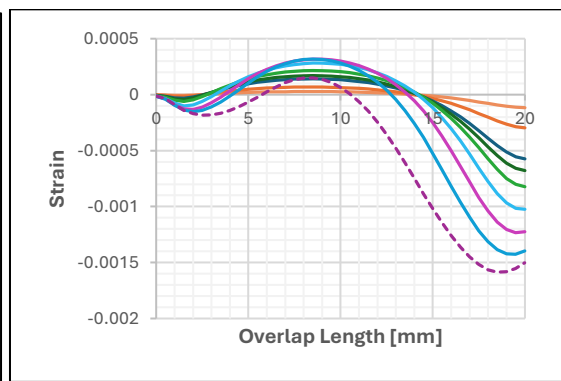
(e)



(f)



(g)



(h)

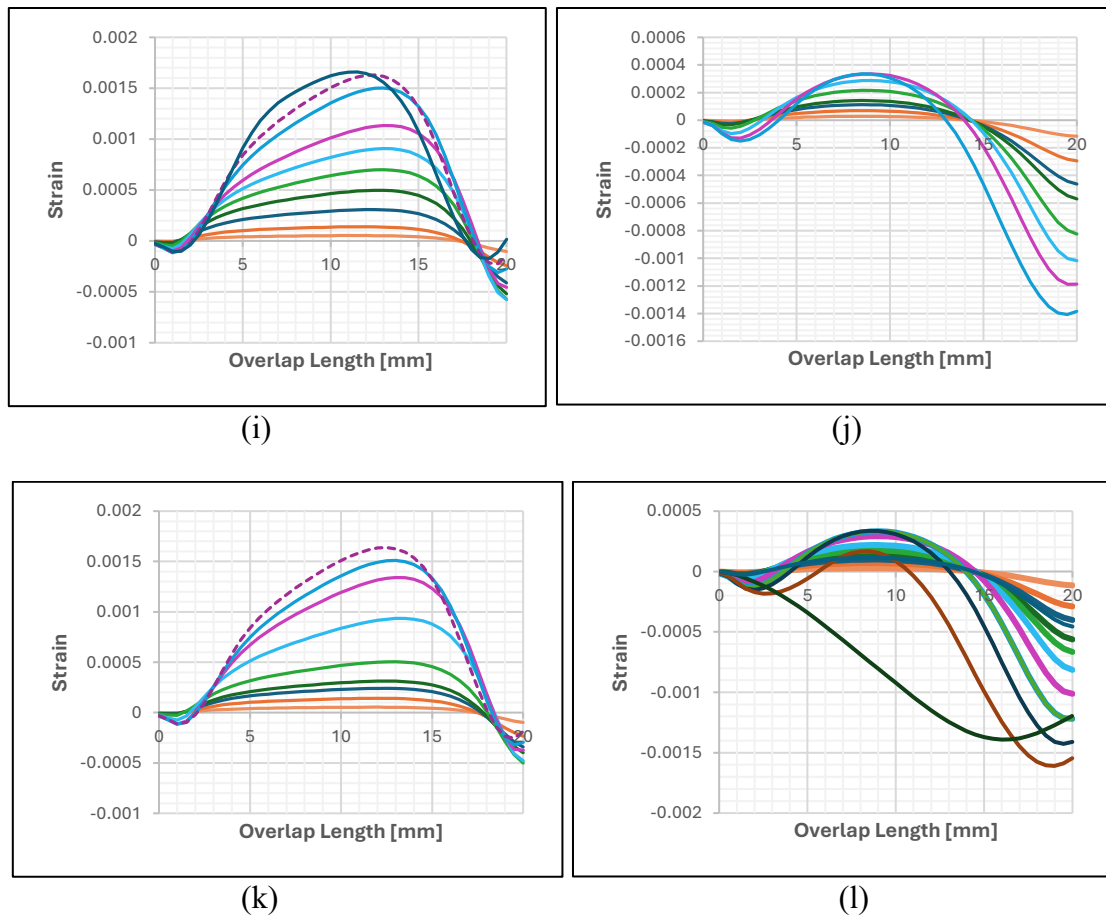
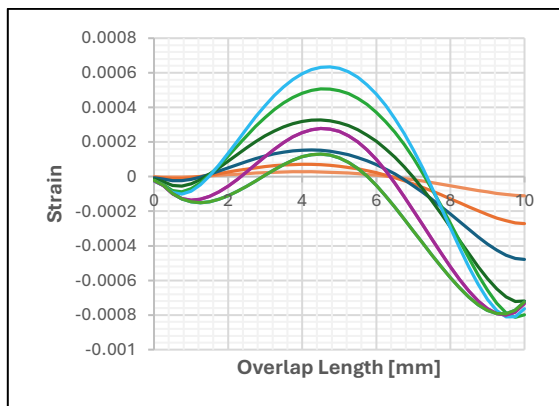


Figure 7.46: Strain Distribution and Zero Strain Point (ZSP) Locations Across Overlap Length for Various EP Specimens Using 3D Surface-Based Cohesive Approach: (a) Ep-L1W1T1, (b) Ep-L1W1T2, (c) Ep-L1W2T1, (d) Ep-L1W2T2, (e) Ep-L1W3T1, (f) Ep-L1W3T2, (g) Ep-L2W1T1, (h) Ep-L2W1T2, (i) Ep-L2W2T1, (j) Ep-L2W2T2, (k) Ep-L2W3T1, (l) Ep-L2W3T2

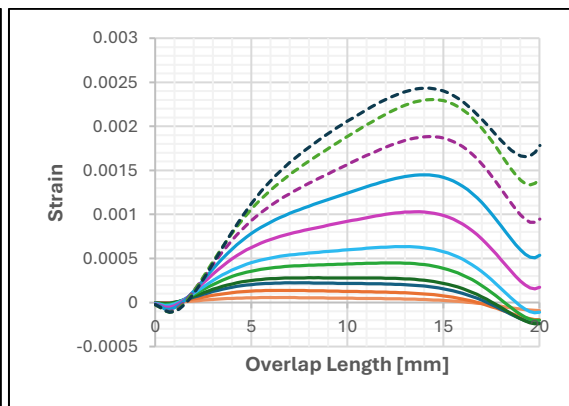
7.4.3. The Results for 2D Cohesive Element Approach

The strain distribution and ZSP locations along the overlap length for the different PU specimens using a 2D cohesive element approach are shown in Figure 7.47. The troublesome behaviour that was noticed in the 2D and 3D surface-based cohesive models persists in the ZSP location of this model, but it is exacerbated for the L2WT1 configuration. Moreover, the

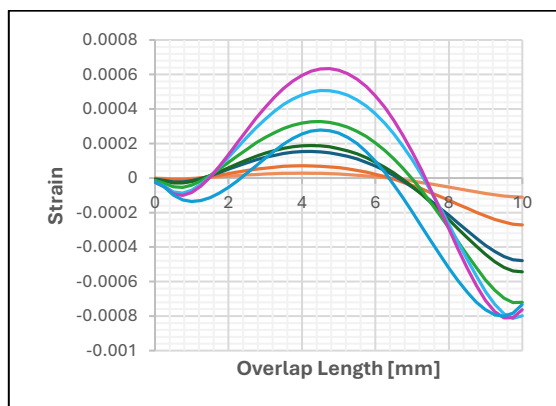
ZSP movement further along the positive strain direction goes even more in the wrong direction, away from what is expected, indicating a growing error.



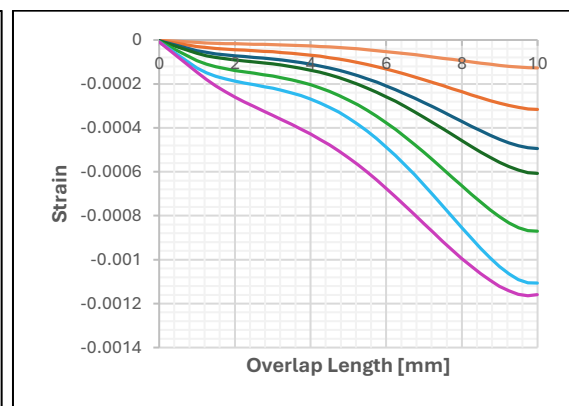
(a)



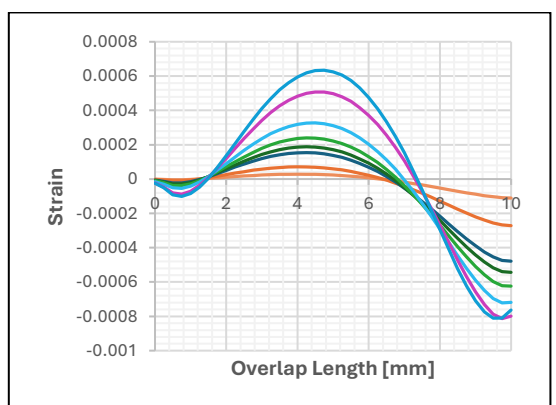
(b)



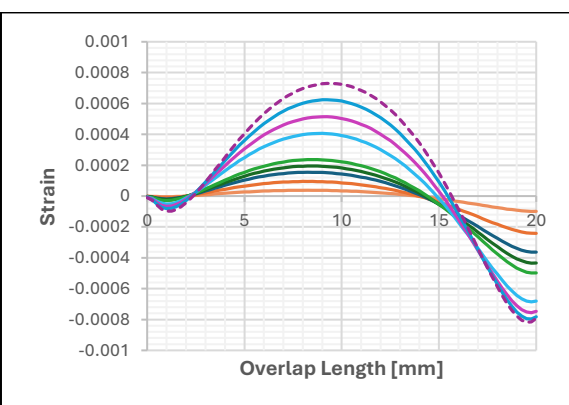
(c)



(d)



(e)



(f)

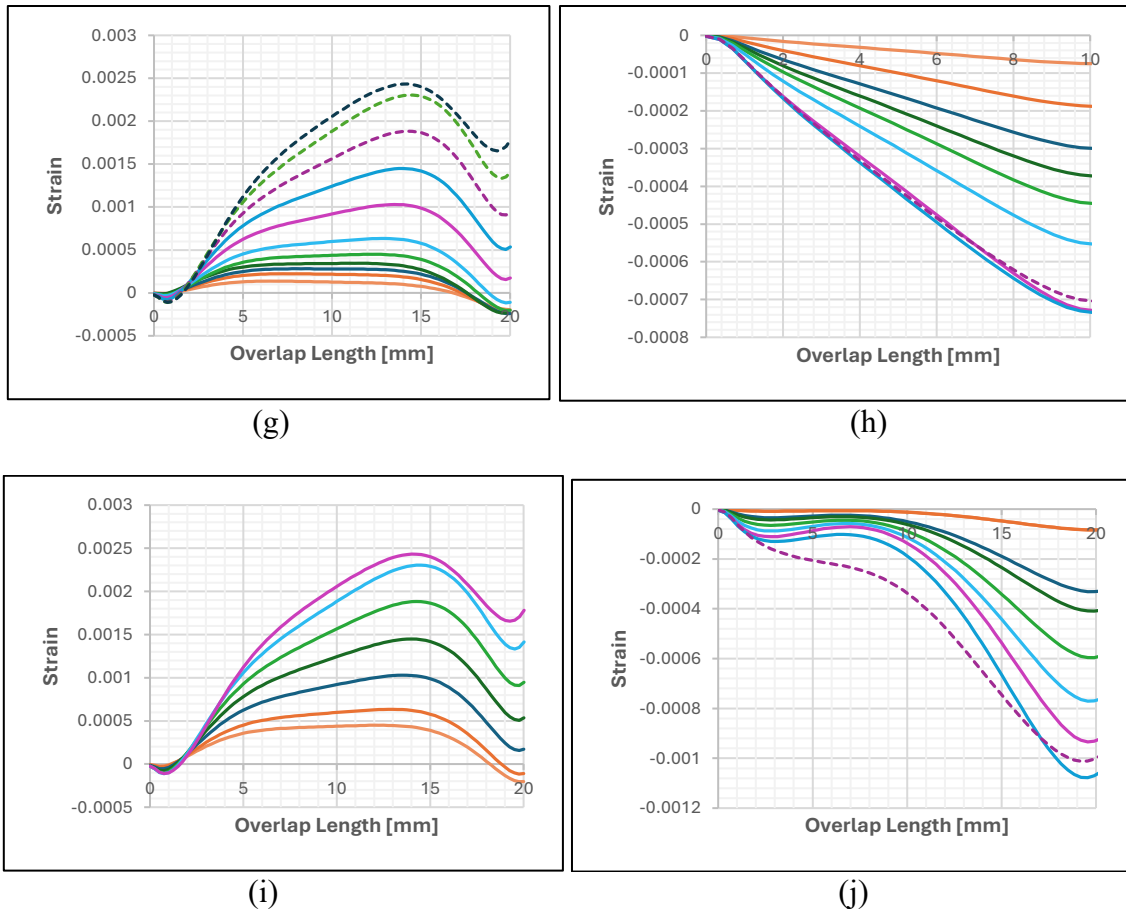
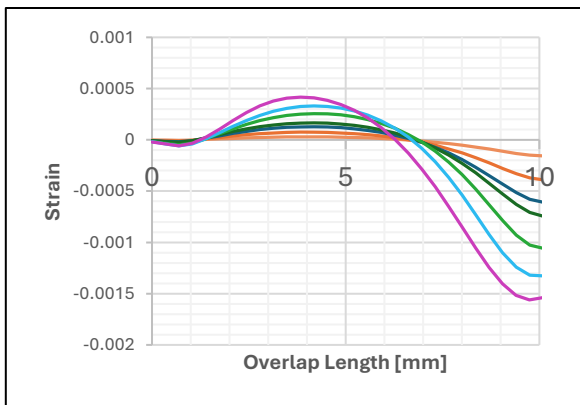
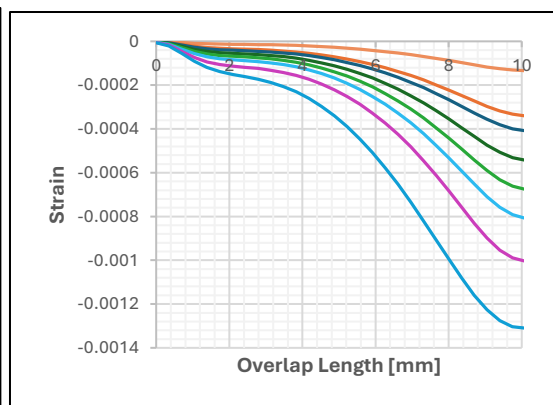


Figure 7.47: Strain Distribution and Zero Strain Point (ZSP) Locations Across Overlap Length for Various PU Specimens Using 2D Cohesive Element Approach: (a) Pu-L1W1T1, (b) Pu-L2W3T1, (c) Pu-L1W2T1, (d) Pu-L1W2T2, (e) Pu-L1W3T1, (f) Pu-L2W2T2, (g) Pu-L2W1T1, (h) Pu-L1W2T3, (i) Pu-L2W2T1, (j) Pu-L2W2T3

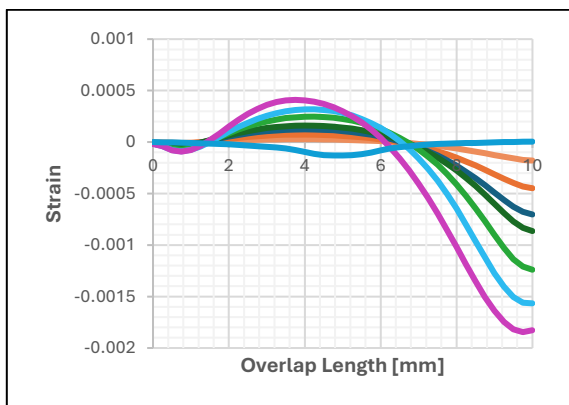
The outputs shown for the EP specimens with the 2D cohesive element method (Figure 7.48) demonstrate that the behaviour of the ZSP did not change with the different configurations. Unlike the PU ones, it is not observed any of the big anomalies or shifts for those, especially for the key configurations such as L2WT1. The ZSP exhibits trends that are consistent with expectations, and the strain evolution along the overlap length is in good agreement with the experimental and the numerical data.



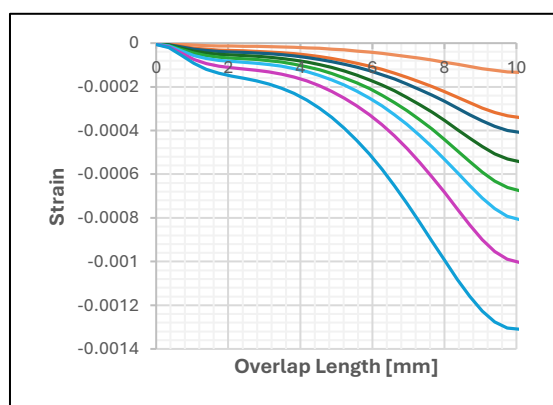
(a)



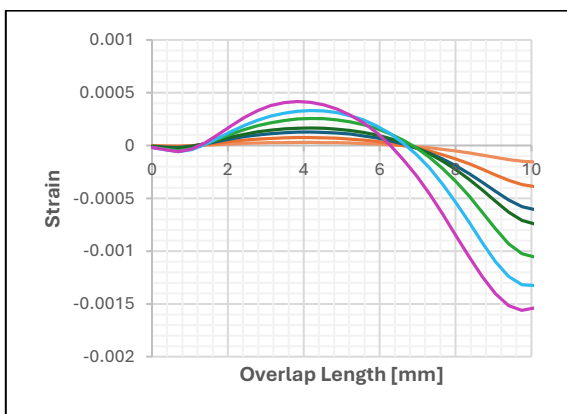
(b)



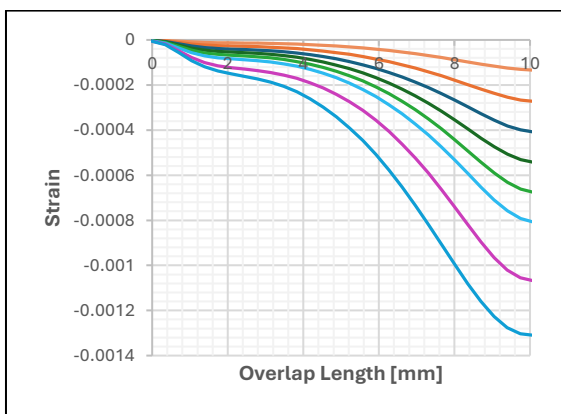
(c)



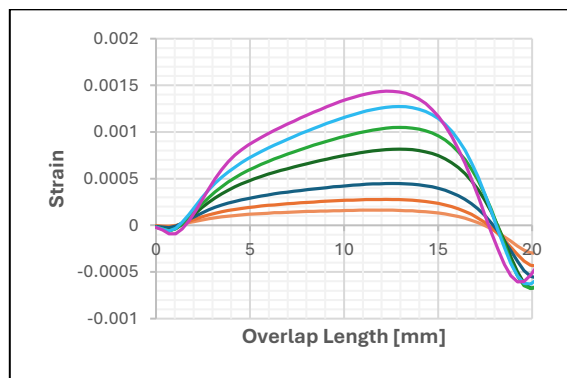
(d)



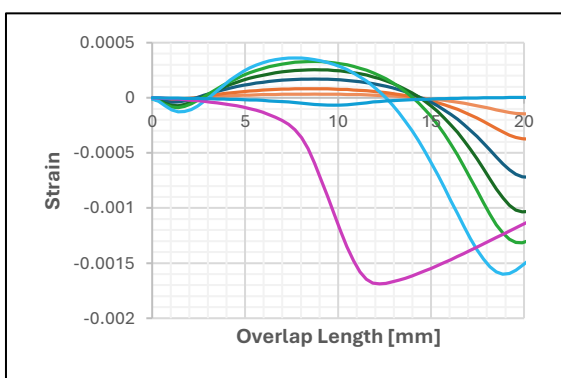
(e)



(f)



(g)



(h)

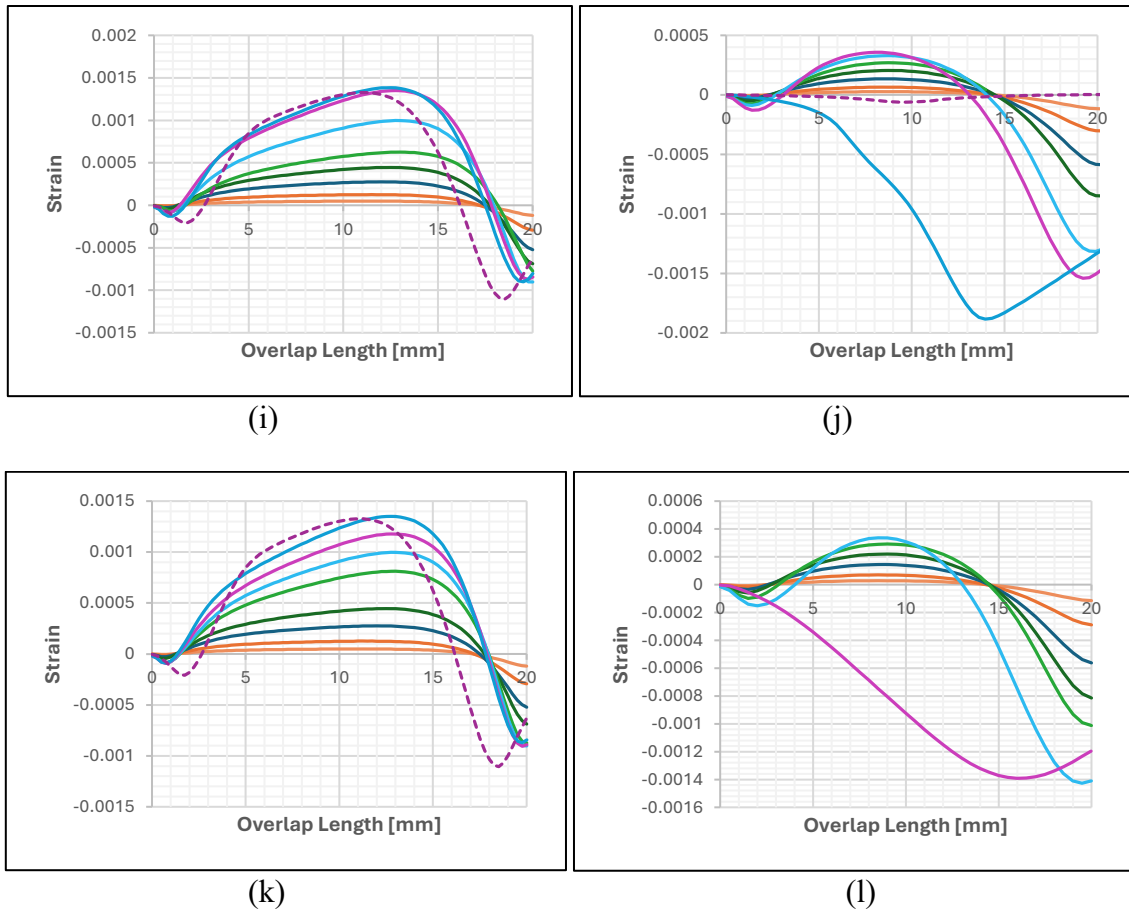


Figure 7.48: Strain Distribution and Zero Strain Point (ZSP) Locations Across Overlap Length for Various EP Specimens Using 2D Cohesive Element Approach: (a) Ep-L1W1T1, (b) Ep-L1W1T2, (c) Ep-L1W2T1, (d) Ep-L1W2T2, (e) Ep-L1W3T1, (f) Ep-L1W3T2, (g) Ep-L2W1T1, (h) Ep-L2W1T2, (i) Ep-L2W2T1, (j) Ep-L2W2T2, (k) Ep-L2W3T1, (l) Ep-L2W3T2

Figure 7.49 presents the ZSP position for the polyurethane adhesive, showing small deviations between numerical and experimental data across all the specimens. While it is seen that there is an overestimation of the location of ZSP with the 3D surface-based method, the 2D surface-based method seems to present closer predictions in few cases but still slightly deviates in some instances from the expected locations. On the other hand, 3D surface-based and 2D element-based cohesive methods are not able to catch the ZSP for the specimens

L1W2T2 and L2W2T3, while 2D surface-based model is successful. For the L1W2T3, none of these numerical models capture the ZSP. However, the ZSP is not clearly revealed experimentally for this sample.

Referring to epoxy adhesive, it can be seen in Figure 7.50 that numerical models are better at predicting experimental ZSP positions. These deviations are more moderate than the specimens with polyurethane adhesive. The experimental curve for both 2D and 3D cohesive models are able to capture the trend well.

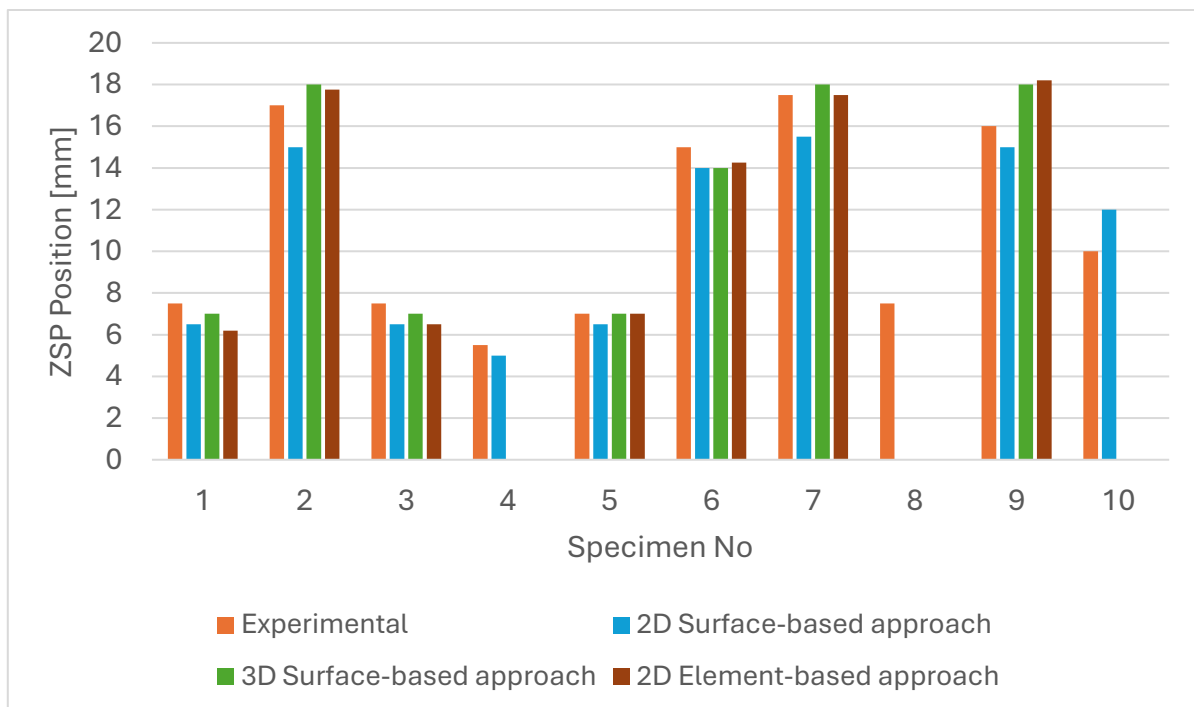


Figure 7.49: Comparison of ZSP Position Across Specimens with Polyurethane Adhesive

(1:Pu-L1W1T1, 2:Pu-L2W3T1, 3:Pu-L1W2T1, 4:Pu-L1W2T2, 5:Pu-L1W3T1, 6:Pu-L2W2T2, 7:Pu-L2W1T1, 8:Pu-L1W2T3, 9:Pu-L2W2T1, 10:Pu-L2W2T3)

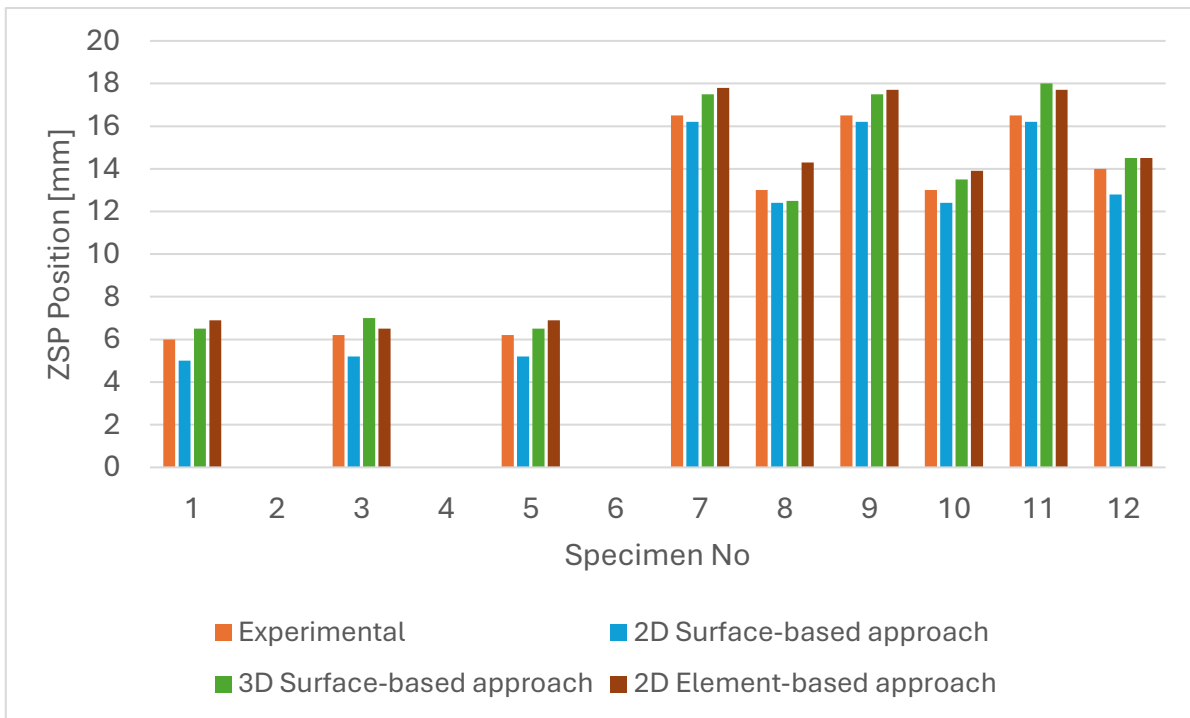


Figure 7.50: Comparison of ZSP Position Across Specimens with Epoxy Adhesive (1:Ep-L1W1T1, 2:Ep-L1W1T2, 3:Ep-L1W2T1, 4:Ep-L1W2T2, 5:Ep-L1W3T1, 6:Ep-L1W3T2, 7:Ep-L2W1T1, 8:Ep-L2W1T2, 9:Ep-L2W2T1, 10:Ep-L2W2T2, 11:Ep-L2W3T1, 12:Ep-L2W3T2)

7.5. Force-Displacement Analysis for All Specimens

7.5.1. The Results of 2D Surface-Based Approach for Polyurethane Adhesive

Figure 7.49 shows the experimental force-displacement graph of samples with polyurethane adhesive. As evident from the force-displacement relationship of the polyurethane specimens shown in Figure 7.51, the 2D surface-based cohesive approach exhibits fairly good overall agreement with experimental data in terms of peak force magnitudes. Compared to experimental results, the numerical predictions often display earlier peak displacements.

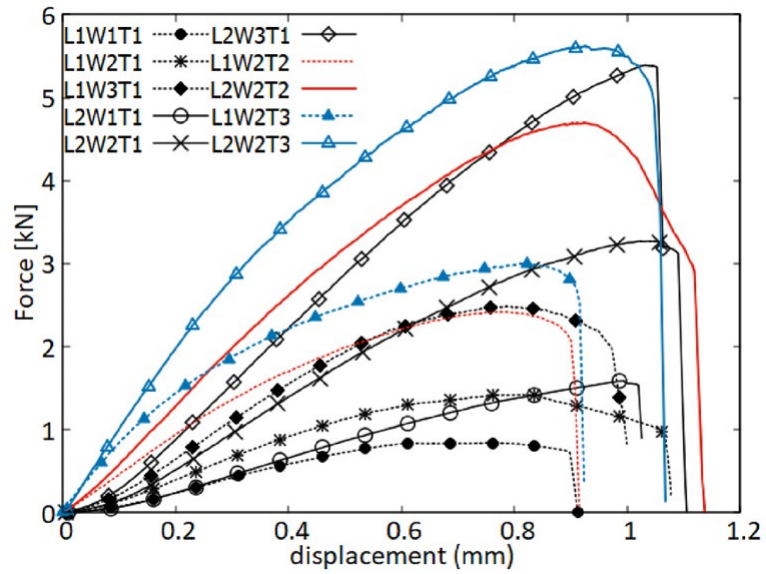


Figure 7.51: Experimental Load-Displacement curve for Polyurethane adhesive specimens [9]

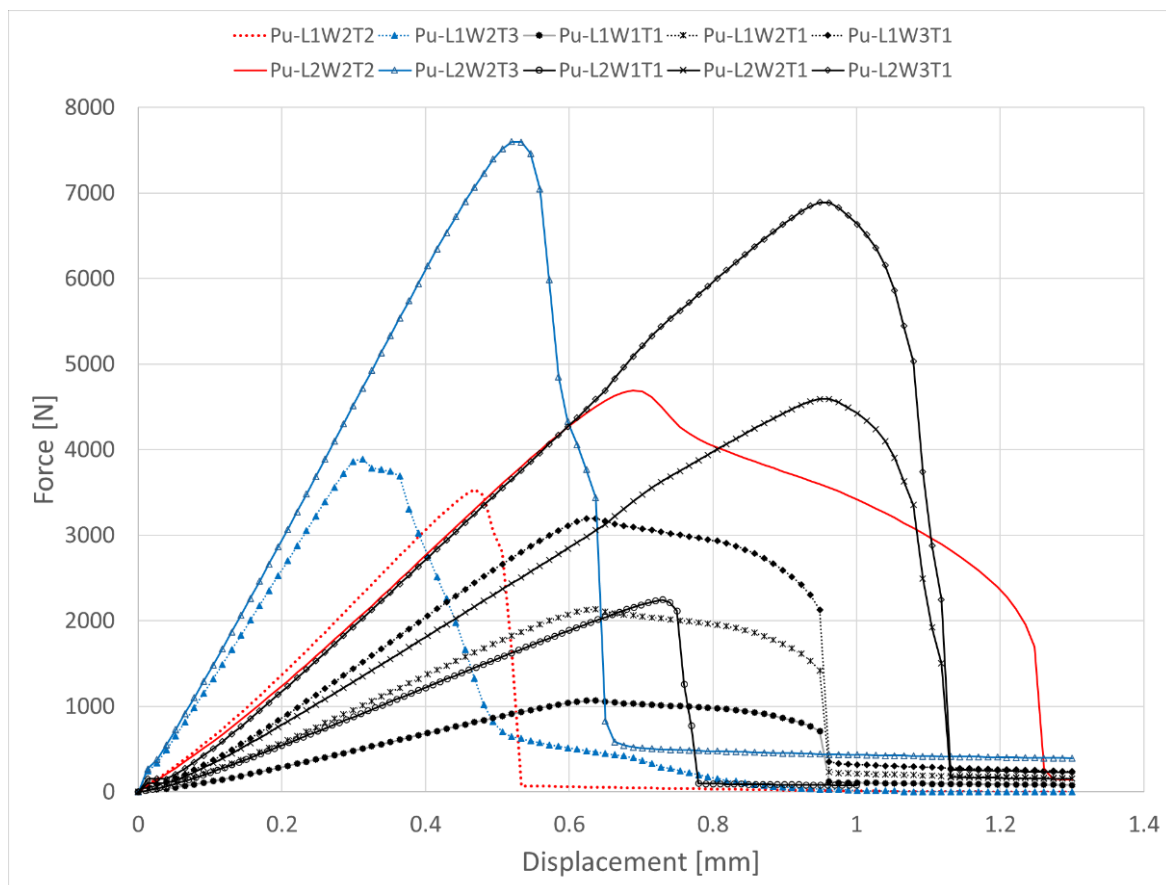


Figure 7.51: 2D Surface-Based Cohesive Method in Load-displacement curves of Polyurethane different specimens

7.5.2. The Results of 3D Surface-Based Approach for Polyurethane Adhesive

The force-displacement curve of polyurethane specimens obtained through the 3D surface-based cohesive model are shown in Figure 7.52. The predictions show a reasonable level of accuracy to capture overall force trends and peak force magnitudes. Compared to experimental results, the numerical predictions often display earlier peak displacements.

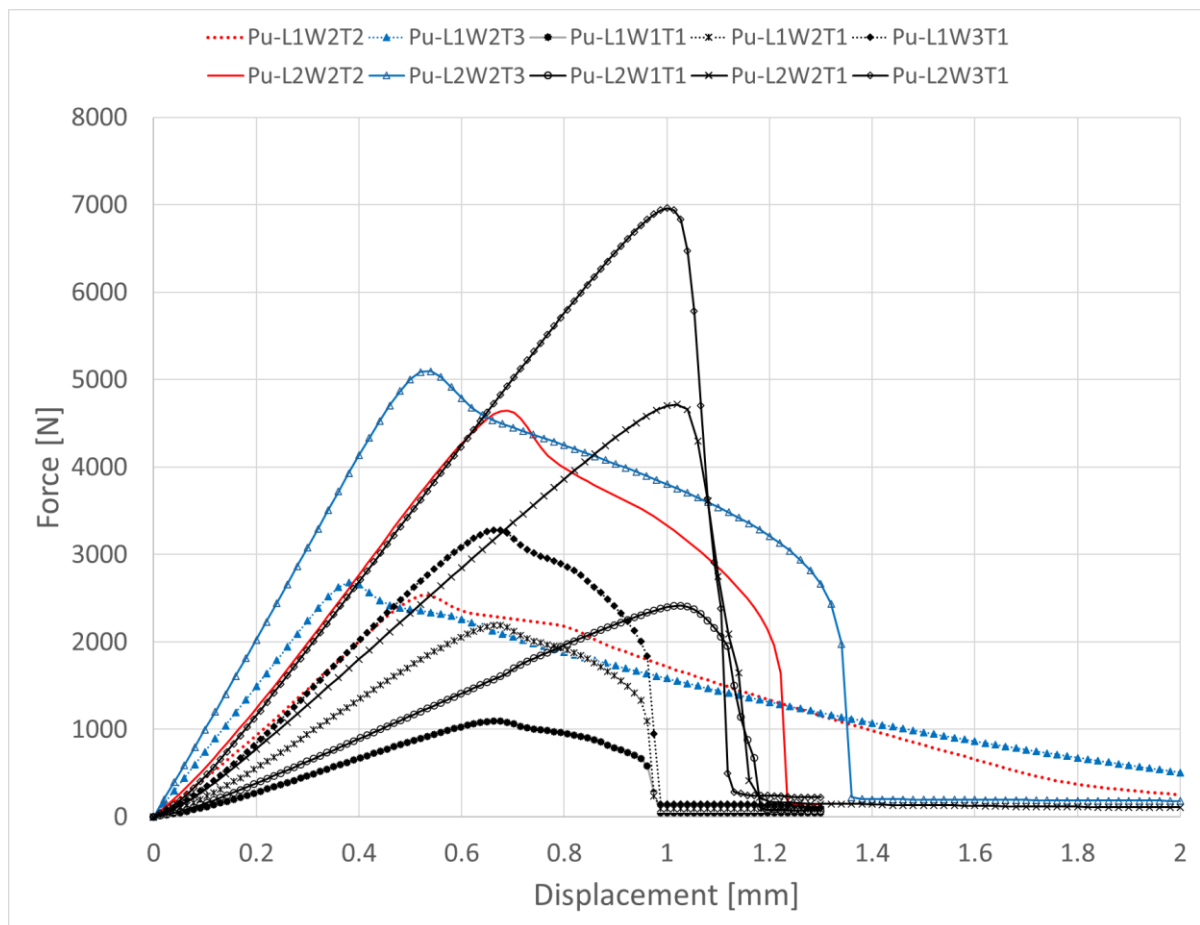


Figure 7.52: 3D Surface-Based Cohesive Method in Load-displacement curves of Polyurethane different specimens

7.5.3. The Results of 2D Cohesive Element Approach for Polyurethane Adhesive

The force-displacement curves of the polyurethane specimens obtained from 2D cohesive element (Fig. 7.53) were also compared to that of the experimental data in Figure

7.51. The numerical results show good agreement with the are with experimental data including the overall force response and maximum force levels. Compared to experimental results, the numerical predictions often display earlier peak displacements.

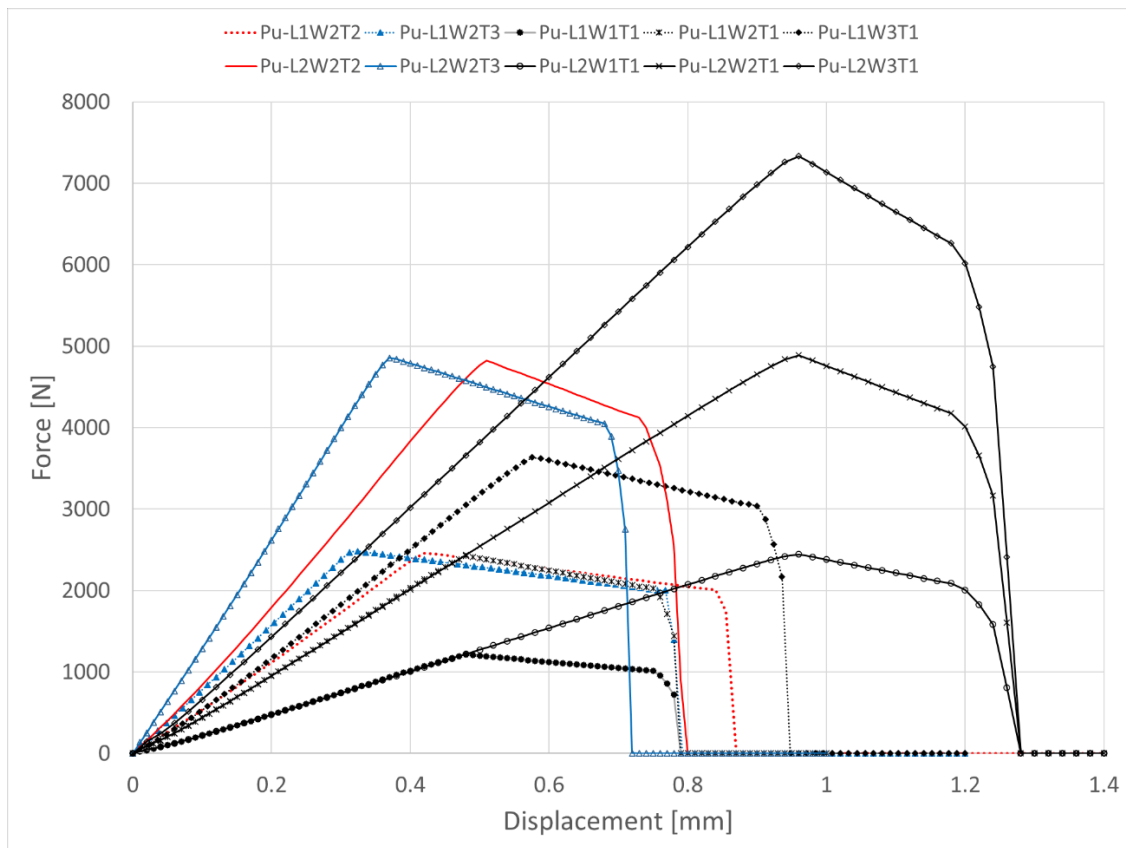


Figure 7.53: 2D Cohesive Element Method in Load-displacement curves of Polyurethane different specimens

7.5.4. The Results of 2D Surface-Based Cohesive Approach for Epoxy Adhesive

Figure 7.54 shows the experimental force-displacement graph of samples with epoxy adhesive. Figure 7.55 shows the force-displacement curves of epoxy specimens employing the 2D surface-based cohesive. The numerical results match well with the experimental curves, both in the maximal force and the shape of the response. Most of the configurations show a good fit of numerical curves based on the experimental data.

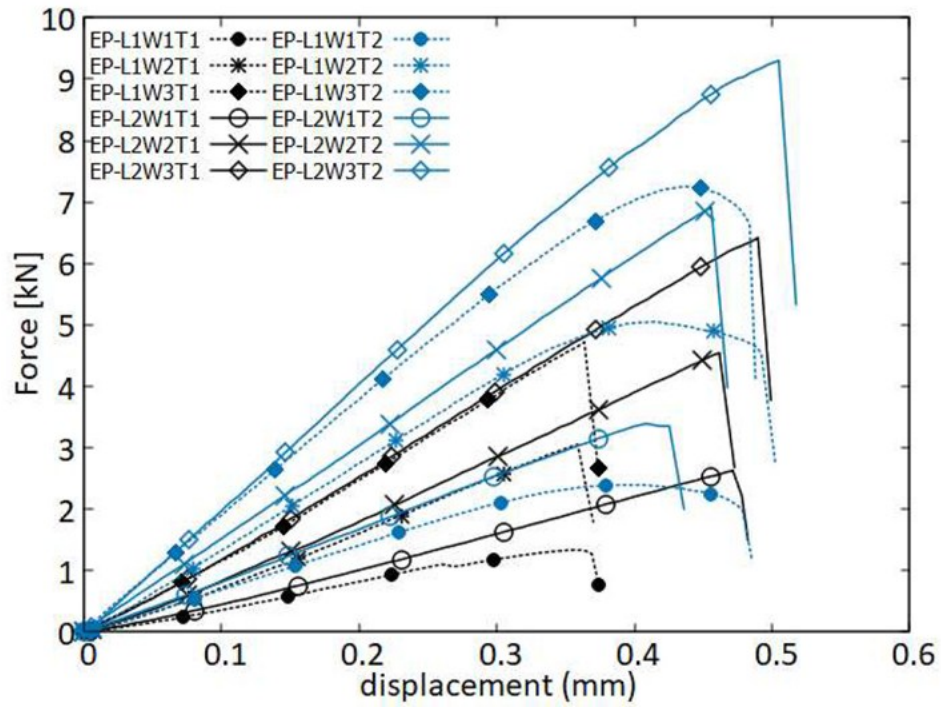


Figure 7.54: Experimental Load-Displacement curve for Epoxy adhesive specimens [6]

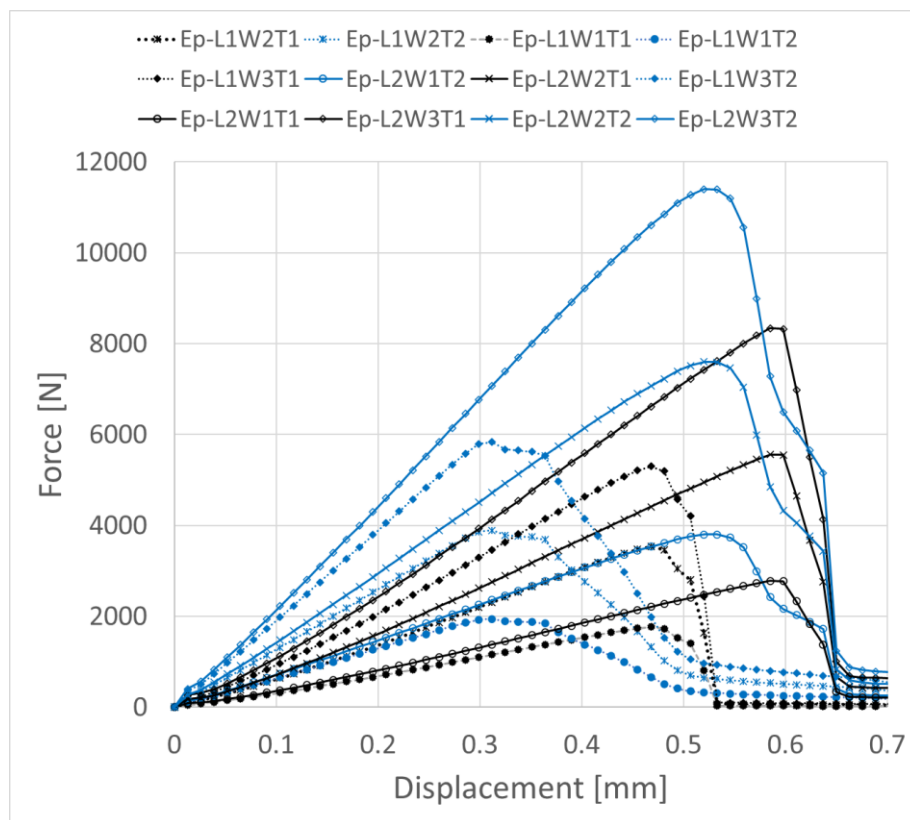


Figure 7.55: 2D Surface-Based Cohesive Method in Load-displacement curves of Epoxy different specimens

7.5.5. The Results of 3D Surface-Based Cohesive Approach for Epoxy Adhesive

In Figure 7.56 shows numerical force-displacement curves of epoxy specimens using 3D surface-based cohesive approach. Deviations are particularly pronounced in some specimens.

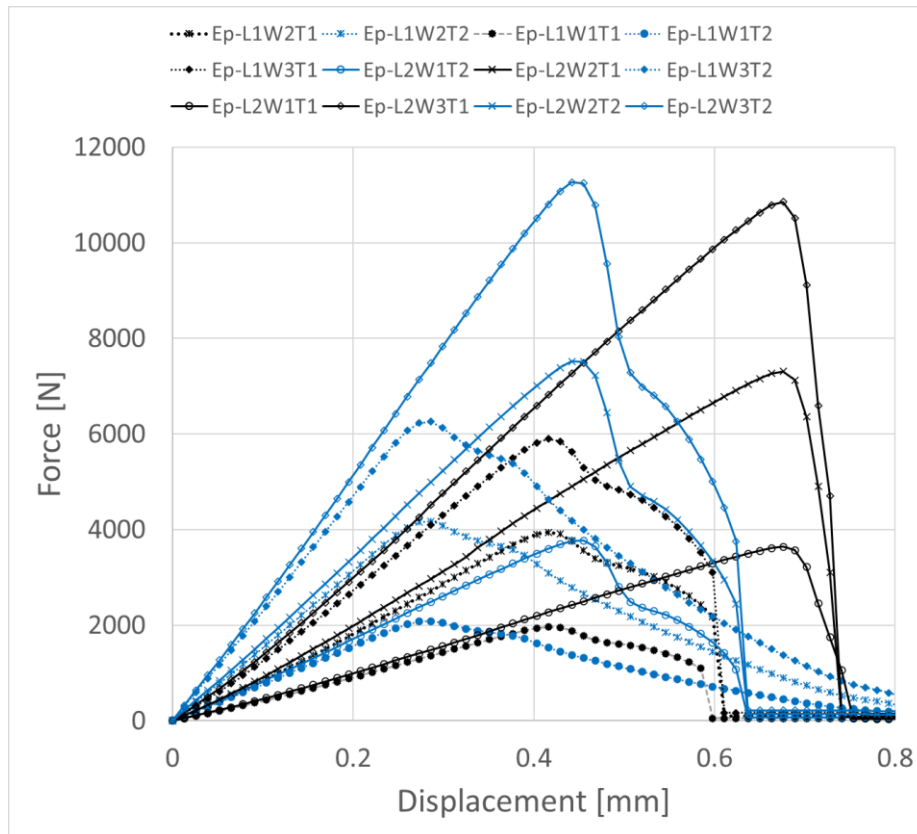


Figure 7.56: 3D Surface-Based Cohesive Method in Load-displacement curves of Epoxy different specimens

7.5.6. The Results of 2D Cohesive Element Approach for Epoxy Adhesive

The force-displacement curves of the specimens with epoxy specimens by using 2D cohesive element approach is presented in Figure 7.57. Numerical results show a fair agreement with the experimental data, especially regarding the maximum force and displacement at maximum force values.

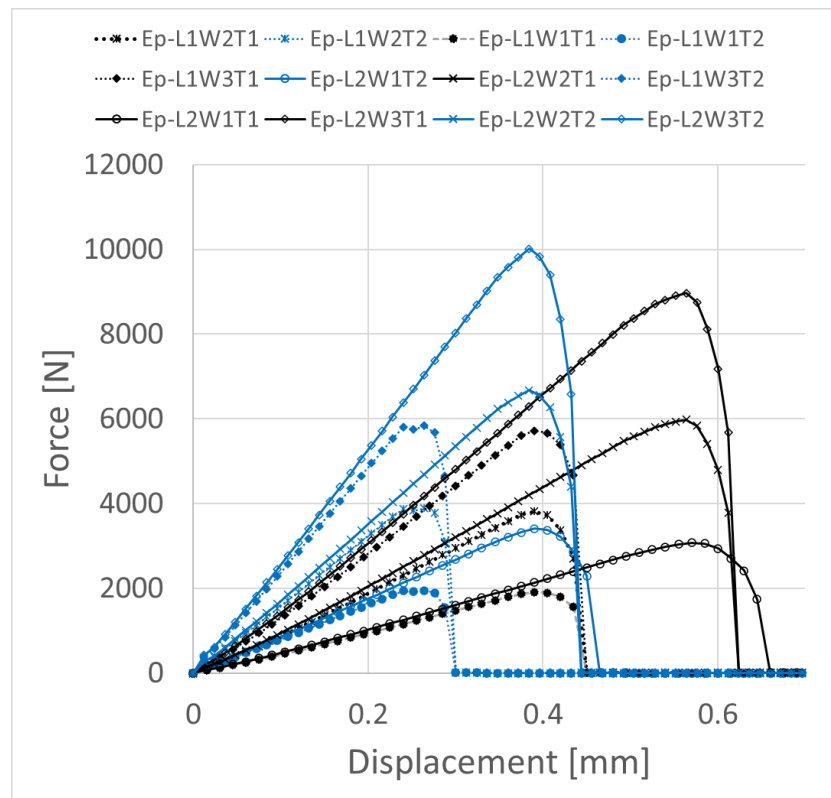


Figure 7.57: 2D Cohesive Element Method in Load-displacement curves of Epoxy different specimens

Load and displacement at peak load for polyurethane and epoxy adhesives have been compared between numerical and experimental results. As shown in the peak load comparison for polyurethane adhesive in Figure 7.58, the 2D surface-based approach generally overestimates the experimental values, especially in specimens 4, 8 and 10. Likewise for polyurethane adhesive, as seen in Figure 7.59, the displacement at peak load values are consistently underestimated by all numerical models with again a significant difference, particularly for specimens 4, 8 and 10.

In the case of epoxy adhesive, the numerical predictions fit better with the experimental results than the polyurethane in Figures 7.60 and 7.61. More importantly, the differences are smaller, and force-displacement trends are more consistent among diverse modelling approaches.

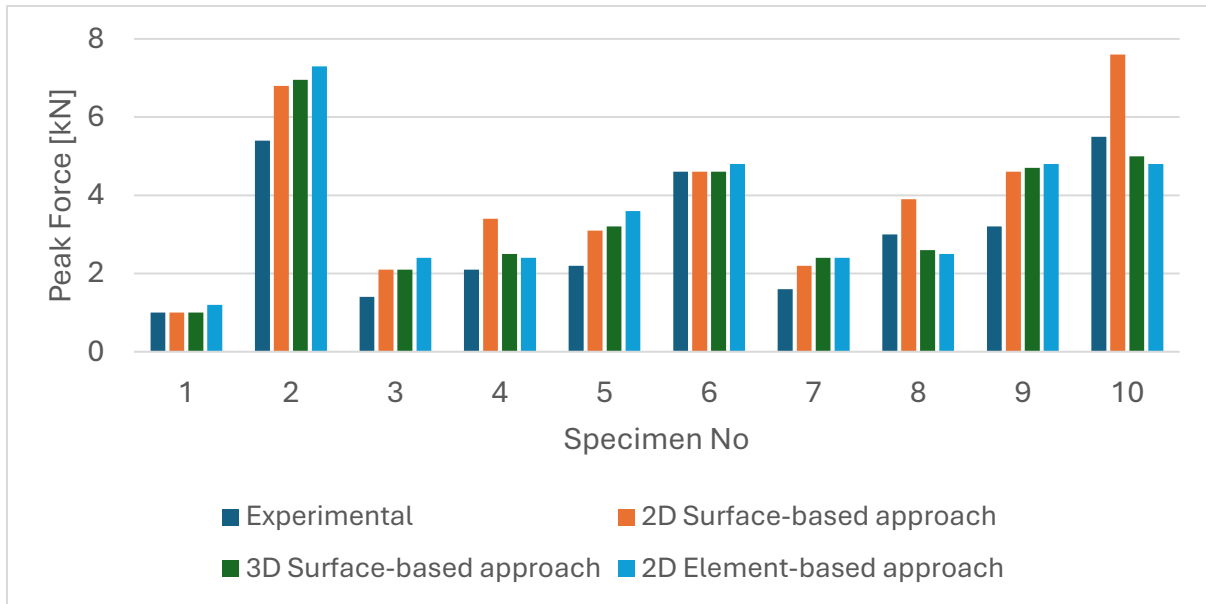


Figure 7.58: Peak Load Comparison Across Specimens with Polyurethane Adhesive (1:Pu-L1W1T1, 2:Pu-L2W3T1, 3:Pu-L1W2T1, 4:Pu-L1W2T2, 5:Pu-L1W3T1, 6:Pu-L2W2T2, 7:Pu-L2W1T1, 8:Pu-L1W2T3, 9:Pu-L2W2T1, 10:Pu-L2W2T3)

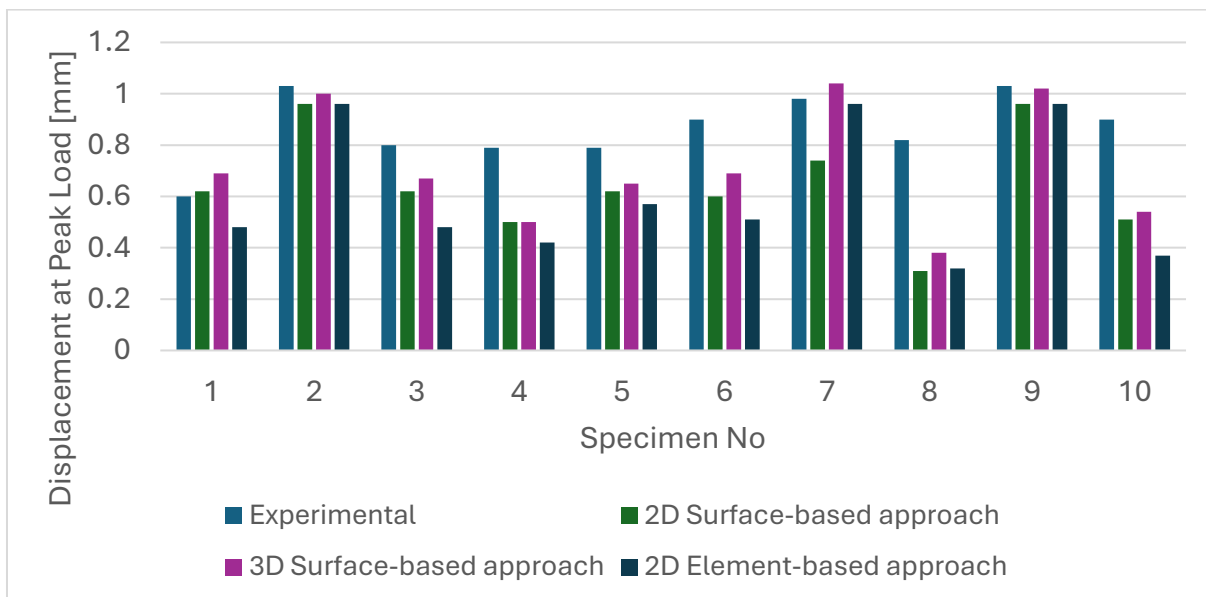


Figure 7.59: Displacement at Peak Load for Different Approaches Across Specimens with Polyurethane Adhesive (1:Pu-L1W1T1, 2:Pu-L2W3T1, 3:Pu-L1W2T1, 4:Pu-L1W2T2, 5:Pu-L1W3T1, 6:Pu-L2W2T2, 7:Pu-L2W1T1, 8:Pu-L1W2T3, 9:Pu-L2W2T1, 10:Pu-L2W2T3)

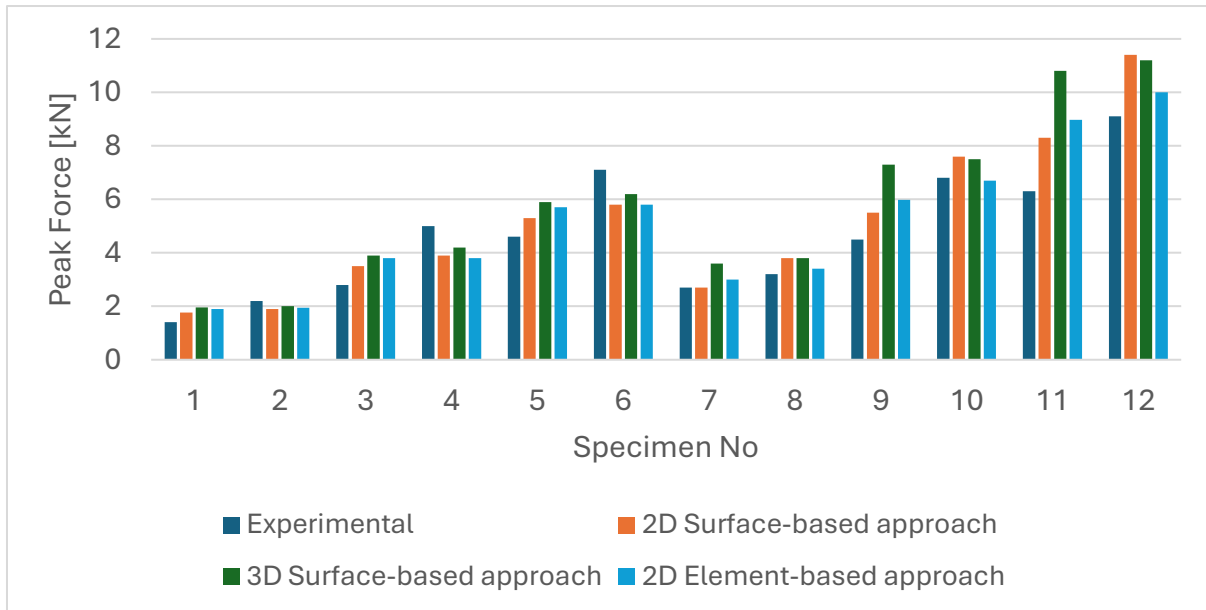


Figure 7.60: Peak Load Comparison Across Specimens with Epoxy Adhesive (1:Ep-L1W1T1, 2:Ep-L1W1T2, 3:Ep-L1W2T1, 4:Ep-L1W2T2, 5:Ep-L1W3T1, 6:Ep-L1W3T2, 7:Ep-L2W1T1, 8:Ep-L2W1T2, 9:Ep-L2W2T1, 10:Ep-L2W2T2, 11:Ep-L2W3T1, 12:Ep-L2W3T2)

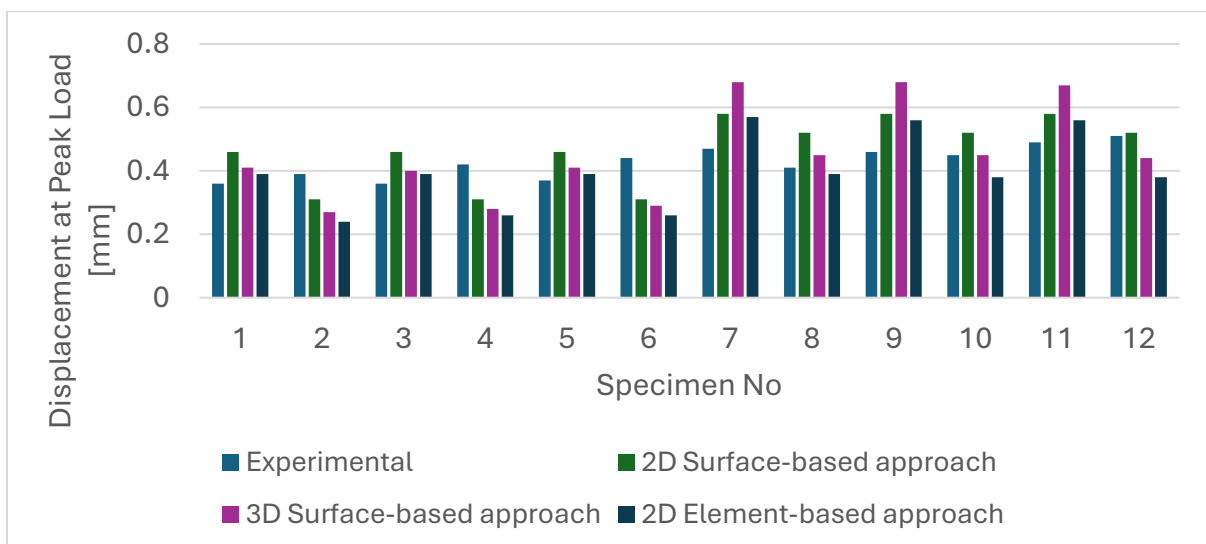


Figure 7.61: Displacement at Peak Load for Different Approaches Across Specimens with Epoxy Adhesive (1:Ep-L1W1T1, 2:Ep-L1W1T2, 3:Ep-L1W2T1, 4:Ep-L1W2T2, 5:Ep-L1W3T1, 6:Ep-L1W3T2, 7:Ep-L2W1T1, 8:Ep-L2W1T2, 9:Ep-L2W2T1, 10:Ep-L2W2T2, 11:Ep-L2W3T1, 12:Ep-L2W3T2)

8. DISCUSSION

The accuracy of the cohesive zone models was attributed to the effective interface modelling without the computational complexity of the cohesive elements [82]. Although the cohesive surface method cannot explicitly capture the thickness deformation, it was able to replicate the global force-displacement trend with high accuracy through the adjusted material properties. This highlights the need to appropriately calibrate these models, especially for critical parameters, such as interface stiffness, shear strength, and fracture energy. (Table 4.1, 4.2, 4.3, 4.4)

As in Figure 7.5, the ZSP in the numerical model moves in negative strain zones as the applied load increases. This trend is well captured by the numerical model, which is consistent with the actual behaviour of the joint, where the strain distribution over the backface is shifted more towards the negative values reflecting the role of adhesive deformation mechanism, and load redistribution. This agreement between experimental data and numerical predictions underscores the capability of the model to robustly reproduce strain evolution for diverse levels of loading.

But one important difference concerns the scale of strain values. The numerical model widely underestimates strain values from the experimental measurements (Figure 7.5 & Table 7.5). The underestimation could result from several reasons such as assumed material properties, possible simplifications in the cohesive zone model, and mesh sensitivity. Even with this limitation as demonstrated its ability to follow the overall trend and detect the ZSP is practically reliable.

Another significant difference identified from the experimental and numerical results is the fluctuations of strain distribution on the overlap length identified in the experimental graph (Figure 7.4). These variations stem from the warp and weft structure intrinsic to the

composite adherends, [09] which lead to localized differences in stiffness and strain response. Unsurprisingly, the numerical model does not reproduce the structural dynamics and all fluctuations associated with it (Figure 7.5). The orthotropic elastic properties specified in the model provide an averaged, homogenized stiffness factor that suppresses some of the local phenomena seen with the experimental measurements.

In the Figure 7.6 & Figure 7.7, the non-linear behaviour can be explained by the linear viscoelasticity of polyurethane [81]. Linear viscoelasticity explains that there is an elastic deformation, as well as time-dependent recoverable strain [83, 84]. This results in a gradual increase of strain even for measurements which remain in the nominally linear region of the material, and therefore accounts for the non-linear drift of the ZSP in the initial loading stage.

When the applied force approaches the maximum load, the strain grows rapidly, indicating that the majority of the viscoelastic deformation and the bond interface damage have occurred at that moment. (Fig. 7.6) This is seen as the force reaches a peak value after which the force and the strain both drop rapidly, which is representative of adhesive failure and debonding [85].

Furthermore, this discrepancy illustrates one of the modelling issues on accurately reflecting the behaviour of polyurethanes. Since a linear traction-separation relation is used in this study as cohesive zone model, this fails to reflect the progressive strain accumulation associated with the viscoelastic or plastic nature of polyurethane [28]. Future model improvements may include implementing a nonlinear viscoelastic or viscoplastic constitutive law [81] to enable the numerical predictions to more closely replicate the experimental ZSP behaviour for differing strain treatments during loading.

In the Figure 7.19, Figure 7.21, Figure 7.23, Figure 7.45b or Figure 7.47b, the similarity of the errors made by 2D and 3D model indicates that this issue is potentially not related to geometrical dimensionality of a model and rather towards localization of material

stress concentrations, numeric or properties related errors due to the linear TSL model.

Overall, most specimens show good agreement. However, the uncertainty observed in the ZSP behaviour at high loads for Pu-L2WT1. This represents from the perfect agreement with the experimental data would necessitate further investigation.

However, unlike the PU specimens, in Figure 7.46, as a result of the lower sensitivity of EP specimens to modelling, the EP specimens tend to much better simulate the physical adhesive behaviour against elevated loads.

Previously, some interactions and material definition led to further error accumulation and led to inconsistencies as those portrayed in case L2WT1, in the Figure 7.47 at cohesive element model. It emphasizes the underlying corresponding inaccuracies with previous configurations. The worsening of ZSP positioning means that adhesive layer modelling approach has important consequences on the range of accuracy for PU specimens and may be more susceptible to mistakes under certain conditions.

As a final note, the relative constancy of the results presented in Figure 7.48 may indicate that the cohesive element approach is more accurate for the EP specimens than the PU specimens.

In most of the numerical simulations in this study, the displacement corresponding to peak force occurred earlier than corresponding experimental results. This early event may suggest minor discrepancies in the stiffness representation or failure initiation criteria of the numerical model. Although the numerical force response curves match each other well, the differences in maximum force data may be responsible for some of the discrepancies in strain localization.

Figure 7.59 also shows discrepancies for the displacement at which the peak force is reached for the specimens with polyurethane. In almost all numerical models, the models generally over-predict peak force at lower displacements compared to experimental data. This

early peak displacement indicates that failure initiation in the cohesive interface may influence this parameter. Analogously, the mismatch observed in Figure 7.59 may imply that the cohesive element approach still triggers failure too early.

The accuracy of the predicted values is adhesive dependent. It can be concluded from Figure 7.58 and Figure 7.59 that polyurethane adhesive is more difficult to model numerically due to its ductile and viscoelastic nature. Analysis shows the force predictions in the 2D surface-based approach are more challenging whereas displacement predictions are usually underestimated. This highlights the limitation of cohesive modelling of polyurethane.

Conversely, Figs. 7.60 and 7.61 show that numerically, epoxy adhesive, due to its higher stiffness and brittle nature, has more accurate results. Both the 2D and 3D surface-based cohesive methods improved results from the element-based approach, with the largest difference obtained in displacements at the maximum load. Although the 3D surface-based method showed a small increase in accuracy, its high computational cost may not be warranted in every case.

The differences indicate that some material modelling, especially for the polyurethane, may require further refinement, including mixed-mode damage parameters and rate-dependent effects.

9. CONCLUSIONS

The quantitative determination of the Zero Strain Point position across different arrangements is consistently accomplished by both adhesives. The detection of ZSP was consistent with experimental results even for L2W1T1, which exhibited significant numerical defects in ZSP trend at elevated loads. Such a trend reinforces the reliability of numerical models in monitoring strain distribution, as there are no notable deviations in the identification of the ZSP. Overall, both the surface-based cohesive and cohesive element approaches accurately capture ZSP locations for both the epoxy and polyurethane adhesives.

For polyurethane specimens, strain distribution and trends with force-displacement showed some anomalies at elevated loads for configurations like L2WT1. But for the other specimens, general trend is accurate. Element-based model suffers from larger inaccuracies compared to surface-based models, resulting in polyurethane remaining a challenging material to represent under load. While this behaviour was seen in polyurethane, epoxy specimens did not experience major deviation in ZSP detection, strain distribution, or force-displacement behaviour. Numerical predictions are consistent with low variability, attributed to the lower ductility and predictable damage growth of epoxy for 2D and 3D models.

Another implication is related to mesh densities in 2D and 3D cohesive element approaches and in particular, significant inaccuracies arise when simulating the evolution of gradual damage due to the higher computational costs of 3D models. The better performance of the surface-based cohesive approach can largely be attributed to the physical basis behind the failure modes. In practical scenarios for these specimens, failure typically is led along the adhesive-adherend interface (adhesive failure) [85] and such a phenomenon can be accurately replicated by employing shear response only at the surface-based cohesive method. Moreover, this method is less mesh-dependent and more accurately represents the actual

failure mechanism than cohesive elements, which model the through-thickness behaviour and can easily deviate from physical reality for these specimens.

Future improvements in optimization of material properties using experimental calibration, 3D mesh refinement and development of different shape traction-separation laws or nonlinear cohesive models for materials that exhibit viscoelastic behaviour may further reduce the inconsistencies and contribute to more reliable FEM simulations.

10. REFERENCES

1. Marques, E. A. S., Carbas, R. J. C., Akhavan-Safar, A., Tenreiro, A. F. G., & da Silva, L. F. M. (Year). *Structural Adhesive Bonding in Aerospace Applications*. Quântica Editora.
2. M. Jenny, "Advantages and challenges of implementing lightweight materials in automobiles: A review," *Int. J. Sci. Res. Publ.*, vol. 13, no. 9, Sep. 2023, doi: 10.29322/IJSRP.13.09.2023.p14116.
3. *Introduction to Modeling Structural Adhesives*. 3M, 2019.
4. *Virtual Material Testing of Adhesive Joints*. DiVA Portal, 2019.
5. Liu and R. Yan, "Damage mechanism and residual strength at different impact locations for composite bonding scarf repairs," *J. Adhes. Sci. Technol.*, vol. XX, 2018. DOI: 10.1080/01694243.2018.1492282.
6. M. Abbasi, R. Ciardiello, and L. Goglio, "Backface strain as an index to detect damage initiation in composite single-lap bonded joints: Effects of adhesive type and joint dimensions," *Int. J. Adhes. Adhes.*, vol. 134, Sep. 2024, Art. no. 103791, doi: 10.1016/j.ijadhadh.2024.103791.
7. P. P. Camanho and C. G. Dávila, "Mixed-mode decohesion finite elements for the simulation of delamination in composite materials," *NTRS (NASA Technical Reports Server)*, July 2002.
8. R. D. S. G. Campilho and T. A. B. Fernandes, "Comparative evaluation of single-lap joints bonded with different adhesives by cohesive zone modelling," *Procedia Engineering*, vol. 114, pp. 102-109, 2015. DOI: 10.1016/j.proeng.2015.08.055.
9. M. Abbasi, R. Ciardiello, and L. Goglio, "A novel approach for damage assessment in adhesively bonded composite joints using backface strain technique," *Compos. Part B: Eng.*, vol. 286, Nov. 2024, Art. no. 111766, doi: 10.1016/j.compositesb.2024.111766.

10. Dassault Systèmes. (2009). Using ABAQUS Online Documentation (v6.6). Retrieved from
<https://classes.engineering.wustl.edu/2009/spring/mase5513/abaqus/docs/v6.6/index.html>.
11. M. Abbasi, R. Ciardiello, and L. Goglio, "Experimental study on the effect of bonding area dimensions on the mechanical behavior of composite single-lap joint with epoxy and polyurethane adhesives," *Appl. Sci.*, vol. 13, no. 13, p. 7683, Jun. 2023, doi: 10.3390/app13137683.
12. M. Ramamurthi and Y.-S. Kim, "Delamination characterization of bonded interface using surface based cohesive model," May 2012, doi: 10.1002/9781118356074.ch38.
13. Dassault Systèmes. (2024). Abaqus/Standard element index. Retrieved from
<https://docs.software.vt.edu/abaqusv2024/English/SIMACAEELMRefMap/simaelm-c-stdelementindex.htm>
14. Altair Engineering. (2021). Elements: Definition and types. Retrieved from
https://2021.help.altair.com/2021/hwdesktop/engsol/topics/pre_processing/entities/elements_r.htm
15. J. Weiland, M. Z. Sadeghi, J. V. Thomalla, A. Schiebahn, K. U. Schroeder, and U. Reisgen, "Analysis of back-face strain measurement for adhesively bonded single lap joints using strain gauge, Digital Image Correlation and finite element method," *International Journal of Adhesion and Adhesives*, vol. 97, Mar. 2020, Art. no. 102491, doi: 10.1016/j.ijadhadh.2019.102491.
16. M. Z. Sadeghi, J. Weiland, A. Preisler, J. Zimmermann, A. Schiebahn, U. Reisgen, and K. U. Schroeder, "Damage detection in adhesively bonded single lap joints by using backface strain: Proposing a new position for backface strain gauges," *International*

- Journal of Adhesion and Adhesives, vol. 97, Mar. 2020, Art. no. 102494, doi: 10.1016/j.ijadhadh.2019.102494.
17. D. A. Bigwood and A. D. Crocombe, "Non-linear adhesive bonded joint design analyses," *International Journal of Adhesion and Adhesives*, vol. 10, no. 1, pp. 31–41, Jan. 1990, doi: 10.1016/0143-7496(90)90025-S.
 18. X. He, "A review of finite element analysis of adhesively bonded joints," *International Journal of Adhesion and Adhesives*, vol. 31, no. 4, pp. 248–264, Jun. 2011, doi: 10.1016/j.ijadhadh.2011.01.006.
 19. Hartlen, S. D., Montesano, J. S., Cronin, D. S. (2020). Cohesive zone modeling of adhesively bonded interfaces: The effect of adherend geometry, element selection, and loading condition. *International Journal of Adhesion and Adhesives*, 99.
 20. M. Z. Sadeghi, A. Gabener, J. Zimmermann, K. Saravana, J. Weiland, U. Reisgen, and K. U. Schroeder, "Failure load prediction of adhesively bonded single lap joints by using various FEM techniques," *International Journal of Adhesion and Adhesives*, vol. 97, p. 102493, Mar. 2020, doi: 10.1016/j.ijadhadh.2019.102493.
 21. M. Z. Sadeghi, J. Weiland, J. Zimmermann, A. Schiebahn, U. Reisgen, and K. U. Schroeder, "Experimental and FE investigations on the influential parameters in positioning and measurement of strain gauges in adhesively bonded single lap joints," *Procedia Structural Integrity*, vol. 28, pp. 1590–1600, 2020, doi: 10.1016/j.prostr.2020.10.131.
 22. F. L. Matthews and T. T. Tester, "The influence of stacking sequence on the strength of bonded CFRP single lap joints," *Int. J. Adhes. Adhes.*, vol. 5, no. 1, pp. 13-18, Jan. 1985. DOI: 10.1016/0143-7496(85)90040-5.
 23. B. R. K. Blackman, H. Hadavinia, A. J. Kinloch, and J. G. Williams, "The use of a cohesive zone model to study the fracture of fibre composites and adhesively-bonded

- joints," *International Journal of Fracture*, vol. 119, no. 1, pp. 25–46, Feb. 2003, doi: 10.1023/A:1023998013255.
24. S. Huzni, M. Ilfan, T. Sulaiman, S. Fonna, M. Ridha, and A. K. Arifin, "Finite element modeling of delamination process on composite laminate using cohesive elements," *Int. J. Automot. Mech. Eng.*, vol. 7, pp. 1023-1030, Jan.-Jun. 2013. DOI: 10.15282/ijame.7.2012.18.0083.
25. A. Turon, P. P. Camanho, J. Costa, and C. G. Dávila, "A damage model for the simulation of delamination in advanced composites under variable-mode loading," *Mechanics of Materials*, vol. 38, no. 11, pp. 1072–1089, Nov. 2006, doi: 10.1016/j.mechmat.2005.10.003.
26. G. T. Camacho and M. Ortiz, "Computational modelling of impact damage in brittle materials," *International Journal of Solids and Structures*, vol. 33, issues 20–22, pp. 2899–2938, Aug. 1996, doi: 10.1016/0020-7683(95)00255-3.
27. K. E. Johanns, J. H. Lee, Y. F. Gao, and G. M. Pharr, "An evaluation of the advantages and limitations in simulating indentation cracking with cohesive zone finite elements," *Modelling and Simulation in Materials Science and Engineering*, vol. 22, no. 1, p. 015011, Dec. 2013, doi: 10.1088/0965-0393/22/1/015011.
28. V. Tvergaard and J. W. Hutchinson, "The influence of plasticity on mixed mode interface toughness," *Journal of the Mechanics and Physics of Solids*, vol. 41, no. 6, pp. 1119-1135, Jun. 1993, doi: 10.1016/0022-5096(93)90057-M.
29. M. Alfano, F. M. Furguele, A. Leonardi, and G. H. Paulino, "Cohesive Zone Modeling of Mode I Fracture in Adhesive Bonded Joints," *Key Eng. Mater.*, vol. 348–349, pp. 13–18, Sep. 2007, doi: 10.4028/www.scientific.net/KEM.348-349.13.

30. R. D. Adams and N. A. Peppiatt, "Stress analysis of adhesive-bonded lap joints," *The Journal of Strain Analysis for Engineering Design*, vol. 9, no. 3, pp. 185-196, Jul. 1974, doi: 10.1243/03093247V093185.
31. J. P. M. Lopes, R. G. S. G. Campilho, R. J. B. Rocha, and F. J. G. Silva, "Geometrical parameter study of adhesively-bonded T-joints by cohesive models," *Procedia Structural Integrity*, vol. 37, pp. 714-721, 2022. DOI: 10.1016/j.prostr.2022.02.085.
32. A. Matzenmiller, S. Gerlach, and M. Fiolka, "A critical analysis of interface constitutive models for the simulation of delamination in composites and failure of adhesive bonds," *Journal of Mechanics of Materials and Structures*, vol. 5, no. 2, pp. 185-211, Aug. 2010, doi: 10.2140/jomms.2010.5.185.
33. A. Turon, J. Costa, P. P. Camanho, and J. J. C. Remmers, "Analytical and numerical investigation of the length of the cohesive zone in delaminated composite materials," in *Mechanical Response of Composites*, Jun. 2008, doi: 10.1007/978-1-4020-8584-0_4.
34. ITW Performance Polymers, *Adhesive Solutions for Electric Vehicle Batteries*, ITW Performance Polymers, 2024.
35. M. Arena and M. Viscardi, "Strain state detection in composite structures: Review and new challenges," *J. Compos. Sci.*, vol. 4, no. 2, p. 60, May 2020. DOI: 10.3390/jcs4020060.
36. X. Lu, M. Ridha, B. Y. Chen, V. B. C. Tan, and T. E. Tay, "On cohesive element parameters and delamination modelling," *Eng. Fract. Mech.*, vol. 206, pp. 278-296, 2019. DOI: 10.1016/j.engfracmech.2018.12.019.
37. M. Heidari-Rarani and M. Sayedain, "Finite element modeling strategies for 2D and 3D delamination propagation in composite DCB specimens using VCCT, CZM and

- XFEM approaches," *Theor. Appl. Fract. Mech.*, vol. 103, p. 102246, 2019. DOI: 10.1016/j.tafmec.2019.102246.
38. M. L. Benzeggagh and M. Kenane, "Measurement of mixed-mode delamination fracture toughness of unidirectional glass/epoxy composites with mixed-mode bending apparatus," *Composites Science and Technology*, vol. 56, no. 4, pp. 439-449, 1996, doi: 10.1016/0266-3538(96)00005-X.
39. M. A. S. Santos and R. D. S. G. Campilho, "Mixed-mode fracture analysis of composite bonded joints considering adhesives of different ductility," *Int. J. Fract.*, vol. 207, pp. 55–71, 2017. DOI: 10.1007/s10704-017-0219-x.
40. S. Sugiman, A. D. Crocombe, and I. A. Ashcroft, "Modelling the static response of unaged adhesively bonded structures," *Eng. Fract. Mech.*, vol. 98, pp. 296-314, 2013. DOI: 10.1016/j.engfracmech.2012.10.014.
41. P. Manikandan and G. B. Chai, "Mode-I metal-composite interface fracture testing for fibre metal laminates," *Adv. Mater. Sci. Eng.*, vol. 2018, p. 4572989, 2018. DOI: 10.1155/2018/4572989.
42. S. Xia and J. W. Hutchinson, "Cohesive zone models: A critical review of traction-separation relationships across fracture surfaces," *Appl. Mech. Rev.*, vol. 64, no. 6, p. 060802, 2012. DOI: 10.1115/1.4023112.
43. 3M, Development of Cohesive Zone Models for 3M™ Structural Adhesives. [Online]. Available: <https://multimedia.3m.com/mws/media/1854893O/3m-structuraladhesives-white-paper-en.pdf>
44. M. G. P. P. Pratama, K. Abdurohman, R. A. Pratomo, and N. M. Ula, "Shear strength comparison of single lap and joggle lap adhesive joints in carbon fiber composites manufactured via vacuum-assisted resin infusion," *Jurnal POLIMESIN*, vol. 22, no. 5, p. 526, Oct. 2024. DOI: 10.30811/jpl.v22i5.5437.

45. M. Ridha, V. B. C. Tan, and T. E. Tay, "Traction–separation laws for progressive failure of bonded scarf repair of composite panel," *Compos. Struct.*, vol. 93, no. 4, pp. 1239-1245, Mar. 2011. DOI: 10.1016/j.compstruct.2010.10.015.
46. A. Turon, C. G. Dávila, P. P. Camanho, and J. Costa, "An engineering solution for mesh size effects in the simulation of delamination using cohesive zone models," *Eng. Fract. Mech.*, vol. 74, no. 10, pp. 1665-1682, Jul. 2007. DOI: 10.1016/j.engfracmech.2006.08.025.
47. P. P. Camanho, C. G. Dávila, and M. F. S. de Moura, "Numerical simulation of mixed-mode progressive delamination in composite materials," *J. Compos. Mater.*, vol. 37, no. 16, Aug. 2003. DOI: 10.1177/0021998303034505.
48. H. C. Chetan, S. Kattimani, and S. M. Murigendrappa, "Prediction of cohesive zone length and accurate numerical simulation of delamination under mixed-mode loading," *Appl. Compos. Mater.*, 2021. DOI: 10.1007/s10443-021-09939-2.
49. A. A. Akay, S. Göktepe, and E. Gürses, "Formulation of a bilinear traction-separation interface law in boundary elements with homogenization," *Procedia Struct. Integr.*, vol. 61, pp. 138-147, 2024. DOI: 10.1016/j.prostr.2024.06.019.
50. S. H. Song, G. H. Paulino, and W. Buttlar, "A bilinear cohesive zone model tailored for fracture of asphalt concrete considering viscoelastic bulk material," *Eng. Fract. Mech.*, vol. 73, no. 18, pp. 2829-2848, Dec. 2006. DOI: 10.1016/j.engfracmech.2006.04.030.
51. S. Marzi, O. Hesebeck, M. Brede, and F. Kleiner, "A rate-dependent cohesive zone model for adhesively bonded joints loaded in Mode I," *J. Adhes.*, vol. 23, no. 6, pp. 881-898, Jan. 2009. DOI: 10.1163/156856109X411238.
52. J. da Silva, R. D. S. G. Campilho, and F. L. M. dos Santos, "Fracture analysis of highly flexible adhesives: Cohesive zone modelling and mechanical characterization,"

- Int. J. Adhes. Adhes., vol. 30, no. 1, pp. 1-14, 2010. DOI:
10.1016/j.ijadhadh.2009.06.011.
53. K. Anyfantis and N. G. Tsouvalis, "A 3D ductile constitutive mixed-mode model of cohesive elements for the finite element analysis of adhesive joints," *J. Adhes.*, vol. 27, no. 10, May 2013. DOI: 10.1080/01694243.2012.735900.
54. J. C. Brewer and P. A. Lagace, "Quadratic stress criterion for initiation of delamination," *J. Compos. Mater.*, vol. 22, no. 12, Dec. 1988. DOI: 10.1177/002199838802201205.
55. Adediran, I., Fritz, J., & Truster, T. (2025). Comparative analysis of different adhesive model representations in single lap joints using finite element analysis. *Applied Sciences*, 15(5), 2661. DOI: 10.3390/app15052661.
56. Ramalho, L. D. C., Campilho, R. D. S. G., Belinha, J., & da Silva, L. F. M. (2019). Static strength prediction of adhesive joints: A review. *International Journal of Adhesion and Adhesives*. DOI: 10.1016/j.ijadhadh.2019.102451.
57. Song, K., Dávila, C. G., & Rose, C. (2008). Guidelines and parameter selection for the simulation of progressive delamination. ResearchGate.
58. Zhang, Z. J., & Paulino, G. H. (2005). Cohesive zone modeling of dynamic failure in homogeneous and functionally graded materials. *International Journal of Plasticity*, 21(6), 1195-1254. <https://doi.org/10.1016/j.ijplas.2004.06.009>
59. Yang, C., & Cox, M. (2010). Relating Cohesive Zone Models to Linear Elastic Fracture Mechanics. NASA Technical Reports.
<https://ntrs.nasa.gov/api/citations/20100021117/downloads/20100021117.pdf>
60. T. Bhattacharjee, M. Barlingay, H. Tasneem, E. Roan, and K. Vemaganti, "Cohesive zone modeling of mode I tearing in thin soft materials," *J. Mech. Behav. Biomed. Mater.*, vol. 28, pp. 37–46, Dec. 2013, doi: 10.1016/j.jmbbm.2013.07.015.

61. A. F. L. Macedo, R. D. S. G. Campilho, F. J. G. Silva, and M. A. Bellali, "Numerical analysis of the mixed-mode fracture of bonded joints depending on the adhesive thickness," *Proc. IMechE Part E: J. Process Mechanical Engineering*, vol. 237, no. 1, pp. 4–25, 2023, doi: 10.1177/09544089221088262.
62. G. Stamoulis, N. Carrere, J. Y. Cognard, P. Davies, and C. Badulescu, "On the experimental mixed-mode failure of adhesively bonded metallic joints," *Int. J. Adhes. Adhes.*, vol. 51, pp. 148–158, June 2014, doi: 10.1016/j.ijadhadh.2014.03.002.
63. D. F. O. Silva, R. D. S. G. Campilho, F. J. G. Silva, and U. T. F. Carvalho, "Application a direct/cohesive zone method for the evaluation of scarf adhesive joints," *Applied Adhesion Science*, vol. 6, article no. 13, Dec. 2018. DOI: 10.1186/s40563-018-0123-x.
64. G. Mirone, R. Barbagallo, G. Bua, and G. La Rosa, "Finite Element Simulation and Sensitivity Analysis of the Cohesive Parameters for Delamination Modeling in Power Electronics Packages," *Materials*, vol. 16, p. 4808, 2023. DOI: 10.3390/ma16134808.
65. I. Ikramullah, A. Afrizal, S. H. Huzni, S. Thalib, H. P. S. A. Khalil, and S. Rizal, "Effect of Mesh Sensitivity and Cohesive Properties on Simulation of Typha Fiber/Epoxy Microbond Test," *Computation*, vol. 8, no. 1, p. 4, Jan. 2020. DOI: 10.3390/computation8010004.
66. C. Zhang, H. Liu, J. Cao, and C. Zhang, "Rate-Dependent Cohesive Models for Dynamic Mode I Interfacial Propagation and Failure of Unidirectional Composite Laminates," *Coatings*, vol. 11, p. 191, Feb. 2021. DOI: 10.3390/coatings11020191.
67. E. Amsterdam, J. W. E. Wiegman, M. Nawijn, and J. Th. M. De Hosson, "On the strain energy release rate and fatigue crack growth rate in metallic alloys," *Engineering Fracture Mechanics*, vol. 286, Article 109292, Apr. 2023. DOI: 10.1016/j.engfracmech.2023.109292.

68. H. B. Yin, L. H. Liang, Y. G. Wei, Z. L. Peng, and S. H. Chen, "Determination of the interface properties in an elastic film/substrate system," *International Journal of Solids and Structures*, vol. 191–192, pp. 473–485, Jan. 2020. DOI: 10.1016/j.ijsolstr.2020.01.003.
69. S. Oshima and J. Koyanagi, "Review on Damage and Failure in Adhesively Bonded Composite Joints: A Microscopic Aspect," *Polymers*, vol. 17, p. 377, Jan. 2025. DOI: 10.3390/polym17030377.
70. H. Malekinejad, R. J. C. Carbas, A. Akhavan-Safar, E. A. S. Marques, F. C. Sousa, and L. F. M. da Silva, "Enhancing Fatigue Life and Strength of Adhesively Bonded Composite Joints: A Comprehensive Review," *Materials*, vol. 16, p. 6468, Sep. 2023. DOI: 10.3390/ma16196468.
71. M. J. Lee, T. M. Cho, W. S. Kim, B. C. Lee, and J. J. Lee, "Determination of cohesive parameters for a mixed-mode cohesive zone model," *International Journal of Adhesion & Adhesives*, vol. 30, pp. 322–328, Mar. 2010. DOI: 10.1016/j.ijadhadh.2009.10.005.
72. J. J. G. Oliveira, R. D. S. G. Campilho, F. J. G. Silva, E. A. S. Marques, J. J. M. Machado, and L. F. M. da Silva, "Adhesive thickness effects on the mixed-mode fracture toughness of bonded joints," *J. Adhes.*, vol. 96, no. 1–4, pp. 300–320, 2020, doi: 10.1080/00218464.2019.1681269.
73. L. F. R. Neves, R. D. S. G. Campilho, I. J. Sánchez-Arce, K. Madani, and C. Prakash, "Numerical Modelling and Validation of Mixed-Mode Fracture Tests to Adhesive Joints Using J-Integral Concepts," *Processes*, vol. 10, p. 2730, Dec. 2022. DOI: 10.3390/pr10122730.
74. S. Rezaei, J. R. Mianroodi, K. Khaledi, and S. Reese, "A nonlocal method for modeling interfaces: Numerical simulation of decohesion and sliding at grain

- boundaries," *Computer Methods in Applied Mechanics and Engineering*, vol. 362, p. 112836, Apr. 2020. DOI: 10.1016/j.cma.2020.112836.
75. J. R. Reeder, "3D mixed-mode delamination fracture criteria - An experimentalist's perspective," *ResearchGate*, Jan. 2006. [Online]. Available: <https://www.researchgate.net/publication/>. [Accessed: Mar. 2025].
76. J. J. Rimoli and J. J. Rojas, "Meshing strategies for the alleviation of mesh-induced effects in cohesive element models," *International Journal of Fracture*, vol. 193, pp. 29–42, Mar. 2015.
77. C. Xu, T. Siegmund, and K. Ramani, "Rate-dependent crack growth in adhesives: I. Modeling approach," *International Journal of Adhesion and Adhesives*, vol. 23, no. 1, pp. 9–13, 2003, doi: 10.1016/S0143-7496(02)00062-3.
78. J. Chopin, R. Villey, D. Yarussso, M. Ciccotti, and others, "Nonlinear Viscoelastic Modeling of Adhesive Failure for Polyacrylate Pressure-Sensitive Adhesives," *Macromolecules*, vol. 51, no. 21, Oct. 2018. DOI: 10.1021/acs.macromol.8b01374.
79. P. Cornetti, M. Muñoz-Reja, A. Sapora, and A. Carpinteri, "Finite fracture mechanics and cohesive crack model: Weight functions vs. cohesive laws," *International Journal of Solids and Structures*, vol. 156–157, pp. 126–136, Aug. 2018. DOI: 10.1016/j.ijsolstr.2018.08.003.
80. M. K. Budzik, M. Wolfahrt, P. Reis, M. Kozłowski, J. Sena-Cruz, L. Papadakis, M. N. Saleh, K. V. Machalicka, S. Teixeira de Freitas, and A. P. Vassilopoulos, "Testing mechanical performance of adhesively bonded composite joints in engineering applications: an overview," *Journal of Adhesion*, vol. 98, no. 14, pp. 2133–2209, 2021. DOI: 10.1080/00218464.2021.1953479.

81. H. L. Groth, "Viscoelastic and viscoplastic stress analysis of adhesive joints," *International Journal of Adhesion and Adhesives*, vol. 10, no. 3, pp. 207–207, Jul. 1990.
82. P. Jousset and M. Rachik, "Comparison and evaluation of two types of cohesive zone models for the finite element analysis of fracture propagation in industrial bonded structures," *Engineering Fracture Mechanics*, vol. 132, pp. 48–69, Oct. 2014. DOI: 10.1016/j.engfracmech.2014.10.018.
83. J. D. Ferry, *Viscoelastic Properties of Polymers*, 3rd ed. New York: Wiley, 1980.
84. W. F. Hosford, *Mechanical Behavior of Materials*, 2nd ed. Cambridge: Cambridge University Press, 2009.
85. S. Omairey, N. Jayasree, and M. Kazilas, "Defects and uncertainties of adhesively bonded composite joints," *SN Applied Sciences*, 2021. DOI: 10.1007/s42452-021-04753-8.